# OpenGRID

## EXPLORING BEYOND BOUNDARIES

Compilation of
Open Access Publishing at BARC, Trombay


भाभा परमाणु अनुसंधान केंद्र
BHABHA ATOMIC RESEARCH CENTRE

IOP Publishing

**2023 - 2024**

# CONTENTS

## IOP Publishing
## Year 2024

मनोज सिंह
MANOJ SINGH

सत्यमेव जयते
भारत सरकार
Government of India

अध्यक्ष, वैज्ञानिक सूचना संसाधन प्रभाग
भाभा परमाणु अनुसंधान केंद्र
**Head,** Scientific Information Resource Division
Bhabha Atomic Research Centre

## PREFACE

Open Access publishing marks a pioneering step in SIRD's efforts to transition scholarly outputs to a more inclusive, author-centred Open Access (OA) publishing. These transformative agreements, by design, enable researchers to publish their articles Open Access in hundreds of prestigious journals while retaining reading rights to those same journals. This model reflects the global trend among libraries, consortia, and research institutions aiming to democratise the dissemination of knowledge without compromising quality or reach.

**IOP Publishing (IOP)** has a transformative agreement with several institutions in India to enable a transition to open access publishing. In 2023, SIRD, BARC signed an agreement with the Institute of Physics (IOP), Bristol, UK, to cover the funding for authors towards Article Processing Charges (APC) for OA publishing for their articles in the listed IOP journals.

This agreement between BARC and IOP allows researchers to publish their articles in 78 Gold and Hybrid journals from January 2023 to December 2024.

This compilation, named "OpenGRID - Exploring Beyond Boundaries", is the second series of publications under the OpenGRID banner. This series captures BARC researchers' published articles from January 2023 to December 2024, which is a noteworthy breakthrough in the transformative journey of **Open Access (OA) publishing at Bhabha Atomic Research Centre (BARC)**, Trombay, Mumbai.

Moving forward, we must recognise that Open Access is not an end but a means to a larger goal of an inclusive, transparent, and collaborative scientific temperament that serves the public interest.

I congratulate all my SIRD colleagues, involved in this pioneering effort of OA initiative and confident that such a compilation will motivate other researchers for more Open Access publishing, resulting more global access to their research and achieving further citations.

(Manoj Singh)

भाभा परमाणु अनुसंधान केंद्र, ए-01, सेंट्रल कॉम्प्लेक्स, ट्रॉम्बे, मुंबई - 400 085, भारत
Bhabha Atomic Research Centre, A-01, Central Complex, Trombay, Mumbai 400 085, India
दूरभाष / Tel. : (91-22) 2559 0820 / 3685 / 2073 • फैक्स / Fax : (91-22) 2551 9613 / 2550 5151
आवास / Res.: +91-22-96195 16929 • ई-मेल / E-mail : smanoj@barc.gov.in, headsird@barc.gov.in

| | | |
|---|---|---|
| 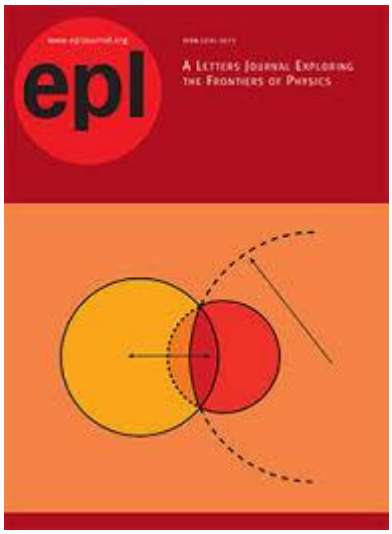 |  |  |
| Europhysics Letters | Journal of Electrochemical society | Journal of instrumentation |
| 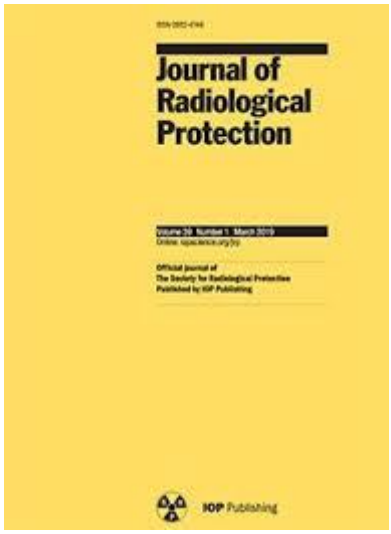 | IOP Publishing<br>Year 2023 | 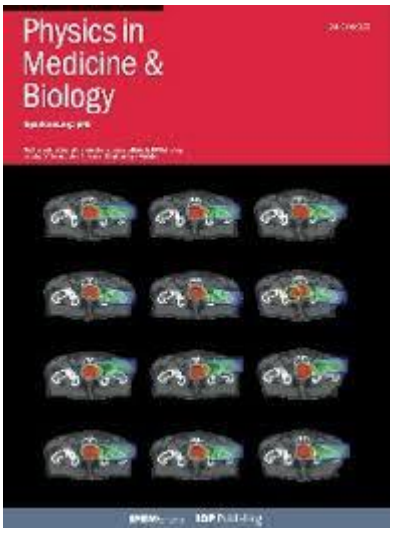 |
| Journal of Radiological Protection | | Physics in Medicine & Biology |
| 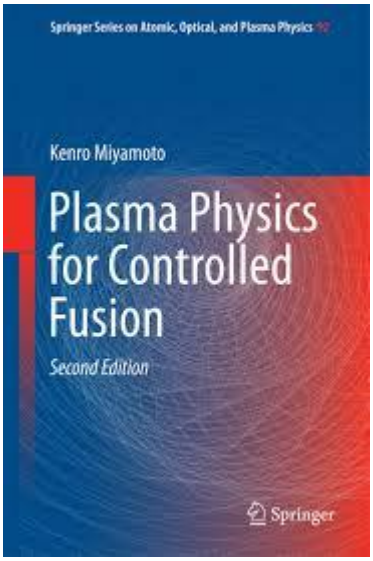 | 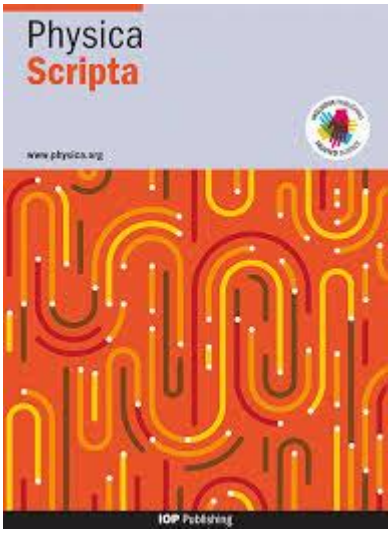 |  |
| Plasma Physics and Controlled Fusion | Physica Scripta | Materials Research Express |

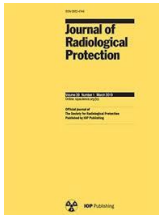

1

IOP Publishing J. Radiol. Prot. 43 (2023) 041508 https://doi.org/10.1088/1361-6498/ad04ef

Journal of Radiological Protection

PAPER

# $^{131}$I dose coefficients for a reference population using age-specific models

**Pradeep Kumar Singh*, Hemant Kumar Patni, Rahul Roy, Deepak Kumar Akar and Pramilla D Sawant**

Internal Dosimetry Section, Radiation Safety Systems Division, Bhabha Atomic Research Centre, Trombay, Mumbai 400085, India

* Author to whom any correspondence should be addressed.

**E-mail:** pradeepsingh@barc.gov.in

**Keywords:** paediatric reference computational phantoms, $^{131}$I age-specific dose coefficients, FLUKA

Supplementary material for this article is available online

OPEN ACCESS

RECEIVED
2 June 2023

REVISED
22 September 2023

ACCEPTED FOR PUBLICATION
19 October 2023

PUBLISHED
2 November 2023



## Abstract

Age-specific dose coefficients are required to assess internal exposure to the general public. This study utilizes reference age-specific biokinetic models of iodine to estimate the total number of nuclear disintegrations $\tilde{a}(r_S,\tau)$ occurring in source regions ($r_S$) during the commitment time ($\tau$). Age-specific S values are estimated for 35 target regions due to $^{131}$I present in 22 $r_S$ using data from 10 paediatric reference computational phantoms (representing five ages for both sexes) published recently by the International Commission of Radiation Protection (ICRP). Monte Carlo transport simulations are performed in FLUKA code. The estimated $\tilde{a}(r_S,\tau)$ and S values are then used to compute the committed tissue equivalent dose $H_T(\tau)$ for 27 radiosensitive tissues and dose coefficients $e(\tau)$ for all five ages due to inhalation and ingestion of $^{131}$I. The derived $\tilde{a}(r_S,\tau)$ values in the thyroid source are observed to increase with age due to the increased retention of iodine in the thyroid. S values are found to decrease with age, mainly due to an increase in target masses. Generally, $H_T(\tau)$ values are observed to decrease with age, indicating the predominant behaviour of S values over $\tilde{a}(r_S,\tau)$. On average, ingestion dose coefficients are 63% higher than for inhalation in all ages. The maximum contribution to dose coefficients is from the thyroid, accounting for 96% in the case of newborns and 98%–99% for all other ages. Furthermore, the estimated $e(\tau)$ values for the reference population are observed to be lower than previously published reference values from the ICRP. The estimated S, $H_T(\tau)$ and $e(\tau)$ values can be used to improve estimations of internal doses to organs/whole body for members of the public in cases of $^{131}$I exposure. The estimated dose coefficients can also be interpolated for other ages to accurately evaluate the doses received by the general public during $^{131}$I therapy or during a radiological emergency.

## 1. Introduction

$^{131}$I, due to its small half-life (8.02 days) and high-energy beta-emission (maximum energy of 606 keV with a yield of 89%), is used in the treatment for hyperthyroidism caused by Graves' disease [1]. Additionally, due to the presence of high-energy gamma radiation (energy of 364 keV with a yield of 82%), it is also used for thyroid/whole-body scintigraphy and other diagnostic purposes [2]. Further, $^{131}$I exposure to the public may occur via direct inhalation during radiological emergencies and/or via ingestion of fallout radiation through food, milk, etc. Assessment of internal dose is important during diagnostic and therapeutic use of radioiodine. Moreover, such assessments are also essential for public safety and regulatory compliance during radiological/nuclear emergencies [3]. These factors make $^{131}$I the most extensively studied and prominent internal contaminant in radiation protection.

Estimation of absorbed dose in a target region ($r_T$) due to emission from a source region ($r_S$) mainly requires two quantities: (1) $\tilde{a}(r_S,\tau)$, which represents the time-integrated activity (or nuclear disintegration) in $r_S$ over a commitment time $\tau$ and (2) $S(r_T \leftarrow r_S)$, the mean absorbed energy in $r_T$ per unit disintegration in

IOP Publishing J. Radiol. Prot. 43 (2023) 041508 P K Singh et al

$r_S$, also known as the S value [4]. The estimation of $\tilde{a}(r_S,\tau)$ involves solving biokinetic models of radionuclides. Furthermore, S values are computed based on the specific absorbed fractions (SAFs) derived from Monte Carlo simulations of absorbed fractions (AFs) in $r_T$ of computational phantoms due to emission from $r_S$. S values can also be computed by directly simulating the energy deposition in $r_T$ due to complete decay of radionuclides in $r_S$ [5].

At present, the $\tilde{a}(r_S,\tau)$ values of $^{131}$I for the reference population [6] are based on the age-specific human respiratory tract model (HRTM) [7], the gastrointestinal tract (GI-tract) model [8] and the three-compartment systemic model of iodine [9]. The reference SAF values are derived from age-specific Oak Ridge National Laboratory stylized mathematical phantoms [10–12]. Based on these $\tilde{a}(r_S,\tau)$ and SAF values, reference $^{131}$I committed tissue equivalent doses, $H_T(\tau)$, and dose coefficients, $e(\tau)$, have been provided in various International Commission of Radiation Protection (ICRP) publications [13, 14].

Recently, a more comprehensive systemic model of iodine was published [15] that provides detailed retention and excretion rates for the redefined reference population [16]. The age-specific human alimentary tract model (HATM) has also been updated for the reference population [17]. In the revised HATM, all alimentary tract organs from the oral cavity to the rectosigmoid are included, with provisions for blood absorption from all these organs.

Furthermore, mathematical stylized phantoms have been updated using 10 paediatric reference computational (PRC) phantoms [18], representing the reference population as per ICRP publication 89 [16]. PRC phantoms have been developed by modifying the University of Florida and National Cancer Institute (UF/NCI) hybrid phantoms [19], and provide a more realistic representation of the human anatomy compared to stylized phantoms. Earlier studies have shown variations in effective doses due to photons, electron [20] and $^{18}$F-FDG [21] estimated using a voxel-based model from those estimated using stylized phantoms. The UF/NCI and PRC phantoms have been used to compute SAF values for electrons and photons of various energies [22–24], which in turn are used to compute S values and organ doses for medical intake scenarios [24, 25]. These studies only focus on dose computation for medical protection pathways such as intravenous and oral administration, while leaving out the inhalation pathway required for radiological protection.

In this study, we estimated age-specific $\tilde{a}(r_S,\tau)$ for the reference population in the case of $^{131}$I inhalation and ingestion using the latest available biokinetic models. S values for 35 target regions are estimated due to $^{131}$I distributed in 22 source regions for PRC phantoms by simulating the complete decay of $^{131}$I in the FLUKA Monte Carlo simulation code. Using these $\tilde{a}(r_S,\tau)$ and S values, age-specific $H_T(\tau)$ and $e(\tau)$ are computed for the reference population.

## 2. Materials and method

This section describes methods for determining the $\tilde{a}(r_S,\tau)$ of $^{131}$I in various $r_S$ of the reference population, as well as the incorporation of PRC phantoms in the Monte Carlo simulation code FLUKA. Additionally, methods for energy scoring and estimating S values, computations of age-specific $H_T(\tau)$ and $e(\tau)$ values are also discussed.

### 2.1. Estimation of age-specific $\tilde{a}(r_S,\tau)$

The biokinetic compartmental model of any radionuclide is described by a system of first-order differential equations, which can be solved by transforming them into a matrix equation, as given in equation (1) [26]:

$$A(t) = \exp(R \times t) \times A(0), \tag{1}$$

where elements of column matrix $A(t)$ represent activity in different compartments at time $t$, while $R$ is a square matrix with diagonal elements given by $r_{ii} = -\sum_j \lambda_{ij} - \lambda_R$ and non-diagonal elements as $r_{ij} = \lambda_{ji}$. $\lambda_{ij}$ is the transfer rate from $i$th to $j$th compartment, $\lambda_R$ is the radioactive decay rate and $A(0)$ represents the initial activity deposited in compartments. Equation (1) is integrated over a commitment time $\tau$ to obtain column matrix $\tilde{A}(\tau)$, whose elements represent time-integrated activity in various compartments (equation (2)):

$$\tilde{A}(\tau) = R^{-1}(\exp(R * \tau) - I) \times A(0). \tag{2}$$

The commitment times are taken as (70–$t$) years for the reference population, with $t$ being the age of the individual at intake. The complete inhalation model of iodine is shown in figure 1. This model is prepared for each individual age group (assuming same for males and females) by combining the HRTM [7], the HATM [17] and the iodine systemic model [15]. For each age, an inhalation intake of 1 Bq of $^{131}$I aerosol with an activity median aerodynamic diameter of 1 $\mu$m is assumed, with fast blood absorption. In the case of ingestion, respiratory tract compartments are excluded and unit activity is assumed to be directly deposited

2

Jinst

Published by IOP Publishing for Sissa Medialab

Received: *April 25, 2023*
Accepted: *May 3, 2023*
Published: *June 20, 2023*

# 11–20 MeV Alvarez Drift Tube Linac for low energy proton accelerator

**Vikas Teotia,* Sanjay Malhotra, Prashant Kumar, Elina Mishra, Sumit Meshram and Rajesh Chimurkar**

*Electromagnetic Applications & Instrumentation Division, Bhabha Atomic Research Centre, Trombay, India*

*E-mail:* vteotia@gmail.com

Abstract: Bhabha Atomic Research Centre is developing Low Energy High Intensity Proton Accelerator (LEHIPA) as a pre-injector for proposed Accelerator Driven Sub-Critical Reactor Systems (ADSS). Drift Tube Linac is one of the two major accelerating structures of LEHIPA, the other being the Radio Frequency Quadrupole (RFQ). Like all particle accelerating structures, DTL needs multi-disciplinary expertise for design, production, qualification, and installation. This paper describes the comprehensive design, production, qualification, and installation of the ~ 11–20 MeV section of DTL. It details the design of all sub-components which form part of the DTL RF cavity. Several novel concepts were implemented in course of this development. Important among them are DT-DTL alignment, referencing methodology, robust vacuum design and hermetically sealed DTs. This paper is a comprehensive coverage of design, development and installation aspects of Alvarez DTL. At present, the DTL is ready for beam commissioning.

Keywords: Accelerator Subsystems and Technologies; Accelerator Applications; DTL; LEHIPA

*Corresponding author.



https://doi.org/10.1088/1748-0221/18/06/P06020

2023 JINST 18 P06020

## Contents



2023 JINST 18 P06020

## 1 Introduction

Low Energy High-Intensity Proton Accelerator (LEHIPA) is a 20 MeV, 30 mA proton Accelerator [1] being built by Bhabha Atomic Research Centre, Trombay, India as a pre-injector to the proposed Accelerator Driven Sub-Critical Reactor System [2, 3]. Drift Tube Linac is one of the two major accelerating structures of LEHIPA, the other being the Radio Frequency Quadrupole (RFQ) [4]. Figure 1 shows the block diagram of LEHIPA [1]. DTL3 and DTL4 are aligned, vacuum leak tested and RF qualified and are being taken for RF conditioning to be followed by beam commissioning. This paper describes, the design, engineering, production, testing, and installation of DTL3 and DTL4.

DTL is a cylindrical cavity operating in $TM_{010}$ mode with Drift Tubes (DTs) arranged concentric and along the axis of the DTL with $\beta\lambda$ spacing between consecutive DTs. The widths of DTs are proportional to $\beta\lambda$. The accelerating gap between two consecutive DTs is tuned to maintain the same

3

IOP Publishing J. Radiol. Prot. 43 (2023) 031503 https://doi.org/10.1088/1361-6498/ace3d3

Journal of Radiological Protection

OPEN ACCESS

RECEIVED
10 May 2023

REVISED
27 June 2023

ACCEPTED FOR PUBLICATION
4 July 2023

PUBLISHED
13 July 2023



PAPER

# A machine learning approach for correcting glow curve anomalies in $CaSO_4$:Dy-based TLD dosimeters used in personnel monitoring

Munir S Pathan[1,2,*], S M Pradhan[1,2], T Palani Selvam[1,2] and B K Sapra[1,2]

[1] Radiological Physics & Advisory Division, Health, Safety & Environment Group, Bhabha Atomic Research Centre, Mumbai, India
[2] Homi Bhabha National Institute, Mumbai, India
* Author to whom any correspondence should be addressed.

E-mail: mspathan.work@gmail.com and mspathan@barc.gov.in

Keywords: personnel dosimeter, thermoluminescence, glow curve analysis, machine learning

## Abstract

The study presents a novel approach to analysing the thermoluminescence (TL) glow curves (GCs) of $CaSO_4$:Dy-based personnel monitoring dosimeters using machine learning (ML). This study demonstrates the qualitative and quantitative impact of different types of anomalies on the TL signal and trains ML algorithms to estimate correction factors (CFs) to account for these anomalies. The results show a good degree of agreement between the predicted and actual CFs, with a coefficient of determination greater than 0.95, a root mean square error less than 0.025, and a mean absolute error less than 0.015. The use of ML algorithms leads to a significant two-fold reduction in the coefficient of variation of TL counts from anomalous GCs. This study proposes a promising approach to address anomalies caused by dosimeter, reader, and handling-related factors. Furthermore, it accounts for non-radiation-induced TL at low dose levels towards improving the dosimetric accuracy in personnel monitoring.

## 1. Introduction

Thermoluminescent dosimeters (TLDs), optically stimulated luminescence dosimeters, and radio-photoluminescent glass are widely used for the measurement of doses from ionising radiation. The advantage of these dosimeters lies in their ability to emit a luminescence signal proportional to the dose received, making them ideal for monitoring the radiation exposure of occupational workers. Out of the aforementioned luminescence dosimeters, thermoluminescence (TL)-based dosimeters are one of the most commonly used dosimeters in personnel monitoring of radiation workers. One of the key features of any TL dosimeter is its glow curve (GC), which is used to estimate the dose. The area under the curve or peak height of the GC is interpreted as a measure of the dose. The accuracy of the estimated dose is directly dependent on the correctness of the GC. To ensure the accuracy of GC in routine personnel monitoring, the TLDs are read using TLD readers, which have highly reproducible temperature profiles and stable response. Despite this, several factors can affect the profile of the TL intensity emitted by the dosimeters, leading to anomalies in the GC.

The sources of anomalies may be related to the dosimeter, reader system, handling of the TLD during field use and readout, and so on [1–3]. At lower dose levels, deviations in the shape of the GC are commonly attributable to non-radiation-induced TL signals (NRI-TL) originating from black body radiation from the TL element, the heated components of the TLD reader and dark current from the photomultiplier tube [4]. Other factors, such as dirt, dust, oil, corrosion of the TLD card and aberrations such as scratches or stress on the TL element may also affect the shape of GC [2]. The occurrence of NRI-TL and its proportion, along with scattering data, are stochastic in nature and mostly difficult to control in routine personnel monitoring, where the majority of doses are of low level. Hence, it is important to perform an assessment of the GCs before dose computation in personnel monitoring.

A machine learning (ML)-based algorithm has been developed [3] for probabilistic GC analysis of the $CaSO_4$:Dy based TLD badge used for countrywide individual monitoring in India. When the GC of a TL

element dosimeter is determined to be anomalous with significant distortion in its shape, then its TL counts cannot be used for dose calculation. In such scenarios, the TL counts from the remaining TL elements, having normal GCs, can be used for the estimation of the dose. However, such an estimation for the TLD badge requires certain assumptions about the type and energy of radiation, compromising the accuracy of dose evaluation [5, 6]. Further, in the case of TLD reader malfunctions, such as a variation in the heating profile or an increase in the reader background signal, all of the TL elements of the TLD card may be affected and the above approach cannot be used for the estimation of dose. Therefore, it is important to estimate the proper TL count from the anomalous GC so that occupational dose can be calculated. Some distortions in the shape of the GC, such as those caused by the variations in the heating profile or NRI-TL signal, follow a predictable pattern [7]. These patterns can be utilized to determine corrected TL counts from anomalous GCs. With this objective, in the present study, we attempted to develop a method to predict TL counts from anomalous GCs as if their shape was normal.

Recently, researchers have explored the feasibility of using ML algorithms for identifying anomalous GCs, to study the characteristics of TL emission and for the estimation of elapsed time after exposure [3, 8–15]. As mentioned earlier, we demonstrated the effectiveness of ML algorithms in identifying abnormal GCs and classifying them based on the associated abnormalities [3]. In the present study, we investigate the TL intensity pattern to estimate corrected TL counts from anomalous GCs with the utilisation of ML algorithms. Therefore, regression models that are capable of estimating correction factors (CFs) based on the shape of the GCs were developed, and subsequently, their performance was evaluated. The results demonstrate impressive accuracy in the estimation of CFs and thereby in the dose estimated, and that this can be achieved from GCs that are thought to be lost due to anomalies.

## 2. Material and methods

### 2.1. $CaSO_4$:Dy-based TDL personnel monitoring system

The TLD Badge comprises a TLD card and Cassette [6, 16, 17]. The TLD card comprises three TL elements (discs) clipped to a nickel plated aluminium TL element holder. The TL-element is a pellet consisting of $CaSO_4$:Dy TL phosphor mixed with polytetrafluoroethylene in a 1:3 weight proportion. The pellet has a diameter of 13.3 mm and a thickness of 0.8 mm. The TL phosphor $CaSO_4$:Dy exhibits an energy-dependent response [6, 18]; hence, the TLD card is loaded into the cassette with filters to compensate for the energy dependence, and the ratios of TL counts from different elements are utilized for the gross estimation of the energy/type of radiation. The first disc, commonly referred to as D1, is provided with a metal filter consisting of a 1 mm thick Cu and a 0.6 mm thick Al filter. The second disc, D2, is sandwiched between polystyrene filters of thickness 1.6 mm (180 mg $cm^{-2}$). The third disc, D3, does not have any filters. The TLD card is sealed into a polythene pouch with a wrapper with information about the user of the TLD badge printed on it. The pouch and wrapper together have a density thickness of ~13–14 mg $cm^{-2}$. A schematic diagram of the TLD cassette and filters is shown in figures 1(a) and (b) respectively. Note that the polythene pouch, wrapper and clip for wearing the TLD badge are not shown in figure 1(a).

The TLD cards are read using a semi automatic TLD badge reader that employs a hot $N_2$ gas-based heating system with a clamping temperature of 285 °C for 30 s [19]. A flow rate of 5 l $min^{-1}$ and pressure of 2 kg $cm^{-2}$ are maintained during the readout to control the amount of heat delivered to the TL element. The intensity of the TL emitted during the heating cycle is recorded every second and stored as TL counts.

Several quality control checks are implemented in the TLD badge-based monitoring programme to ensure the quality of the dosimeters. These include dosimetric testing of $CaSO_4$:Dy phosphor batches, physical examination of new discs for coloration, inclusion of foreign particles, voids, and physical and dosimetric individual testing of TLD cards before introduction into service. During service before selecting for reuse, each dosimeter is physically examined for the quality of the discs as well as the nickel plating on the aluminium cards. In addition, the background of freshly annealed dosimeters is checked on a sample basis. It is verified that 3.29 times the standard deviation of annealed background counts from a random sample does not exceed 100 counts (0.1 mSv equivalent). To avoid the possibility of a higher residual signal due to excessive exposure, cards indicating counts 50 000 $\mu$Sv equivalent in the previous cycle are segregated. In spite of the above measures, during field use, reuse and processing, TLD cards undergo various forms of handling and treatments, which, when combined with the stochastic nature of the NRI-TL, may lead to variability in the shape of the GC and thereby in the dose estimates. These effects are more dominant at lower dose levels.

### 2.2. Characteristics of GC and dataset preparation

A normal GC has a peak position of between 9 and 11 s and a tail-to-peak height ratio of between 0.25 and 0.30. At low doses (less than about 0.5 mSv), the tail-to-peak ratio may exceed 0.3, but generally remains less than 0.5 [5]. When the TL-element is overheated due to higher clamping temperature or a higher flow rate of

4

Jinst

Published by IOP Publishing for Sissa Medialab

Received: *June 18, 2023*
Accepted: *July 2, 2023*
Published: *September 19, 2023*

# Capacitance-based absolute pressure gauge for beamline vacuum measurement applications

**Vikas Teotia,* Prashant Kumar, Sampada Sawant, Sumit Meshram, S.R. Patil and Sanjay Malhotra**

*Electromagnetic Applications Section, Electromagnetic Applications & Instrumentation Division, Bhabha Atomic Research Centre, Trombay, India*

*E-mail:* vteotia@gmail.com

Abstract: For low-pressure measurements, capacitance diaphragm-based absolute pressure gauges are used owing to their high accuracy, media independence, and simplistic design. Catering to the general requirements of synchrotron beamline vacuum measurements, a capacitance diaphragm-based absolute pressure gauge is designed, developed, tested, and calibrated. The sensor is having electrode assembly which forms a dual capacitor with the gauge body. The two capacitances are used in post-processing to reduce the noise levels and to enhance the precision and accuracy of the measurements. The reference side is at high vacuum of the level $5 \times 10^{-5}$ Pa. The vacuum of the reference side is generated using a Turbo Molecular Pump and is sustained by pinching-off the reference side at this vacuum. A getter pump is provided and energized for improving the vacuum which otherwise gets deteriorated due to outgassing in the reference region of the gauge. The fabrication methods adopted for fabricating the gauge are novel. The diaphragm is fabricated from bulk material using the electrical discharge method (EDM). This helped in achieving a perfect diaphragm with linear deflection with pressure variation and attained a 100% success rate. Unlike the fabrication by welding of plate, this method is robust, economical, and helped in achieving similar properties across the gauges. The second innovation is in the fabrication of electrode assembly. Unlike commonly used electrodeposited electrodes; the presented technique used copper plates which sandwich the Alumina dielectric. The plates are bolted/brazed/welded across the ceramic disc with the help of pins which also help in the parallel connection of the dual capacitors are described later. This made this method of fabrication largely rejection free with the potential of repairs and testing with different plate configurations. This paper is presenting the design, production, and calibration of the gauge using these fabrication techniques for $1 \times 10^3$ Pa to $1 \times 10^5$ Pa.

Keywords: Instrumentation for particle accelerators and storage rings - high energy (linear accelerators, synchrotrons); Instrumentation for synchrotron radiation accelerators

*Corresponding author.



https://doi.org/10.1088/1748-0221/18/09/P09031

2023 JINST 18 P09031

## Contents





## 1 Introduction

Low-pressure measurement sensors have numerous applications in industry and research laboratories, specially in beamlines. Even high vacuum systems need low vacuum level gauges for generating TMP (Turbo Molecular Pump) switch-on signals. Diaphragm-based capacitive pressure sensors are simple, robust, accurate, and media-independent and measure only the pressure exerted by residual gas particles [1].

Figure 1 shows the basic sketch of the capacitance-based diaphragm gauge. It consists of two hermetically sealed and isolated regions called the process side (one having media to be measured) and the reference side (maintained at low pressure $\sim 1 \times 10^{-5}$ Pa). A thin diaphragm isolates these two regions. The diameter and thickness of the diaphragm determine the key parameters of the gauge like range, sensitivity, and dimensions. The process side is connected to the process under measurement via KF (Klein Flansche), or CF (Con-flat) flange. The reference side consists of the capacitance electrode assembly, and getter assembly and is connected to the TMP by a pinch-off tube for evacuation to pressure of the order of $1 \times 10^{-5}$ Pa.

The electrode assembly forms two sets of capacitors with respect to the diaphragm (gauge body) as shown in figure 2.

The two capacitances change when the diaphragm, as shown in figure 2 deflects under the influence of differential pressure. This causes the average distance between the diaphragm and electrode to decrease. Reduction in distance increases the capacitance as per the following formula

$$C = \frac{\varepsilon_0 A}{d} \tag{1.1}$$

5

Published by IOP Publishing for Sissa Medialab

Received: *March 6, 2023*
Accepted: *April 16, 2023*
Published: *May 15, 2023*

# Development of FPGA-based standalone, portable TDCR system

**M.K. Sharma,**[a,b,*] **Shivam Agarwal,**[b] **M.S. Kulkarni,**[a,b] **S.V. Baraiya**[b] **and D.B. Kulkarni**[b]

[a] *Homi Bhabha National Institute, Mumbai, India*
[b] *Bhabha Atomic Research Centre, Mumbai, India*

*E-mail:* mksharma@barc.gov.in

Abstract: A standalone, lightweight, portable, FPGA-based triple to double coincidence ratio (TDCR) system is developed. The optical chamber of the system is fabricated in a dual, coaxial cylindrical geometry, with the inner cylinder made up of Teflon and the outer one of aluminium. Three square PMTs, each having an active cathode area of 2.3 cm × 2.3 cm, are housed in the optical chamber. The variation in detection efficiency to identify the optimum kB (ionization quenching parameter) value is achieved by changing the vial position vertically with respect to the centre line of the PMTs. The coincidence analyzer implemented in a field programmable gate array (FPGA) transfers the pulse counts and associated parameters in real time to a Raspberry Pi single board computer (SBC). The TDCR algorithm to compute the efficiency is implemented in the SBC. In addition, the SBC is interfaced with a local 7″ touchscreen to provide an intuitive graphical user interface (GUI) for operating the standalone instrument. The system performance is validated with $^{3}$H and $^{14}$C radionuclide standards.

Keywords: Digital electronic circuits; Modular electronics; Data acquisition circuits; Detector control systems (detector and experiment monitoring and slow-control systems, architecture, hardware, algorithms, databases)

*Corresponding author.



https://doi.org/10.1088/1748-0221/18/05/P05016

2023 JINST 18 P05016

## Contents



2023 JINST 18 P05016

## 1 Introduction

The triple to double coincidence ratio (TDCR) systems are used worldwide for the standardization of pure beta, alpha, and electron capture (EC) radionuclides [1]–[6]. A TDCR system consists of a dedicated liquid scintillation (LS) counter comprising three photomultiplier tubes (PMTs) to count the coincidences and a computing platform to determine the double and triple coincidence efficiencies. The TDCR methodology is based on three fundamental assumptions: the statistics of the emitted light (Photon Emission), the detection threshold of the counter (Photon Detection) and the description of the scintillator non-linearity. The triple and double coincidence counting efficiencies are computed as a function of the free parameter ($\lambda$) by solving the following equations along with the experimental coincidence count rate data [7, 8].

$$\frac{\varepsilon_T}{\varepsilon_{AB}} = \frac{\int_0^{E_{max}} S(E)\left(1-e^{-\lambda_A EQ(E)}\right)\left(1-e^{-\lambda_B EQ(E)}\right)\left(1-e^{-\lambda_C EQ(E)}\right)dE}{\int_0^{E_{max}} S(E)\left(1-e^{-\lambda_A EQ(E)}\right)\left(1-e^{-\lambda_B EQ(E)}\right)dE} = \frac{N_T}{N_{AB}} \tag{1.1}$$

$$\frac{\varepsilon_T}{\varepsilon_{BC}} = \frac{\int_0^{E_{max}} S(E)\left(1-e^{-\lambda_A EQ(E)}\right)\left(1-e^{-\lambda_B EQ(E)}\right)\left(1-e^{-\lambda_C EQ(E)}\right)dE}{\int_0^{E_{max}} S(E)\left(1-e^{-\lambda_B EQ(E)}\right)\left(1-e^{-\lambda_c Q(E)E}\right)dE} = \frac{N_T}{N_{BC}} \tag{1.2}$$

$$\frac{\varepsilon_T}{\varepsilon_{AC}} = \frac{\int_0^{E_{max}} S(E)\left(1-e^{-\lambda_A EQ(E)}\right)\left(1-e^{-\lambda_B EQ(E)}\right)\left(1-e^{-\lambda_C EQ(E)}\right)dE}{\int_0^{E_{max}} S(E)\left(1-e^{-\lambda_A EQ(E)}\right)\left(1-e^{-\lambda_C EQ(E)}\right)dE} = \frac{N_T}{N_{AC}} \tag{1.3}$$

where

- $\varepsilon_T$ = triple coincidence efficiency
- $\varepsilon_{AB}, \varepsilon_{BC}, \varepsilon_{AC}$ = double coincidence efficiency between the PMTs A & B, B & C and A & C respectively

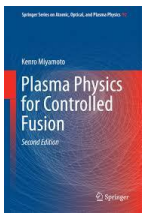


6

OPEN ACCESS
IOP Publishing
Plasma Physics and Controlled Fusion
Plasma Phys. Control. Fusion **65** (2023) 075010 (12pp)
https://doi.org/10.1088/1361-6587/accfbd

# Development of a portable pulsed fast ⩾$10^6$ neutron generator based on a flexible miniature plasma focus tube

**Ram Niranjan**[1,*], **Rohit Srivastava**[1], **J Joycee**[1] **and K D Joshi**[1,2]

[1] Applied Physics Division, Bhabha Atomic Research Centre, Mumbai 400085, India
[2] Homi Bhabha National Institute, Mumbai 400094, India

E-mail: niranjan@barc.gov.in

Received 20 December 2022, revised 10 April 2023
Accepted for publication 24 April 2023
Published 30 May 2023


**Abstract**

A plasma focus device is a laboratory fusion device that is used to produce pulsed neutrons for a few tens of ns duration. A compact plasma focus tube (volume ≈ 130 $cm^3$) has been developed, and this was connected to a newly developed capacitor bank using 24 coaxial cables, each 10 m long. The capacitor bank was of compact size and consisted of four energy storage capacitors (each 6 $\mu$F, 20 kV, size: 20 cm × 20 cm × 30 cm). The peak discharge current of the capacitor bank was estimated to be 176 kA with a rise time of around 3.6 $\mu$s at maximum 4.8 kJ operation energy. The average neutron yield was observed to be maximum (3.1 ± 1.0) × $10^6$ neutrons/pulse with a pulse duration of 15–25 ns at an operating energy of 2.7 kJ (15 kV) and deuterium gas filling pressure of 4 mbar. Long coaxial cables allow only the plasma focus head (neutron source) to be moved as per need, making this a portable pulsed neutron source that is useful in many applications, including in extreme conditions, such as in borehole logging applications for oil and mineral mapping. This report describes the various components of this portable neutron generator together with its neutron emission characteristics.

Keywords: pulsed neutrons, plasma focus, nuclear fusion

(Some figures may appear in colour only in the online journal)

## 1. Introduction

Portable fast neutron generators (PFNGs) have been proven to be a technically as well as commercially viable alternative to conventional neutron sources, such as Pu–Be, Am–Be and $^{252}$Cf, in many applications covering vast areas, including security [1–3], industry [4], environmental and geological fields [5], medical fields, especially in biophysics [6, 7], and in boron neutron capture therapy [8] among others. Among the various PFNGs, compact light-ion accelerator-based hermetically sealed tubes that use deuterium–deuterium (D–D) and deuterium–tritium (D–T) fusion reactions have found the most widespread use [8–13]. These accelerators generate neutrons of energies ∼2.45 MeV and ∼14.1 MeV, respectively. This consists of a source able to generate positively charged ions, one or more devices to accelerate the ions, and a metal hydride target loaded with either deuterium or tritium or a mixture of the two. An alternative to this is the dense plasma focus (PF)device based [14] portable pulsed ∼2.45 and ∼14.1 MeV neutron generator, which uses the same fusion reactions in $D_2$ and/or D–T mixture gases, respectively. Unlike in accelerator-based sealed neutron tubes, ions are self-accelerated in the plasma focus device to high energies (a few keV to several hundred keV) due to its geometry and produce intense neutrons for a short duration (typically a few 10 s ns). The plasma focus device is simple in operation as well as

* Author to whom any correspondence should be addressed.



 

economical as most of its components are either replaceable at a low cost or designed for long and repetitive operations.

Together with pulsed intense neutrons, the plasma focus device is a widely known pulsed source of ions, electrons and soft as well as hard x-rays. They have routinely been used for several applications, such as lithography [15], radiography [16], material processing and thin film depositions [17], irradiation on materials for the first wall of upcoming fusion reactors [18–20] and in biological and biomedicine research [21–24]. In view of this, plasma focus devices continue to be designed and developed with different geometries and with different radiation yields that, suitable for use in the above-mentioned applications.

Numerous portable pulsed neutron generators of neutron yield ~$10^6$ neutrons/pulse or less based on the plasma focus device have been developed worldwide in different laboratories [25–32]. For example, Silva *et al* [25] reported a maximum neutron yield of $(1.06 \pm 0.13) \times 10^6$ neutrons/shot at 9 mbar filling pressure of $D_2$ gas in a very small and fast plasma focus device operated at ~400 J. Similarly, Milanese *et al* [26] reported the design, construction and experimental study of a very small transportable dense plasma focus device with 125 J of energy as an intense, fast neutron source of yield ~$10^6$ neutrons/pulse. In another report [27], a compact and portable pulsed neutron source was reported to generate an average neutron yield of $(1 \pm 0.27) \times 10^4$ neutrons/shot at 200 J of bank energy. Rout *et al* [28] designed and developed a compact and portable sealed-type PF device, which could generate $10^5$–$10^6$ neutrons/pulse at 200 J of bank energy for 150 discharges for a single filling. Neutron emission of more than $10^4$ neutrons/shot from a table-top plasma focus device of size 25 cm × 25 cm × 50 cm at only tens of joules energy was reported by Soto *et al* [29]. Soto *et al* [33] reported on the neutron emission from the smallest plasma focus device in the world (size: ~20 cm × 20 cm × 5 cm) operating only at 0.1–0.2 J. A total neutron yield of (100 ± 40) neutrons/pulse was reported to be produced using this device at an operating energy of 0.1 J (4.9 nF, 6.5 kV), which can further be increased if operated repetitively.

Portability in all the above-mentioned devices has been achieved mostly through the use of a compact capacitor bank operating at sub-joule to a few hundred joules with an appropriately matched plasma focus unit. A typical plasma focus unit consists of a pair of coaxial electrodes working as the anode and the cathode, and an insulator sleeve placed in between them at the bottom [14]. The cathode is either designed in a tubular shape or in the form of a squirrel cage consisting of multiple rods. The majority of the low-energy plasma focus devices have used a tubular-shaped cathode as it also works as the experimental plasma chamber, which helps in achieving the desired compactness in a portable neutron source. A compact and coaxial spark gap is generally used for fast transfer of the capacitor bank energy to the plasma focus unit. The overall dimension is minimized by connecting all three main components, i.e. the capacitor bank, the spark gap and the plasma focus unit, using parallel plate transmission lines in a compact and rigid geometry. Moreover, these devices are mostly operated with battery-powered supplies, making them suitable for use in those field applications where a low to moderate neutron yield is required. However, high electromagnetic noise generated during capacitor bank discharge has been an issue in applications that require a high signal-to-noise ratio (S/N) because of its proximity to the plasma focus unit. In addition, the capacitor bank and other associated high-voltage (HV) components of the portable plasma focus devices may not be compatible for use in extreme conditions, such as a neutron probe tool in borehole logging for deep geological surveys to find deep ore deposits and petroleum reservoirs [34, 35], as high moisture among other factors severely effects its electrical operation in such conditions.

Taking into consideration the above-mentioned limitations, an electromagnetic-interference proof and HV safe pulsed neutron generator based on a flexible miniature plasma focus tube has been developed. A tubular-shaped miniature plasma focus tube of size 5 cm diameter × 16 cm length and weight around 1.2 kg has been connected to a compact capacitor bank of size around 40 cm × 40 cm × 30 cm using 10 m long commercially available RG213 coaxial cables. The long coaxial cables provide the desired flexibility to move the plasma focus tube to any specific location in 10 m radius, as well as to reduce the effects of EMIs, as the outer conductor of the cables also helps to partially screen the electromagnetic noise generated during the capacitor-bank discharge. Here, the plasma focus tube shall be at HV for only a short duration of a few microseconds, making this useful as a neutron probe tool in extreme conditions without any change in electrical characteristics and, in turn, neutron emission characteristics. Moreover, isolation of the plasma focus tube and the capacitor bank makes handling of the portable neutron generators safe from any electrical hazard, which was otherwise not possible with other available portable neutron generators, where the capacitor bank and the plasma focus unit were held together in a compact geometry. The present report includes a detailed description of the major components of the portable plasma focus device, i.e. the plasma focus tube design, the capacitor bank and the spark gap, followed by experimental observations of time-resolved and time-integrated neutron emission characteristics in the subsequent sections.

## 2. Experimental setup

A schematic and a photograph of the newly developed portable pulsed neutron generator are depicted in figures 1 and 2, respectively. The main components of the portable pulsed neutron generators are the capacitor bank, the triggerable spark gap switch and the plasma focus tube. All these components have been indigenously designed and developed. A compact DC HV power supply has been used to charge the capacitor bank to the desired voltage and to supply a fast negative trigger pulse to trigger and close the spark gap switch. All the electrical operations were performed remotely using a hand-held control unit.

The capacitor bank was assembled using four energy storage capacitors connected in parallel. The capacitors were custom-made for fast high-discharge current, thus were

7

IOP Publishing Mater. Res. Express 10 (2023) 075102 https://doi.org/10.1088/2053-1591/ace9ae

Materials Research Express

PAPER

# Distinction between low-barrier hydrogen bond and ordinary hydrogen bond: a case study of varying nature of charge assisted hydrogen bonds of diglycine perchlorate crystal

**Rajul Ranjan Choudhury**[1], **R Chitra**[1] and **Lata Panicker**[2]

[1] Solid State Physics Division, Bhabha Atomic Reserach Center, Trombay, Mumbai-400085, India
[2] Radiation Biology and Health Sciences Division, Bhabha Atomic Reserach Center, Mumbai-400085, India

**E-mail:** rajul@barc.gov.in

**Keywords:** hydrogen bond, double well potential, proton delocalization

OPEN ACCESS

RECEIVED
2 May 2023

REVISED
22 June 2023

ACCEPTED FOR PUBLICATION
21 July 2023

PUBLISHED
31 July 2023



## Abstract

Hydrogen bonding is a complex phenomenon that is a resultant of many energy components like the electrostatic, dispersive, covalent, charge cloud overlap repulsion etc, nature of hydrogen bond (H-bond) depends on which of these components play a dominant role. Low barrier hydrogen bond (LBHB) constitutes a special category of hydrogen bonds characterized by near delocalization of proton between donor and acceptor groups of the H- bond unlike an ordinary hydrogen bond (OHB) having proton clearly localized near the donor group. The significance of LBHBs in macromolecular interactions has been highly controversial, despite may attempts the existence and potential importance of protein LBHBs remains debatable. In order to answer questions like whether or not a distinct class of LBHBs exists and if they do exist under what conditions they are formed and how do they behave differently from OHBs, a detailed study of H-bonding in Diglycine Perchlorate (DGPCl) crystal containing five unique hydrogen bonded glycinium-glycine pairs is undertaken. All O-H–O bonds of DGPCl are between the carboxyl (-COOH) and carboxylate ($-COO^-$) groups with slightly different electron distributions resulting in observable variations in the H-bond geometries, this is an indication of varying strength of these short strong H-bonds. It is found that LBHB nature of the five O-H—O bonds between glycinium-glycine pairs (P1-P5) varies as P1 < P4 < P2 < P3 < P5. This study gives an experimental evidence of the existence of LBHBs and demonstrates that the behaviour of LBHBs is very different from that of strong OHBs.

## Introduction

Hydrogen bonds are arguably the most enigmatic and versatile intermolecular interactions [1], they play a fundamental role in biochemical processes hence in order to understand the biophysical systems it becomes important to study the nature of these interactions minutely. Nature of hydrogen bonds particularly the strong ones is complex, it is a resultant of many interactions like the electrostatic, dispersive, covalent, charge cloud overlap repulsion etc Low barrier hydrogen bond (LBHB) constitutes a special category of hydrogen bonds characterized [2, 3] by near delocalization of proton between donor and acceptor groups of the hydrogen bond, it is assumed that potential energy landscape for these hydrogen bonds has a double minimum form where the barrier height between the two minima is of the order of zero point energy of the proton. Role of LBHB in enzyme studies is an ongoing topic of interest, as LBHB has been proposed to play a major factor in enzyme catalysis through transition state stabilization; these hydrogen bonds can also play a role in proton conductivity within molecular clusters. In order to consider LBHB as a distinct class of hydrogen bond they should have some unique characteristic not present in ordinary hydrogen bonds (OHB) that have proton clearly localized near the donor group. It was shown by Warshel and Papzan [4] that the novel aspect of LBHB is a more covalent character accompanied by a more disperse charge distribution resulting in different energetic especially in response to its environment. It has been proposed earlier [5] that hydrogen bonding and proton transfer reactions can be

IOP Publishing Mater. Res. Express 10 (2023) 075102 R R Choudhury et al

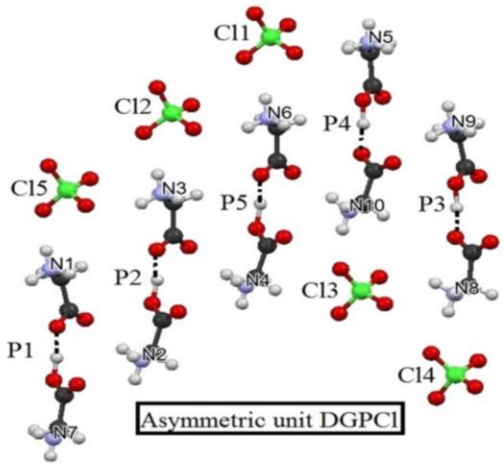


**Figure 1.** Asymmetric Unit of DGPCl.

described by Empirical Valence Bond models involving valence bond states, according to the three-orbital four electron model for hydrogen bond X–H–Y following three valence bond states are involved in the Hamiltonian

$$\psi_1 = X - H\ Y^{-} \psi_2 = X^{-}H - Y\ \psi_3 = X^{-}H^{+}\ Y^{-}$$

For ordinary hydrogen bonds with negatively charge acceptor the charge is primarily concentrated at the acceptor end (Y) this corresponds primarily to the resonance structure $\psi_1$ in contrast for LBHB the charge is spread out because of charge transfer effects hence the situations corresponds more towards the resonance structure $\psi_3$.

The significance of LBHBs in macromolecular interactions has been highly controversial [6], despite may attempt the existence and potential importance of protein LBHBs remains debatable. One reason for this is that clear experimental evidence of LBHB in macromolecular crystallography is rare since firstly it is proposed to exist in the transition state only which is difficult to crystallize and secondly even the best x-ray structures of macromolecules do not give H atom positions precisely. Hence in order to answer questions like whether or not a distinct class of LBHBs exists and if they do exist under what conditions they are formed and how do they behave differently from OHB one has to fall back to studying small molecular structures proposed to contain LBHBs.

Diglycine perchlorate (DGPCl) is one such small molecular structure that gave us an opportunity to study subtle differences in the nature of short strong hydrogen bonds, the structure contains five unique charge assisted hydrogen bonds [7], each of these hydrogen bonds have the potential to be a LBHB. DGPCl is a crystalline adduct obtained from 2:1 aqueous solution of Glycine and Perchloric [8] acid. Its crystal structure [8] is Triclinic with space group P-1, an asymmetric unit (figure 1) of DGPCl has five strongly hydrogen bonded positively charged glycinium-glycine pairs (P1-P5) and five negatively charged perchlorate ions. Table 1 gives structural details for the five O-H–O hydrogen bonds between the carboxyl (-COOH) and carboxylate ($-COO^{-}$) groups of glycinium-glycine pairs of DGPCl at two different crystal temperatures 293 K and 150 K. Carboxyl-Carboxylate supramolecular motifs [9] are important synthon in bimolecular systems, O-H–O bond between the carboxyl and carboxylate groups has the potential to be a LBHB [6] since the primary requirement for the formation of LBHB [4] namely a close matching of pKa values of the donor and acceptor groups can be easily satisfied in this case.

## Computation method

In order to obtain the properties like partial atomic charges, bond orders etc for the atoms and bonds of the glycinium-glycine pair PM6 semi-empirical quantum calculation method [10] as implemented in software MOPAC2016 [11] is used. Experimentally obtained molecular geometry of the glycinium-glycine pair is used in the calculation. Table 2 lists these properties for the atoms and bonds involved in O-H–O H-bonds of DGPCl. Hydrogen bond stabilization energy $E_{HB}$ resulting due to O-H–O bond between Glycinium ($Gly^{+}$) and Glycine

JES
Journal of the Electrochemical Society

8

*Journal of The Electrochemical Society*, 2023 **170** 113503

# Efficient Plutonium Extraction and Electrochemical Insights in a Hydrophobic Deep Eutectic Solvent for Radioactive Waste Management

**Sushil M. Patil,[1,2] Kavitha Jayachandran,[1] Manjulata Sahu,[2,3] and Ruma Gupta[1,2,z]**

[1]*Fuel Chemistry Division, Bhabha Atomic Research Centre, Trombay, Mumbai-400085, India*
[2]*Homi Bhabha National Institute, Training School Complex, Anushakti Nagar, Mumbai 400094, India*
[3]*Radio Analytical Chemistry Division, Bhabha Atomic Research Centre, Trombay, Mumbai-400085, India*

In this study, we explore the extraction and electrochemical characteristics of Plutonium using a hydrophobic deep eutectic solvent (DES) consisting of tetra-Butyl Ammonium Bromide(TBABr) as the hydrogen bond acceptor and Decanoic acid (DA) as the hydrogen bond donor in a 1:2 ratio composition. Hydrophobic DES possesses unique attributes, such as low volatility and a high affinity for metal ions, making it a promising choice for Plutonium extraction. We systematically investigate the influence of various parameters, including DES composition, acid concentration, and extraction duration. Our extraction experiments reveal that the hydrophobic DES exhibits its maximum Plutonium extraction efficiency (95%) at a 4 M $HNO_3$ concentration, with a distribution coefficient (D) reaching nearly 71. To gain insights into the electrochemical behavior of Plutonium within the hydrophobic DES, we conduct cyclic voltammetry experiments. The resulting voltammograms offer valuable insights into the redox properties and stability of Plutonium species within the DES. Furthermore, we analyze the impact of potential scan rate on the electrochemical response, shedding light on the kinetics and mechanisms underlying Plutonium electrochemistry within the hydrophobic DES. These findings underscore the considerable potential of hydrophobic DES for efficient Plutonium extraction and electrochemical separation. This research contributes to the development of sustainable and environmentally friendly approaches for managing Plutonium, particularly in the context of nuclear waste disposal

 [DOI: 10.1149/1945-7111/ad0adc]

Manuscript submitted July 13, 2023; revised manuscript received October 27, 2023. Published November 21, 2023.

Supplementary material for this article is available online

The extraction and separation of Plutonium from radioactive waste play a critical role in nuclear waste management.[1,2] Plutonium, a highly radioactive and long-lived element, poses significant environmental and health risks if not properly handled and disposed of.[3–5] Therefore, developing efficient and sustainable methods for Plutonium extraction is of utmost importance. Conventional methods for Plutonium extraction from radioactive waste often involve complex chemical processes, which are time-consuming, resource-intensive, and generate large amounts of secondary waste.[6–11] As a result, there is a growing interest in exploring alternative approaches that are more environmentally friendly and economically viable.[12–14] One promising avenue for Plutonium extraction is the use of hydrophobic deep eutectic solvents (DES).[15,16] The DES are solvents formed by simply mixing relatively cheap starting materials(quaternary ammonium, sulphonium or phosphonium salts as hydrogen bond acceptor (HBA) with hydrogen bond donor (HBD) such as organic acid, amine, amide, etc) with 100% atom economy, hence no further purification is required.[17–20] The resulting viscous liquid, characterized by large depression in freezing point, even lower than the melting points of the individual components of the mixture, as a consequence of strong H-bonding between constituents of the mixture.[15,17,18,21,22] DESs are a class of solvents that exhibit unique properties, such as low volatility and high solubility for metal ions.[15,21–26] These solvents have gained attention in recent years due to their potential as green alternatives to traditional organic solvents.[27–37]

In this research paper, we investigate the extraction and electrochemical behavior of Plutonium in a tetra-Butyl Ammonium Bromide and Decanoic Acid (TBABr-DA (1:2)) based hydrophobic deep eutectic solvent (DES) for radioactive waste management. Our study aims to evaluate the efficiency of the hydrophobic DES in extracting Plutonium from radioactive waste and gain insights into its electrochemical behavior. Herein, the synthesis and characterization of the hydrophobic DES based on tetra-Butyl Ammonium Bromide as hydrogen bond acceptor and Decanoic acid as hydrogen bond donor (TBABr-DA (1:2)) is presented. The composition and physicochemical properties of the DES are investigated to understand its potential for Plutonium extraction. Through a series of extraction experiments; we systematically evaluated the efficiency of the hydrophobic DES in extracting Plutonium from simulated radioactive waste. Various parameters, including DES composition, concentration of nitric acid and extraction time, are investigated to optimize the extraction process. The extraction yields are quantified, and the effectiveness of the hydrophobic DES in Plutonium extraction is assessed.

In addition to extraction studies, we also explore the electrochemical behavior of Pu(IV)/Pu(III) redox couple in the hydrophobic TBABr-DA DES. Cyclic voltammetry experiments provide valuable insights into the redox behavior and stability of Plutonium (IV) species in the synthesized DES. The effect of potential scan rate on the electrochemical response is investigated to elucidate the kinetics and mechanism of Plutonium electrochemistry in the hydrophobic DES. These studies open avenues to explore and understand the potential of using the hydrophobic DES as an electrolyte medium for electrochemical separation of Plutonium. By applying a suitable potential, the selective deposition of Plutonium onto an electrode surface, enabling its separation from other metal ions present in the radioactive waste can be achieved. The findings of this paper contribute to the development of sustainable and environmentally friendly approaches for Plutonium management in the context of nuclear waste disposal. The efficient Plutonium extraction and electrochemical insights gained from the hydrophobic DES open up new possibilities for more efficient and cost-effective strategies for radioactive waste treatment.

## Experimental

All the experiments were performed in a radioactive fume hood, in order to prevent risk of contamination due to the use of Plutonium. $^{239}Pu$ is an $\alpha$-active nuclide with a half-life of $2.46 \times 10^4$ years.

[z]E-mail: rumac@barc.gov.in

*Journal of The Electrochemical Society*, 2023 **170** 113503

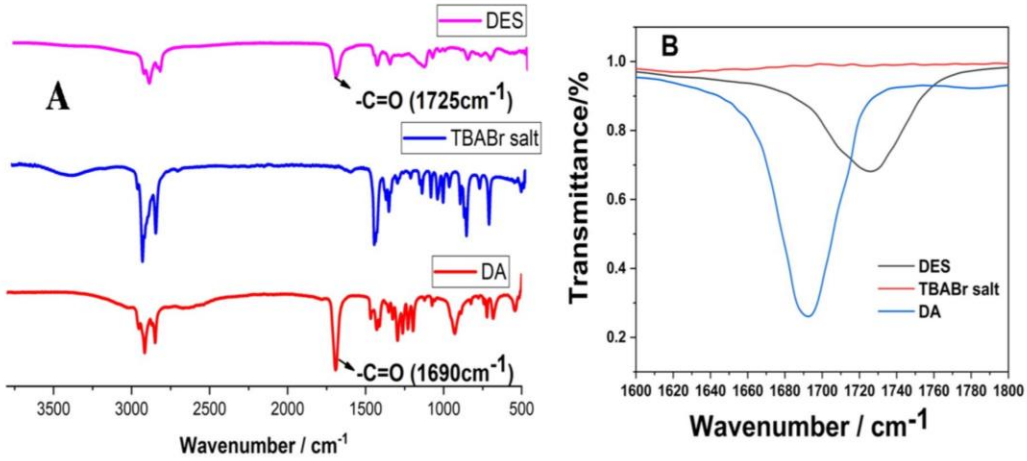


**Figure 1.** Comparison of FTIR spectra of (A) TBABr salt, decanoic acid and DES (B). Zoomed image for C=O bond interaction.

***Reagents and solutions.***—Tetrabutyl ammonium bromide (TBABr) (99% purity, CAS number 1643-19-2) and Decanoic acid (DA) (99% purity, CAS number 334-48-5), were purchased from Sigma-Aldrich, and used without further purification. Nitric Acid ($HNO_3$) was of G. R. (Guaranteed Reagent) grade and used as received. All the solutions were prepared in Millipore Milli-Q water (~18 MΩ cm).

***Apparatus.***—Thermogravimetry and differential scanning calorimetry was performed using a Differential scanning calorimeter (DSC-I) supplied by M/s Metter Toledo, Switzerland, under the flow of high-purity argon at a flow rate of 0.02 $dm^3$ $min^{-1}$.Voltammetric studies of the solutions were recorded using CHI 760D electrochemical work station at room temperature with a three electrode system. A Platinum disk electrode (area, A = 0.0314 $cm^2$) was used as working electrode. It was polished using alumina powder (CH Instruments, Inc.) of decreasing particle size from 1.0 to 0.05 $\mu$m and was sonicated in water after each polishing step to remove any adhering alumina particles. Then, it was electrochemically cleaned by potential cycling between 1.6 and −0.5 V for 20 cycles in 1 M $H_2SO_4$. This procedure of cleaning was repeated until a reproducible response of Pt electrode was observed in 1 M $H_2SO_4$. A platinum coiled wire was used as counter electrode and a platinum wire was used as quasi reference electrode. All the redox potentials were referred against $Fc/Fc^+$. Each measurement was repeated thrice and the average numerical value of each parameter is quoted for discussion with a relative error < 0.1%. The electrochemical cell had a single leak-tight compartment and all the electrodes were placed in the same compartment. The experiments were carried out at room temperature (25 1 °C) and the electrochemical cell was kept under argon atmosphere during entire study. FT-IR (Fourier Transform Infrared) spectra were recorded on ATR mode using Alpha FTIR spectrometer from Bruker. The UV–Visible spectra of TBABr-DA DES before and after extraction of Pu from aqueous $HNO_3$ solution were recorded using UV–VIS-NIR light source DH-2000-BAL Ocean Optics spectrophotometer with QE 65,000 detector. Density and viscosity were determined using an Anton Par Viscometer.[17–19]

***Synthesis of TBABr:DA (1:2) DES.***—The deep eutectic solvents were synthesized by the mechanochemical method. The hydrogen bond acceptor (Tetrabutyl ammonium bromide salt) and hydrogen bond donor (Decanoic acid) were mixed together at different molar ratios (1:1, 1: 1.5, 1:2, 1:3, 1:4) using mortar-pestle and then was stirred further at 50 °C until the formation of a colorless liquid, then kept at room temperature for 24 h (Scheme S1, ESI). The DES of molar composition (1:2) was a stable liquid at RT and this DES was used for further experiments.

***Preparation of Pu(IV) solution.***—The working reference, potassium Plutonium sulphate dehydrate ($K_4Pu(SO_4)_4.2H_2O$) was prepared in our laboratory as describedelsewhere.[38] In brief, crystals of ($K_4Pu(SO_4)_4.2H_2O$) were first prepared by the slow evaporation of 1 M $H_2SO_4$ containing$K_2SO_4$ and $Pu(SO_4)_2$ in a 2:1 molar ratio. Then the crystals were washed several times with absolute alcohol and dried in a current of air. The anhydrous $K_4Pu(SO_4)_4$ was prepared by heating the hydrated crystals at 340 °C for about three hours until constant weight. A known amount of the anhydrous standard $K_4Pu(SO_4)_4$ was quantitatively dissolved in3M $HNO_3$ to achieve a Pu concentration 0.15 mg $ml^{-1}$.

## Results and Discussion

The formation of an ammonium-based deep eutectic solvent (DES) with a ratio of 1:2 was confirmed by FT-IR analysis, aiming to understand the hydrogen bonding interactions responsible for the decrease in the melting point of the mixture at the eutectic composition compared to that of the pure components. As depicted in Fig. 1A, a noticeable shift in the carbonyl stretching peak in the DES towards a higher wave number is observed in comparison to pure DA. This significant shift, as zoomed in Fig. 1B, is believed to be a result of the weakening of the C=O bond strength due to hydrogen bonding between the bromide anion of the salt and DA ($–O–H_{DA}$ $–Br_{salt}$). Furthermore, in the FT-IR spectra, the prominent C–H bands at approximately 2920 $cm^{-1}$ (CH3/CH2 asymmetrical stretching vibrations) and 2850 $cm^{-1}$ (CH2 symmetric stretch) show no significant changes in the DES compared to the FT-IR spectra of the pure components (TBABr and DA), indicating that these bonds are not involved in hydrogen bonding.

Physiochemical properties such as melting point, density and viscosity plays crucial role in determining the speciation parameters and its evaluation is helpful in accurate depiction of interactions. The temperature range of application of any DES depends on its thermal stability. Hence the thermal stability of DES formed between decanoic acid and TBABr was investigated with Thermogravimetry experiment. The presence of any low temperature phase transitions and melting point was investigated by Differential Scanning Calorimeter (DSC). Both experiments in DSC and TGA were carried out at identical rate of heating and cooling of 5 K.$min^{-1}$. The thermograms obtained from the reversible run in DSC and the heating run in TG-DSC are given in Figs. 2A & 2B respectively. In Fig. 2A, DSC curve showed a hump before the melting peak which occurred at −2.34 °C. The hump may be

JES
Journal of the Electrochemical Society

9

*Journal of The Electrochemical Society*, 2023 **170** 124515

# Investigations on CuCl/HCl Electrolysis Using a Pt/C Electrocatalyst-based Membrane Electrode Assembly

**Atindra Mohan Banerjee,[1,2,z] Rajini P. Antony,[3] Ashish Nadar,[1] V. M. Tripathi,[1] S. Aich,[1] M. R. Pai,[1,2] and A. K. Tripathi[1,2]**

[1]*Chemistry Division, Bhabha Atomic Research Centre, Mumbai 400085, India*
[2]*HomiBhabha National Institute, Anushaktinagar, Mumbai 400094, India*
[3]*Water and Steam Chemistry Division, Bhabha Atomic Research Centre, Mumbai 400085, India*

The study reports the fabrication and performance evaluation of a Pt/C(Electrocatalyst) (20 wt% Pt)/Nafion MEA as cathode for CuCl/HCl electrolysis in a PEM-based electrolyser with an active area of ~4 $cm^2$. The electrolyser is indigenously developed consisting of graphite plates with serpentine fluid flow channels grooved. The anode half-cell reaction i.e. $Cu^+$ oxidation is investigated by electrochemical (LSV, CV, EIS) methods, and I-V characteristics. An oxidation peak for $Cu^+$ to $Cu^{2+}$ is observed at a cell voltage of ~0.55 V in the LSV curve recorded at 20 $mVs^{-1}$ in the electrolyser with an anolyte of 0.2 M CuCl in ~2 M HCl flowing at 2.2 ml $min^{-1}$. The effect of the concentration of CuCl in the anolyte and its flow rate is also studied. A current density of ~128 $mAcm^{-2}$ is attained for CuCl/HCl electrolysis at a cell voltage of 1 V with an anolyte of 0.4 M CuCl in ~4 M HCl flowing at 8.8 ml $min^{-1}$. Further, a model showing the working of the above electrolyser is generated using COMSOL 6.0. Higher concentration of CuCl in the anolyte and higher anolyte flow rates favoring the electrolysis is evident from electrochemical characterizations.

 [DOI: 10.1149/1945-7111/ad11ae]

Manuscript submitted May 23, 2023; revised manuscript received October 24, 2023. Published December 19, 2023.

Supplementary material for this article is available online

The global energy demand is continually increasing due to increasing population and improvement in human lifestyle.[1,2] To cope up with this energy demand, widespread utilization of fossil fuel based energy resources is taking place worldwide. This has resulted in climate change i.e., global warming due to increased concentration of green house gases in the Earth's atmosphere consequential to the extensive consumption of fossil fuels.[3] Besides, the reserve of fossil fuel in Earth is limited by inadequate resources in comparison to the increasing demand. A heterogeneous geographical distribution of fossil fuel stocks and fluctuations in its price are common. In view of all these concerns the scientific community at present is exploring alternative renewable energy systems to address future energy and environmental issues and achieve asustainable energy solutions combined with suitable environmental benefits. Solar energy can effectively resolve this with its enormous potential with a power capacity of ~120,000 TW reaching the Earth's surface.[4,5] However in order to deal with the intermittency of the availability of solar energy, its storage in the form of chemical fuels generated from solar energy for future use seems to be the most viable, sustainable and green solution.[6,7] One such promising energy carrier or fuel is hydrogen and if it can be generated from water utilizing solar energy it has a complete scope to replace the present liquid fuel in the transportation and even other sectors with both sustainability and environmental security.[8–11]

Hydrogen has a very high calorific value of ~142 MJ $Kg^{-1}$. Energy conversion of solar to hydrogen via water splitting is a sustainable and environment friendly process. Solar energy is a renewable energy source and water, a renewable hydrogen resource without any major emission issues. Solar water splitting is thermodynamically feasible as theoretically it requires 1.23 eV.[12] Hydrogen can be generated from water using solar energy by diverse methodologies viz. photovoltaic coupled electrolysis,[13] photoelectrochemical,[14,15] photocatalytic,[16–18] microwave assisted,[19] plasma assisted,[20] thermochemical.[21,22] Among these methods one promising option is thermochemical water-splitting (TWS) cycles as it possesses certain advantages over others e.g. appropriate operational temperatures (550 °C–1500 °C) for coupling to solar thermal systems or even advanced nuclear reactors, scaling up potentiality, high efficiencies and eliminating requirement of costly gas separating membranes as the products of water splitting are formed in separate chambers.[21–26] Among the thermochemical cycles the two step metal-metal oxide cycles,[27,28] iodine-sulfur and hybrid-sulfur cycles,[29–31] copper-chlorine cycle[24] demands special mention due to their higher efficiencies, scale of operation, feasibility and advanced stage of research. The lowest temperature demand among these thermochemical cycles is for the copper-chlorine (Cu-Cl) process where a maximum temperature of ~550 °C is required for closed loop operation for hydrogen generation. Thus, huge potential for coupling with solar thermal technology seems workable.[32–34] Further, coupling with advanced nuclear reactors to utilize high temperature heat for hydrogen generation is also a possibility and promising futuristic option.[35,36]

Figure 1a depicts the four-step hybrid Cu-Cl cycle, in which the hydrogen production step is the CuCl/HCl electrolysis generating $CuCl_2$ as the oxidised product and it is electrochemically accomplished. This is followed by the drying of the aqueous $CuCl_2$ which is then hydrolysed by water in the next step to produce $Cu_2OCl_2$ and HCl. Both these steps proceed by utilizing thermal energy. Finally, $Cu_2OCl_2$ undergoes thermolysis in the highest temperature step producing back CuCl for electrolysis and generating oxygen. All the chemicals except the input water and two products hydrogen and oxygen are recycled in this set of reactions with the net effect of water splitting into hydrogen and oxygen. Numerous experimental and numerical studies have been reported as part of development of this cycle viz. studies on individual steps, research on materials involved—catalyst, membranes, materials of construction etc, closed cycle demonstration issues, cost assessment, exergy analysis, coupling issues with solar/nuclear reactor and so on.[37–46] Evidently one important outcome from above studies and reviews is that among several issues to be resolved for Cu-Cl thermochemical cycle operation, quite a few concerns related to the hydrogen producing electrochemical step needs to be addressed viz. thermodynamic and kinetic issues, understanding fundamental reaction steps, optimization of operating parameters, solving material issues in high acidic environments (membrane, catalyst, cell components etc.), achieving high efficiencies to decrease electrical demand, designing electrolyzers, minimizing side reactions and undesired crossovers etc The

[z]E-mail: atinmb@barc.gov.in; atinmb@gmail.com

*Journal of The Electrochemical Society*, 2023 **170** 124515

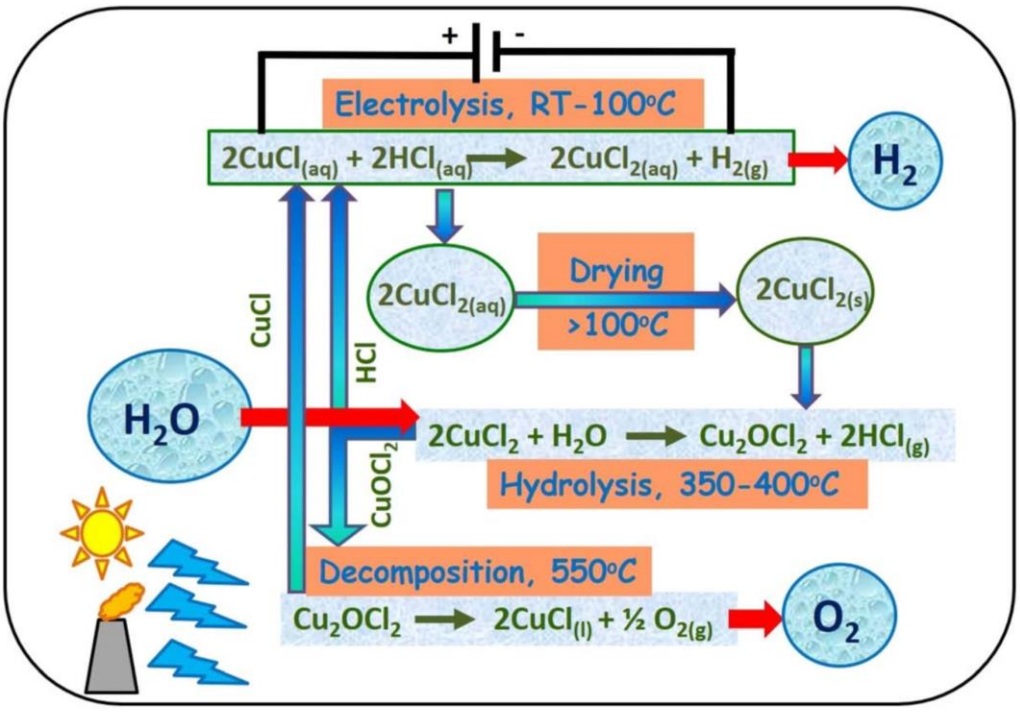


(a)

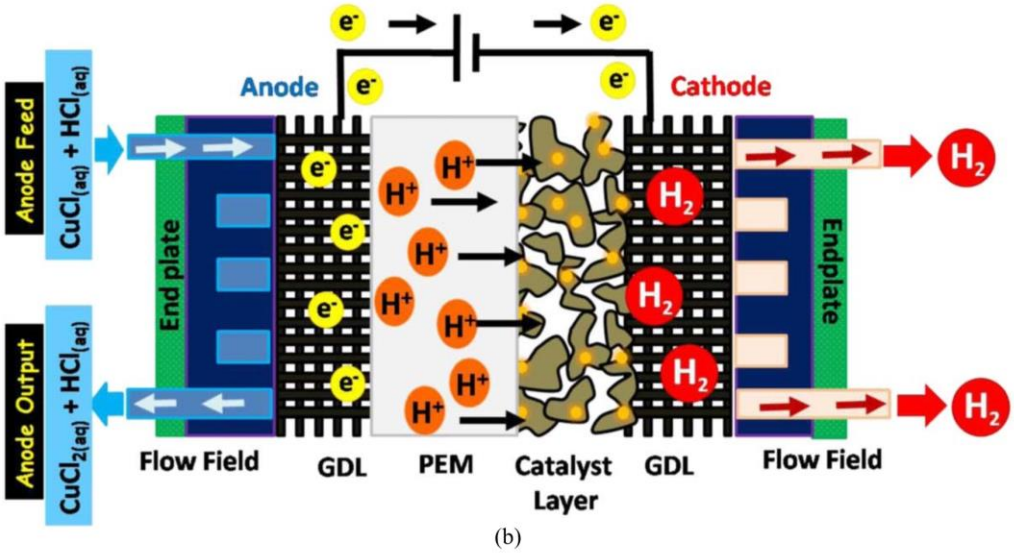


(b)

**Figure 1.** (a) Schematic representation of Cu-Cl thermochemical water spliting cycle. (b) Schematic representation of the principle of operation of a PEM based CuCl/HCl electrolyser.

scientific advances have been recently well reviewed in the articles by Li et al.[47] and Farsi et al.[43]

CuCl/HCl electrolysers uses the advanced concept of membrane electrode assembly (MEA) with cathode and anode flow field plates on either side as discussed elsewhere[48] and shown in Fig. 1b. In this principle of operation, the CuCl in aqueous HCl is fed into the anode compartment whereCuCl is oxidized to $CuCl_2$ generating electrons and protons. While the protons passes through the proton exchange membrane to the cathode surface, electrons conducts through the external circuit and hydrogen evolution reaction occurs at the cathode in presence of a catalyst. The net result of these two half cell reactions is the CuCl/HCl electrolysis.

Commercial MEA's based on Pt/C electrocatalyst has been generally employed in reported literature.[43,47,49–54] In our earlier study, we had employed a platinized Nafion membrane as MEA with electrocatalyst coated only on the cathode side.[48] In this study we

10

IOP Publishing Phys. Med. Biol. 68 (2023) 225005 https://doi.org/10.1088/1361-6560/ad00a4

Physics in Medicine & Biology

IPEM Institute of Physics and Engineering in Medicine

PAPER

# Microdosimetry-based investigation of biological effectiveness of $^{252}$Cf brachytherapy source: TOPAS Monte Carlo study

**Arghya Chattaraj**[1,2] **and T Palani Selvam**[1,2,*]

[1] Radiological Physics and Advisory Division, Health, Safety and Environment Group, Bhabha Atomic Research Centre, Mumbai 400085, India

[2] Homi Bhabha National Institute, Anushaktinagar, Mumbai 400094, India

* Author to whom any correspondence should be addressed.

**E-mail:** pselvam@barc.gov.in

**Keywords:** microdosimetry, Monte Carlo, RBE, quality factor, neutron, brachytherapy, TOPAS

CrossMark

OPEN ACCESS

RECEIVED
6 April 2023

REVISED
7 August 2023

ACCEPTED FOR PUBLICATION
5 October 2023

PUBLISHED
6 November 2023



## Abstract

*Objective.* To investigate biological effectiveness of $^{252}$Cf brachytherapy source using Monte Carlo-calculated microdosimetric distributions. *Approach.* $^{252}$Cf source capsule was placed at the center of the spherical water phantom and phase-space data were scored as a function of radial distance in water ($R$ = 1–5 cm) using TOPAS Monte Carlo code. The phase-space data were used to calculate microdosimetric distributions at 1 $\mu$m site size. Using these distributions, Relative Biological Effectiveness (RBE), mean quality factor ($\bar{Q}$) and Oxygen Enhancement Ratio (OER) were calculated as a function of $R$. *Main results.* The overall shapes of the microdosimetric distributions are comparable at all the radial distances in water. However, slight variation in the bin-wise yield is observed with $R$. RBE, $\bar{Q}$ and OER are insensitive to R over the range 1–5 cm. Microdosimetric kinetic model based RBE values are about 2.3 and 2.8 for HSG tumour cells and V79 cells, respectively, whereas biological weighting function-based RBE is about 2.8. ICRP 60 and ICRU 40 recommendation-based $\bar{Q}$ values are about 14.5 and 16, respectively. Theory of dual radiation action based RBE is 11.4. The calculated value of OER is 1.6. *Significance.* This study demonstrates the relative insensitivity of RBE, $\bar{Q}$ and OER radially away from the $^{252}$Cf source along the distances of 1–5 cm in water.

## 1. Introduction

Radiotherapy treatment using ionizing radiation having high or intermediate linear energy transfer (LET) demonstrates higher biological effectiveness as compared to conventional photon sources. The key advantages of using neutron sources for treatment are: (a) its high LET, and (b) unlike photons, the presence of oxygen in cells or tissues does not affect its biological effectiveness (Koh *et al* 1994, Srivastava *et al* 2014). Similar to photon-based brachytherapy sources such as $^{60}$Co, $^{137}$Cs, $^{192}$Ir, $^{169}$Yb, $^{125}$I and $^{103}$Pd etc, miniature $^{252}$Cf source is a potential brachytherapy source for interstitial implantation, external surface applications and intra-cavitary applications (Abd El-Hafez *et al* 1997). In addition to the wide applicability of $^{252}$Cf neutron sources in the field of research, medicine and industry (Maruyama and Beach 1986, Ghassoun *et al* 2010), it has also been used as a brachytherapy source since 1970 (Nagarajan *et al* 1971, Colvett *et al* 1972, Krishnaswamy 1972, Anderson 1973, 1974). $^{252}$Cf is a suitable neutron brachytherapy source because of its long half-life (2.6 years) and relatively high neutron yield (Wierzbicki *et al* 1997). The advantages and limitations of using $^{252}$Cf source for various brachytherapy applications were reported elsewhere (Maruyama and Beach 1986, Maruyama *et al* 1991, Wierzbicki *et al* 1994, Abd El-Hafez *et al* 1997, Rivard 2000, Ghassoun *et al* 2010, Lei *et al* 2011, Ghassoun 2013, Yadollahpour *et al* 2015, Zhou *et al* 2016, Qian *et al* 2017, Xiong *et al* 2017, Rasouli *et al* 2020, Karimi-Shahri *et al* 2021).

Several published studies were centered on radiobiological experiment-based investigation of Relative Biologic Effectiveness (RBE) of $^{252}$Cf brachytherapy sources (Hall *et al* 1974, Feola *et al* 1982, Maruyama *et al* 1983, Maruyama 1984, Maruyama *et al* 1991, Fairchald *et al* 1997, Wierzbicki 2012, Zhou *et al* 2016, Rasouli *et al* 2020, Karimi-Shahri *et al* 2021). Wang and Zhang (2004) developed a new formula based on the theory of

IOP Publishing Phys. Med. Biol. 68 (2023) 225005 A Chattaraj and T P Selvam

compound-dual-radiation-action to predict the cell-survival fraction for a mixed-radiation field of $^{252}$Cf. RBE of ionizing radiations can also be determined based on different models such as the Biophysical model, theory of dual radiation action (TDRA) and microdosimetric kinetic model (MKM) which use microdosimetric distributions as input parameters (Rossi 1979, Griffiths 1985, Zaider *et al* 1996, Wierzbicki 2012, Karimi-Shahri *et al* 2021). Microdosimetry is the evaluation of stochastic distribution of energy depositions at cellular and sub-cellular targets (Rossi 1979, Griffiths 1985, Zaider *et al* 1996). The lineal energy ($y$) is an important quantity for evaluation of radiation quality. As per ICRU Report 36 (Griffiths 1985), $y$ is defined as $y = \varepsilon/\bar{l}$, where $\varepsilon$ is the energy imparted to matter in the volume of interest by a single energy deposition event and $\bar{l}$ is the mean chord length of the target volume. $\bar{l} = \frac{2}{3}d$, where $d$ is site diameter. $\bar{y}_F = \int_0^\infty yf(y)dy$ is frequency-mean lineal energy and $\bar{y}_D = \int_0^\infty yd(y)dy$ is dose-mean lineal energy. $f(y)$ represents the number of events having event size between $y$ and $y+dy$ and $d(y) = \frac{yf(y)}{\bar{y}_f}$ is the dose probability density of $y$. The moments of $y$ distribution ($\bar{y}_F$ and $\bar{y}_D$) are indicative of RBE of ionizing radiation (Kellerer and Rossi 1974).

Although microdosmetric studies on $^{252}$Cf neutron sources related to radiation protection are reported (Rollet *et al* 2004, Zhang *et al* 2014, Chattaraj *et al* 2019a), a similar study for a $^{252}$Cf brachytherapy source has not been reported in the literature. The present study is aimed at calculating the biological effectiveness of a $^{252}$Cf brachytherapy source as a function of radial distance ($R$) in water phantom using microdosimetric technique. For this purpose, microdosimetric distributions at 1 $\mu$m site size as a function of $R$ in water are calculated using the Monte Carlo-based tool for particle simulation (TOPAS) and FLUKA codes. Biological effectiveness is quantified in terms of mean Quality Factor ($\bar{Q}$), *RBE* and Oxygen Enhancement Ratio (OER). In the present study, RBE is derived based on Biophysical model, MKM and TDRA. $\bar{Q}$ is calculated based on ICRP 60 and ICRU 40 recommendations using the microdosimetric distributions. Additionally, $\bar{Q}$ is derived based on distributions of unrestricted LET ($L_\infty$) in water and compared with the microdosimetry-based $\bar{Q}$ values. The study also demonstrates an efficient method for calculating microdosimetric distributions.

## 2. Materials and methods

### 2.1. $^{252}$Cf brachytherapy source and phantom models

The present study simulated the applicator tube (AT) $^{252}$Cf source capsule from Oak Ridge National Laboratory (ORNL). The source details were taken from Karimi-Shahri *et al* (2021) and schematic diagram of the source is shown in figure 1. The active core of the source capsule is a cylinder (1.5 cm length × 0.61 mm diameter) made of $Cf_2O_3$ of density 12 g cm$^{-3}$. The cylindrical active core is surrounded by a primary capsule followed by a secondary capsule. Both the primary and secondary capsules are made of Pt/Ir-10% mass having density of 21.51 g cm$^{-3}$. The inner and outer diameters of the primary capsule are 1.35 and 1.75 mm, respectively and its inner and outer lengths are 15.50 and 17.78 mm, respectively. The secondary capsule has inner and outer diameters of 1.80 and 2.80 mm, respectively, and inner and outer lengths of 17.82 and 23.14 mm, respectively. The gap between the primary and secondary capsules is filled with air (0.0012 g cm$^{-3}$). The rounded ends of capsules are welded. In addition, a bodkin evelet having diameter of 0.63 mm is embedded in the secondary capsule (Rivard *et al* 1999). The typical source strength of a remote after loading HDR capsule is 0.3–0.4 mg $^{252}$Cf and using advanced radiochemistry techniques, loading up to 1 mg of $^{252}$Cf per mm$^3$ is feasible (Rivard *et al* 1999).

$^{252}$Cf is produced in nuclear reactor. Cf source typically contains up to 85% of $^{252}$Cf and the remaining 15% is $^{249}$Cf, $^{250}$Cf, and $^{251}$Cf which have negligible dosimetric impact due to their long half-lives (Knauer and Martin 1997). $^{252}$Cf decays by spontaneous neutron fission (3.1%) and alpha emission (96.9%). The decay process of $^{252}$Cf includes emission of beta, prompt gamma up to 6.5 MeV and photons from fission products up to 2 MeV (Wierzbicki *et al* 1997). The neutron and photon yield from one $\mu$g of $^{252}$Cf are $2.31 \times 10^6$ neutrons s$^{-1}$ (Permar 1976) and $1.332 \times 10^{13}$ photons s$^{-1}$ (Wierzbicki *et al* 1997), respectively. For the encapsulated $^{252}$Cf brachy source, alpha and beta will be absorbed by the source capsule materials and hence not considered in the present study. Neutrons and photons can penetrate the encapsulation material and contribute in the total dose deposited. Rivard *et al* (1999) and Wierzbicki (2012) showed that approximately, 33% of the total absorbed dose is due to photon emissions. However, in terms of RBE weighted dose (absorbed dose × RBE), the relative contribution from photons will be very less as compared to neutrons. Note that the RBE and $\bar{Q}$ are sensitive to neutron energy and greater than unity whereas for photons, value of these parameters is unity, independent of photon energy (Karimi-Shahri *et al* 2021). Rasouli *et al* (2020) demonstrated that the contribution of neutrons to the total dose is maximum and the equivalent gamma dose is negligible when compared to those of neutrons. The above findings showed that in terms of RBE-weighted dose or equivalent gamma dose, relative contribution from neutrons is maximum as compared to photons. Hence, the present study considers only the neutron components of $^{252}$Cf. In the Monte Carlo calculations, the neutron energy


11

IOP Publishing Mater. Res. Express 10 (2023) 096513 https://doi.org/10.1088/2053-1591/acfae6

Materials Research Express

PAPER

# Nonlinear multivariate constitutive equations for modeling hot deformation behavior

OPEN ACCESS

RECEIVED
25 April 2023

REVISED
26 August 2023

ACCEPTED FOR PUBLICATION
18 September 2023

PUBLISHED
26 September 2023



**Parag M Ahmedabadi**

Materials Processing & Corrosion Engineering Division, Bhabha Atomic Research Centre, Trombay, Mumbai 400085, India

**E-mail:** aparag@barc.gov.in

**Keywords:** hot deformation, nonlinear constitutive models, multivariate constitutive models, Zener-Holloman parameter, activation energy

## Abstract

Nonlinear constitutive equations are proposed to model variations in flow stress as a function of strain rate and temperature during hot deformation. Modified constitutive are applied to seventy data sets about hot deformation of alloys. Two modifications to conventional constitutive models are introduced, viz. (1) nonlinear and (2) multivariate models with the fitting of flow stress simultaneously with two variables. The predictive accuracy of constitutive equations was evaluated using three statistical parameters and compared with a conventional Arrhenius-like model. It is shown that nonlinear constitutive equations have improved predictive accuracy for variations in flow stress during hot deformation. The advantages of multivariate models include less computation and material parameters that are constants independent of temperature or strain rate. In another type of multivariate model, flow stress is expressed as linear and nonlinear polynomial functions of the Zener-Holloman parameter. This approach gives a single value of the activation energy of hot deformation. The results have indicated that a generalized second-order multivariate constitutive equation can be used to better predict flow stress, as a function strain rate and temperature, during hot deformation.

## 1. Introduction

Hot working is a deformation of materials carried out at a combination temperature and strain rate such that substantial recovery occurs [1]. It is essential to select a suitable set of temperature and strain rate to impart considerable strain without appreciable strain hardening. Optimized sets of temperature and strain rate result in desirable mechanical properties. Owing to its importance for controlling final mechanical properties, hot deformation of alloys is an extensively studied field of materials processing [2–8]. Appropriate knowledge of material flow and microstructural behavior during hot working is crucial for selecting suitable temperatures and strain rates. It requires accurate modeling of variations in flow stress with temperature and strain rate (at different levels of strains) using constitutive equations. Such modeling helps in determining optimized hot working conditions and understanding underlying metallurgical processes like work hardening (WH), dynamic recovery (DRV), and dynamic recrystallization (DRX) [9].

Mathematical modeling of hot deformation is primarily focused on the prediction of flow stress as a function of strain rate ($\dot{\varepsilon}$), temperature ($T$), and strain ($\varepsilon$). Such models are generally referred to as constitutive models [10]. Commonly used constitutive models for prediction of flow stress are Arrhenius-type model [11–15], Johnson-Cook [16, 17], Fields-Backofen [18–21], and Zerilli-Armstrong [22, 23] models. In addition, models based on artificial neural network [24–26] and physical-based models [27–29] are also widely used. A brief review of most models is given in [30].

Arrhenius-type model is used extensively in studying hot deformation. For investigating the combined effect of strain rate and temperature on flow stress, the Zener-Holloman parameter $Z$ (temperature-compensated strain rate parameter) is used [31, 32] by treating hot deformation as a thermally activated process. The Zener-Holloman parameter is related to flow stress by following equations. It can be described similarly to strain rate

IOP Publishing Mater. Res. Express 10 (2023) 096513 P M Ahmedabadi

dependence on activation energy and temperature in creep studies.

$$\ln Z = \ln \dot{\varepsilon} + \frac{Q_d}{RT} = \ln j(\sigma) = \begin{cases} \ln A_1 + n' \ln \sigma \\ \ln A_2 + \beta\sigma \\ \ln A_3 + n \ln [\sinh(\alpha\sigma)] \end{cases} \quad (1)$$

Here, $Q_d$ is the activation energy of deformation and $R = 8.314$ J/mol · K is the universal gas constant. In equation (1), $A_1$, $A_2$, and $A_3$ are scaling factors, exponents $n'$, $n$, and $\beta$, $\alpha$ are material parameters with $\alpha \approxeq \beta/n'$. It is generally observed that the expression $j(\sigma) = A_1\sigma^{n'}$ is valid at low values flow stress, $j(\sigma) = A_2 \exp(\beta\sigma)$ is valid for higher values, and, $j(\sigma) = A_3[\sinh(\alpha\sigma)]^n$ is valid for all values of stresses. The activation energy, $Q_d$, obtained from the above three expressions is expected to be comparable. Typically, material parameters in equation (1) are obtained at peak flow stress [33–35] which is considered as independent of strain. For better prediction, temperature-dependent self-diffusion coefficient and Young's modulus are also incorporated sometimes in the hyperbolic representation of flow stress in equation (1) [36, 37].

All representations of flow stress are collectively denoted by the symbol $z$. In addition, strain rate is represented as $x = \ln \dot{\varepsilon}$ and temperature as $y = 1/T$. According to equation (1), apparent activation energy $Q_d$ is given by

$$Q_d = R\left(\frac{\partial z}{\partial y}\right)_x \left(\frac{\partial z}{\partial x}\right)_y^{-1} = -R\left(\frac{\partial x}{\partial y}\right)_z \quad (2)$$

Calculation of materials constants is based on assumptions that plots $z$ versus $x$ and $z$ versus $y$ are parallel straight lines so that the Arrhenius relationship can be used to obtain $Q_d$. In other words, activation energy $Q_d$ and other material constants that appear in equation (1) should be independent of strain rate or temperature. This also implies that fitted straight lines of $z$ versus $x$ and $z$ versus $y$ should be parallel so that the slopes are true constants. However, this is usually not the case, and material constants and activation energy $Q_d$ are generally reported as average values. It is also argued that since the role of microstructure is not considered, the fitting parameters are apparent materials constants [36].

It is observed that the variation of $z$ with $x$ and $y$ can be nonlinear, particularly at lower or higher values of $Z$. Intermediate values of $Z$ give a largely linear relationship with flow stress. One way to overcome this is to fit the entire temperature range using different segments so the individual segment can still be a straight line even if the entire temperature range shows nonlinear behavior. Each segment has a separate set of material constants, including activation energy. This approach was adopted in [38]. The second approach is the nonlinear fitting of flow stress with temperature and strain rate. This is done by assuming material parameters and activation energy $Q_d$ in equation (1) as functions of $\ln \dot{\varepsilon}$ and $1/T$, for example, see [39]. In this approach, the activation energy is a function of strain rate and temperature, unlike in the case of linear fitting.

The primary objective of this investigation is to apply the multivariate fitting of variations in flow stress such that the materials constants in these models are independent of $T$ and $\dot{\varepsilon}$ over the entire experimental range. This contrasts conventional constitutive models in which flow stress is modeled separately with $T$ and $\dot{\varepsilon}$. Two kinds of multivariate nonlinear fitting approaches are proposed, one in which activation energy is a function of temperature and strain rate and the other in which activation energy is independent of temperature and strain rate.

## 2. Conventional and modified constitutive models

It may be noted that the primary focus of this investigation is to model variations in flow stress; equation (1) is used in the following form.

$$\ln \sigma = -\frac{\ln A_1}{n'} + \frac{Q_d}{RTn'} + \frac{\ln \dot{\varepsilon}}{n'} \quad (3)$$

$$\sigma = -\frac{\ln A_2}{\beta} + \frac{Q_d}{RT\beta} + \frac{\ln \dot{\varepsilon}}{\beta} \quad (4)$$

$$\ln \sinh(\alpha\sigma) = -\frac{\ln A_3}{n} + \frac{Q_d}{RTn} + \frac{\ln \dot{\varepsilon}}{n} \quad (5)$$

Conventionally, $z$ is fitted with $x$ and $y$ separately, hence, linearly fitted curves of $z$ versus $y$ (for different $x$) and $z$ versus $x$ (for different $y$) can be expressed as

$$\mathbf{A}_c\text{:}\ \ z = a_0 + b_0 x \quad (6)$$

$$\mathbf{A}_t\text{:}\ \ z = a_1 + b_1 y \quad (7)$$

Since material parameters in equation (6) is obtained for a given $y$, the values of $a_0$ and $b_0$ are typically different for different values of $y$. Similarly, parameters $a_1$ and $b_1$ depend on $x$. The above linear models are collectively denoted **A**. For a better fitting, nonlinear fitting can be applied instead of the linear fitting given above

12

A Letters Journal Exploring the Frontiers of Physics

March 2023

EPL, **141** (2023) 58001
doi: 10.1209/0295-5075/acba41

www.epljournal.org

# Phase matching in quantum search algorithm

Saptarshi Roy Chowdhury[a], Sudarshan Baruah and Biswaranjan Dikshit

*Beam Technology Development Group, Bhabha Atomic Research Centre - Mumbai-400085, India*

received 11 November 2022; accepted in final form 8 February 2023
published online 22 February 2023

**Abstract** – We systematically generalize the Grover algorithm in a density matrix formalism by exploiting the underlying two-dimensional subspace of the problem. Using this, we derive analytic expressions for the success probability after arbitrary iterations of the generalized Grover operator with two generic phase angles $(\alpha, \beta)$. We show for the phase matching condition $\alpha = -\beta = 0.268\pi$ with *three* iterations, success probability $\geq 0.8$ can be achieved only with knowledge about the lower bound $\lambda = 0.14$, where $\lambda$ is the ratio of marked to total number of states in the database. This result will improve the quantum search algorithm when applied to databases with unknown number of marked states in the specified regime of $\lambda$, at the cost of decreased efficiency in the smaller $\lambda$ region.



**Introduction.** – The subject of quantum computation is believed to hold exceptional promise in the sense of solving some of the crucial problems with significantly better computational advantage than their classical counterpart. Quantum algorithms such as Deutsch-Jozsa algorithm [1], Shor's factorization algorithm [2], Grover's quantum search algorithm [3,4] are some of the notable examples in this regard. The Grover algorithm gives square root speed up over the best available classical algorithm when searching for marked items from an unstructured database.

After this seminal finding, several efforts have been made to extend and improve the quantum search algorithm. These include the proof that the algorithm is computationally optimal [5,6]. It was shown to be a larger class of quantum amplitude amplification problems by Brassard and Hoyer [7]. Long [8,9] generalized the algorithm for generic phase angles and gave exact phase expressions for 100% success. Biham *et al.* [10–13] found success probability expressions for an arbitrary pure and mixed initial states using recursion equation analysis for the amplitudes. For some of the further works on quantum search, see refs. [14–22]. Li and Li [23] reported for $\lambda \geq 1/3$, success probability $P(\lambda) \geq 25/27$ can be achieved with a single iteration where $\lambda$ is the ratio of the marked to total number of states in the database. Multi-phase matching condition was proposed [24,25] and numerical results were given to improve the success probability for a wide range of $(\lambda)$. The role of coherence on the success probability was studied [26,27] using measures of quantum coherence and quantum correlations [28] for arbitrary pure initial states using previous results [10,11]. Some of the experimental realizations of the Grover algorithm applied to known databases have also been reported, see refs. [29–41].

The Grover iteration can be thought of as a rotation in the two-dimensional Hilbert space spanned by marked and unmarked states [42]. Each rotation slowly transforms the initial state which is a uniform superposition towards the marked states. Unitarity of the Grover operator implies there will always be the so-called "overcooking" ("under cooking") of the prepared state if we iterate more than the required number as the eigenvalues are inherently periodic. This often poses difficulty when the exact number of marked items in the database is unknown. To get around this problem, the idea of fixed point quantum search was proposed by Grover [43] with a recursion relation for the successive operators to be applied in the algorithm. Fixed point quantum search works at the price of decreased efficiency [35] as the query complexity scales exponentially with the number of iterations. Chuang *et al.* [44] gave a fixed point search with an optimal number of user-controlled oracle queries using phase matching functions typically used as frequency filters in electronics. However, it has been pointed out [45] that the user might not have access to the oracle in each step of the quantum search process. Oracle query should be a fixed unitary made out of physical processes without any user-controlled parame-

[a]E-mail: satarshi96@gmail.com (corresponding author)

ter as seen in recent demonstrations [40,41,46]. For some of the recent works in this regard, see refs. [47,48].

In this paper we systematically generalize the Grover algorithm in a density matrix formalism, exploiting the underlying two-dimensional subspace of the $n$-qubit system. We find analytic expressions for success probability for arbitrary iteration as a function of the number of iteration $m$, two generic phase angles $(\alpha, \beta)$ and parameter $\xi$, introduced to capture the coherence present in the initial quantum register. Next we consider the phase matching condition $\alpha = -\beta$ with various phases and iterations. We show the success probability profile to be always greater than a fixed threshold (0.8 and 0.9), in the relevant range of $\lambda \leq 0.5$, can be achieved only with the knowledge about the lower bound on $\lambda$. In particular, we find $P(\lambda) \geq 0.8$ for *three* iterations and $\alpha = -\beta = 0.268\pi$ with the lower bound to be $\lambda = 0.14$. We tabulate values of phase angle $\alpha$ and corresponding lower bounds up to five iterations for which we consistently get $P(\lambda) \geq 0.8$ and $\geq 0.9$. This fixes the "overcooking" ("under cooking") problem up to the mentioned range of $\lambda$, when applied to a database with unknown $\lambda$, without using user-controlled oracle query. Finally, we quantify the performance of the algorithm against initial state preparation errors for the above phase matching condition.

**Preliminaries.** – Let us review the Grover algorithm and its generalizations hitherto known. Suppose we have an unstructured database of size $N = 2^n$ and want to search for $M$ marked items from the database. Classically, the query complexity of the problem scales as $O(N/2M)$ with the size of the database. Quantumly, as Grover showed in his remarkable paper [3,4], one can achieve quadratic speed up over the classical case. The Grover algorithm consists of initialization of the $n$-qubit state $|0\rangle^{\otimes n}$ to equal superposition state using $n$-qubit Hadamard gate as $|\psi\rangle = H^{\otimes n}|0\rangle^{\otimes n} = \frac{1}{\sqrt{N}} \sum_{x=1}^{2^n} |x\rangle$, then application of the oracle and diffusion operator (the product is also called Grover operator $G$) [3,4] iteratively $k_{opt} = (\pi/2\theta - 1/2)$ times with $\theta$ given by $\theta = 2 \arcsin \sqrt{\lambda}$, where $\lambda = M/N$. The effect of $G$ on $|\psi\rangle$ is essentially captured by the rotation matrix written in the basis $|R\rangle, |T\rangle$ as

$$G = \begin{pmatrix} \cos\theta & -\sin\theta \\ \sin\theta & \cos\theta \end{pmatrix},$$

with the bases $|R\rangle$ and $|T\rangle$ given by $|T\rangle = \frac{1}{\sqrt{M}} \sum_{x=1}^{M} |x\rangle$, $|R\rangle = \frac{1}{\sqrt{N-M}} \sum_{x=M+1}^{N} |x\rangle$, respectively. In terms of these bases, the initial state can be written as $|\psi\rangle = \sqrt{1-\lambda}|R\rangle + \sqrt{\lambda}|T\rangle$. Application of Grover operator has the effect of rotating $|\psi\rangle$ towards $|T\rangle$ through an angle $\theta$ in each iteration taking $k_{opt}$ iterations in total before measurement can be done in the computational basis completing the quantum search process. Exact knowledge of $\lambda$ is required for the algorithm to succeed as a slight mismatch of the number of iterations from $k_{opt}$ could lead to a significant decrease in performance due to the inherent periodicity of the rotation operator.

Generalization of the Grover operator $G(\alpha, \beta) = V(\beta)U(\alpha)$ has been made with two generic phases written in the basis of $|R\rangle, |T\rangle$ as [23]

$$V(\beta) = Ie^{i\beta} + (1 - e^{i\beta})|\psi\rangle\langle\psi|,$$
$$U(\alpha) = I - (1 - e^{i\alpha})|T\rangle\langle T,$$

where $U$, the generalization of oracle, selectively shifts the phases of the marked states by an angle $\alpha$ and $V$, generalized diffusion operator, shifts the phase by angle $\beta$ around the fixed state $|\psi\rangle$ each time. This reduces to the original Grover algorithm for the choice $\alpha = \beta = \pi$.

Li and Li gave their new phase matching condition as $\alpha = -\beta = \frac{\pi}{2}$. This gives the result that with single iteration, we get success probability $P(\lambda) \geq \frac{25}{27}$ for $1/3 \leq \lambda \leq 1$, which is useful when the number of marked states in the database is unknown. A geometric picture on this particular phase matching can be found here [23], where intermediate state vectors are projected in planes spanned by the vectors perpendicular to $|R\rangle$ and $|T\rangle$ due to the $\pi/2$ phase shift.

**Exact expressions for arbitrary iteration.** – We begin with the matrix representation of the operator $G(\alpha, \beta) = V(\beta)U(\alpha)$ in the $\{|R\rangle, |T\rangle\}$ basis,

$$\begin{pmatrix} (1 - e^{i\beta})(1 - \lambda) + e^{i\beta} & e^{i\alpha}(1 - e^{i\beta})\sqrt{\lambda(1-\lambda)} \\ (1 - e^{i\beta})\sqrt{\lambda(1-\lambda)} & e^{i\alpha}(1 - e^{i\beta})\lambda + e^{i(\alpha+\beta)} \end{pmatrix}.$$

Let the initial density matrix be

$$\rho_{initial} = (1 - \lambda)|R\rangle\langle R| + \lambda|T\rangle\langle T| + \xi\sqrt{\lambda(1-\lambda)}(|R\rangle\langle T| + |T\rangle\langle R|),$$

where $\xi$ is the parameter introduced to capture coherence present in the initial quantum state.

The density matrix after $m$ iterations is given by $\rho_m = G^m \rho_{initial} (G^\dagger)^m$. The success probability can be given as the $\langle T|\rho_m|T\rangle$ element of the final density matrix. We raise $G(\alpha, \beta)$ and $G^\dagger(\alpha, \beta)$ to the $m$-th power using the standard method of expanding the matrix in the basis of $I$ and the Pauli matrices [45]. After some simple algebra, we obtain the success probability as a function of $m$, $\xi$ and generic angles $\alpha$ and $\beta$ as

$$P(\lambda, \xi, \alpha, \beta, m) = \lambda + \sin^2(m\phi)[(1 - n_3^2)(1 - 2\lambda)] - 2\xi\sqrt{\lambda(1-\lambda)}\sin^2(m\phi)[n_1 n_3 + n_2 \cot(m\phi)], \quad (1)$$

with

$$\cos(\phi) = \cos\frac{(\alpha + \beta)}{2} + 2\lambda \sin(\beta/2)\sin(\alpha/2),$$
$$n_1 = -\frac{\sqrt{\lambda(1-\lambda)}}{\sin(\phi)} 2\cos(\alpha/2)\sin(\beta/2),$$
$$n_2 = \frac{\sqrt{\lambda(1-\lambda)}}{\sin(\phi)} 2\sin(\alpha/2)\sin(\beta/2),$$
$$n_3 = \frac{1}{\sin(\phi)}\left[-\sin\frac{(\alpha + \beta)}{2} + 2\lambda\sin(\beta/2)\cos(\alpha/2)\right].$$

13

Jinst

PUBLISHED BY IOP PUBLISHING FOR SISSA MEDIALAB

RECEIVED: *April 15, 2023*
ACCEPTED: *May 17, 2023*
PUBLISHED: *July 14, 2023*

# Single Stretch Wire and vibrating wire measurement system for characterization of multipole accelerator magnets

**Vikas Teotia*** **and Sanjay Malhotra**

*Electromagnetic Applications & Instrumentation Division, Bhabha Atomic Research Centre, Trombay, India*

*E-mail:* vteotia@gmail.com

ABSTRACT: A stretch wire magnetometer is a versatile instrument and can be treated as the primary standard of magnetic qualification of accelerator magnets. Bhabha Atomic Research Centre has developed a Stretch wire magnetic measurement system to cater to the requirements of magnetic measurements on accelerator magnets. This bench also includes a vibrating wire system. The scheme used in this instrument for measurements of magnetic flux ensures drift compensations after each scan. This feature along with post-signal processing gives an accuracy of homogeneity measurements comparable to that of a rotating coil magnetometer. Unlike conventional stretch wire systems, wire moves in the *r*-*z* plane (along r-axis) at different azimuthal angles. This provides the opportunity for drift compensation at each scan. This has immensely enhanced the measurement accuracy of non-homogeneity of integral fields to less than 3 units. The same is cross-verified with a rotating coil system. The comparison between rotating coil and stretch wire is presented. The Paper gives the step-wise procedure for the measurement of key performance indicators of an accelerator magnet. This paper brings out salient features of the system along with design and calibration results.

KEYWORDS: Acceleration cavities and superconducting magnets (high-temperature superconductor, radiation hardened magnets, normal-conducting, permanent magnet devices, wigglers and undulators); Beam-line instrumentation (beam position and profile monitors, beam-intensity monitors, bunch length monitors); Hardware and accelerator control systems

*Corresponding author.



https://doi.org/10.1088/1748-0221/18/07/P07029

2023 JINST 18 P07029

## Contents



2023 JINST 18 P07029

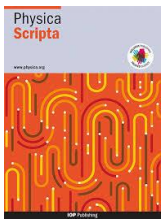

14

IOP Publishing Phys. Scr. 99 (2024) 015525 https://doi.org/10.1088/1402-4896/ad16c6

Physica Scripta

PAPER

# Synchronization of complexity enhanced chaos in semiconductor lasers

Bappaditya Pal[1], Sudarshan Baruah[1] and Biswaranjan Dikshit[1,2]

[1] Advanced Tunable Laser Applications Division, Bhabha Atomic Research Centre, Mumbai-400085, India
[2] Homi Bhabha National Institute, Department of Atomic Energy, Mumbai-400094, India

E-mail: bappa@barc.gov.in

OPEN ACCESS

RECEIVED
18 October 2023

REVISED
15 November 2023

ACCEPTED FOR PUBLICATION
18 December 2023

PUBLISHED
29 December 2023



**Keywords:** chaos, complexity enhancement, time delay information concealment, synchronization, permutation entropy, secure key distribution

## Abstract

In synchronized chaotic lasers based secure key distribution and other encrypted communications, presence of the time delay signature in chaos poses a threat to security. So the transmitter and receiver lasers should preferably be operated in complexity enhanced chaotic regime where the time delay signature is hidden. However, achieving good synchronization in experiments in such regime is challenging. We report experimental demonstration of achieving excellent synchronization between two semiconductor lasers even when both the lasers are operating in complexity enhanced chaotic regime with absolutely no time delay signature present in their output. This chaotic regime is ensured by evaluating the auto correlation function, permutation entropy and spectrum analysis of the time series. As a measure of synchronization, cross-correlation coefficient of 0.923 is achieved between the transmitter and receiver lasers. This results are of immense importance in chaos based secure key distribution and other encrypted communication schemes.

## 1. Introduction

Generation and synchronization of chaos [1] in semiconductor laser (SL) has exhibited tremendous application potential [2–4]. Among those, secure key distribution using correlated SLs is the most emblematic one [5–7]. In particular, the development of quantum computing technology along with sophisticated algorithms [8], poses a threat to the computational algorithmic based asymmetric-key schemes (like RSA) [9]. An alternative of this scheme is the one-time pad (OTP) based encryption which requires a secure key distribution between two parties (i.e. the sender and the recipient) prior to the actual communication [10–12]. Quantum key distribution (QKD), in which the security is attributed to the fundamental properties of the quantum mechanics, is ideal for this purpose [13]. However, implementation of QKD in the commercial communication system is still demanding [14, 15]. Synchronized chaotic SLs provide an excellent alternative method to distribute the secure key. Other potential applications include high speed long distance secure communication [16, 17]. Two key features in such applications of synchronized chaotic SLs are the complexity of the chaos and the synchronization between transmitter laser (TL) and target receiver laser (RL). Security of the information is ensured by the complexity of chaos being used for encryption. On the other hand, recovery of the encrypted signal in receiver end depends on synchronization between TL and RL. The complexity of chaotic time series can be characterised by normalized permutation entropy (PE), autocorrelation function (ACF) and spectral analysis. PE has gained popularity as a measure of complexity of real world time series [18, 19]. ACF provides a robust measure of time delay information (TDI) as well as the complexity of chaotic time series [20]. For less complex chaos there are repeated peaks in ACF at integral multiple of time delay. The TDI helps mapping the actual chaotic attractor to much lower dimensional attractor and hence reduce the complexity [21, 22]. So the presence of TDI is detrimental for security in all of the chaos based encryption techniques. Hence, the TL and RL should preferably be operated in a complexity enhanced regime where TDI is masked. In this regime the secondary peaks in ACF are disappeared [23]. Recent studies have been reported about different schemes to enhance the

IOP Publishing Phys. Scr. 99 (2024) 015525 B Pal et al

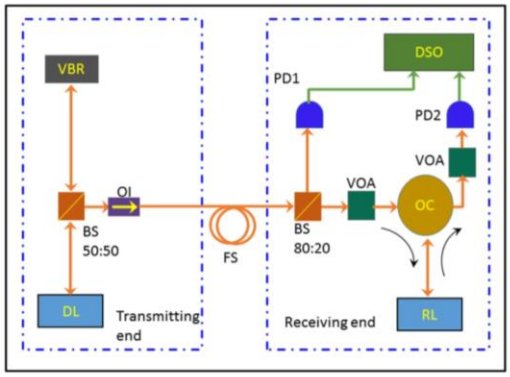


**Figure 1.** Schematic of the experimental setup with two semiconductor lasers under master slave configuration. TL: Transmitter Laser, FS: 10 km single mode fibre spool, RL: Receiver Laser, BS: Beam Splitter, OI: Optical Isolator, OC: Optical Circulator, PD: Photo diode, VBR: Variable back reflector, VOA: Variable optical attenuator, DSO: Digital Storage Oscilloscope.

complexity of the chaos generated in SLs and hiding the TDI [24–29]. However, when both TL and RL are operating in this strong chaotic regime, meeting the other criteria of chaos based encrypted communication, namely good synchronization between TL and RL is challenging [19, 30]. In this report we address this point. We have demonstrated experimentally that when chaos in the TL is generated by optical injection from another chaotic laser, then not only complexity enhanced chaos with absolutely no TDI could be generated, but also excellent synchronization between TL and RL could be achieved by properly controlling the operating parameters. We have also shown that the spectral analysis provides a qualitative measure about the complexity of the chaos. In particular, for relatively less complexity of the chaos, there are repetitive and uniformly spaced spectral lines in the Fourier spectrum. In contrast, for complexity enhanced chaos, those repetitive spectral lines get merged into the continuum of the Fourier spectrum. This report is organized in the following way. In section 2, we describe in details the experimental results of reduced synchronization with increase in complexity with two lasers, TL and RL in conventional master-slave (MS) configuration under unidirectional coupling. Master laser is basically the TL, and slave laser is RL. TL is subjected to self-optical feedback from a variable back reflector (VBR). The optical feedback induces a coupling between the phase and the amplitude of the electric filed. The laser then may exhibit instabilities including chaos [31]. We have shown that with the increase in the feedback strength, the complexity of chaotic output from TL is increased. This is verified from increasing PE, substantial reduction of secondary peaks in ACF, and spectral analysis. However, here TDI is not hidden completely. We have quantified the state of synchronization in terms of cross-correlation coefficient and then present our results that in MS configuration with increase in complexity, the cross correlation coefficient between TL and RL is decreased. This is consistent with the reported literature [19, 30] and it limits the recovery of the signal in the receiver end in all chaos based encrypted communication schemes. In section 3, we describe experimental results with three lasers in Driver-Transmitter-Receiver (DTR) configuration. Chaos in the TL is generated by optical injection from another chaotic laser which we call driver laser (DL). Chaotic output from the TL is then injected to RL. We report that in this scheme, TDI is totally absent in the chaotic output from both the TL and RL. Also, excellent synchronization, with cross correlation coefficient of 0.923 is achieved between these two lasers by suitable adjustment of optical injection from TL to RL.

## 2. Two laser schemes

### 2.1. Experiments

Figure 1 shows the schematic of our experimental setup with two c-band 1550 nm semiconductor lasers under MS configuration. The lasers have free running, room temperature threshold of ~12 mA. The experiments were carried out with injection current set at 40 mA and temperature at 25 °C in both the lasers. In these values the output power of both the laser is 4 mW. The output of the TL is divided into two equal part by a 50:50 beam splitter (BS). One arm of the BS is connected to a VBR for optical feedback. The VBR has an insertion loss ~2 dB. The output from the other arm of the 50:50 BS is sent to the receiver end through a 10 km single mode fibre spool. In the receiving end the output from the fibre spool is divided into two parts by an 80:20 BS. The output of the 20% arm is detected by a photodetector (PD), while the output from the 80% arm is injected to the RL via a

15

IOP Publishing Mater. Res. Express 10 (2023) 086514 https://doi.org/10.1088/2053-1591/acf278

Materials Research Express

PAPER

# Synthesis, microstructure and electrochemical properties of Ni-P-based alloy coatings for hydrogen evolution reaction in alkaline media

A P Gaikwad[1], Atindra Mohan Banerjee[1,2,*], M R Pai[1,2], Rajat Dheeman[1,4], Sanjay Kumar[3] and A K Tripathi[1,2]

[1] Chemistry Division, Bhabha Atomic Research Centre, Mumbai-400085, India
[2] Homi Bhabha National Institute, Anushaktinagar, Mumbai-400094, India
[3] Materials Science Division, Bhabha Atomic Research Centre, Mumbai-400085, India
[4] Project student, Institute for Chemical Technology, Mumbai.
* Author to whom any correspondence should be addressed.

**E-mail:** atinmb@barc.gov.in and atinmb@gmail.com

**Keywords:** Ni-P alloy, electrocatalyst, hydrogen evolution reaction, electrodeposition, coatings

Supplementary material for this article is available online

OPEN ACCESS

RECEIVED
21 April 2023

REVISED
14 August 2023

ACCEPTED FOR PUBLICATION
21 August 2023

PUBLISHED
5 September 2023



## Abstract

Alkaline water electrolysis driven by renewable energy is a promising technology for green hydrogen generation. The cathode half-cell reaction i.e., the hydrogen evolution reaction (HER) in alkaline water electrolysis suffers from slow kinetics. Ni-P-based alloys have shown to be an efficient and cost-effective electrocatalyst to accelerate the HER rate. In this study, three Ni-P alloy coatings are prepared via electrodeposition by varying the deposition currents viz. 10 mA cm-2 direct, 10 mAcm-2 and 100 mAcm-2 pulsed currents. The XRD patterns of all the Ni-P coatings exhibited the formation of crystalline deposits and confirmed the alloying of P in Ni. The SEM images suggested that the microstructures of the Ni-P alloy deposits are highly dependent on the magnitude and waveform of the applied current employed during preparation of the alloy coatings. The composition of the alloy surface is Ni-rich in all three cases but exhibited local variations as evaluated by EDX. The surface distributions of Ni and P in the pulsed deposited samples are more uniform and homogeneous. The cyclic voltammetry patterns of the Ni-P coatings in KOH media exhibit characteristic peaks due to Ni/Ni3+ redox phenomenon. The Ni2+/Ni3+ oxidation peak area is lowest for the direct deposited sample and highest for the pulsed deposited one (100 mAcm-2). The Ni-P alloy electrocatalyst deposited under pulsed mode at 100 mAcm-2 exhibits a current density of −10 mAcm-2 at 0.09 V overpotential and is most active among all samples. The remarkable electrocatalytic activity of this sample is attributed to its smaller crystallite size, better morphological characteristics and lesser resistances to charge transfer and porosity.

## 1. Introduction

Hydrogen is a promising alternative green energy carrier with a very high calorific value of ~ 142 KJ/mole and if it can be produced using renewable energy by water splitting a completely green energy utilization option emerges [1–3]. Water splitting can be accomplished by a variety of ways such as electrolytic [2–5], thermochemical [6, 7], photoelectrochemical [8, 9], photocatalytic [10, 11] etc. Among them, electrochemical water splitting or electrolysis is at present the most feasible, commercialized, and matured technology [12]. Green hydrogen generation can be achieved upon coupling water electrolysis with a PV or wind turbine system [4, 5]. Alkaline water electrolysis is a hydrogen generating process at an advanced stage of development with established commercial plants. However, the electrochemical reactions at the electrodes for alkaline water electrolysis, viz. hydrogen evolution reaction (HER) and oxygen evolution reaction (OER), suffers from

overpotentials due to kinetic, ohmic, and mass transfer limitations [12, 13]. To reduce the kinetic barrier, the use of electrocatalysts is desirable but noble metal based electrocatalysts like Pt, Rh etc are most effective. Although both the activity and stability of these noble metal-based electrocatalysts are high, the cost and availability are significant concerns for their industrial application [3, 4, 13, 14]. As a cheaper replacement for costly noble metal-based electrocatalysts, Ni-based materials have found promising applications in alkaline water electrolysis [14, 15]. But Ni as an electrode suffers from passivation and corrosion during the electrolysis operation [14, 16]. The passivity of Ni in alkaline solution is widely studied as it finds applications in corrosive and mechanically demanding environments viz. steam generators etc. The passive film on Ni is formed spontaneously, is of the order of few nm, and is generally bi-layered with inner one predicted to be NiO with point defects [17–19]. Studies to investigate the probable causes for the deactivation of Ni under reaction conditions, both for HER and OER have been conducted [14, 16, 20–23]. Alloying Ni with other elements were attempted to address these stability aspects, and it was found that alloying in many cases have led to a change in surface morphology and yielded materials with higher electrocatalytic activity and stability [14]. A wide variety of Ni-based alloys was investigated and some promising results were obtained in many cases, viz. Ni-Mo [14, 23–26], Ni-Fe [27, 28], Ni-Co [29, 30], Ni-W [31, 32] and Ni-P [14, 33–48].

Ni-P-based alloys are extensively investigated for their superior mechanical, tribological, magnetic, and electrochemical properties with a wide range of applications [35]. Ni-P alloys show improved performance in terms of electroactivity and stability for alkaline water electrolysis. In most of these studies, Ni-P alloy coatings have been prepared by electrochemical deposition method as it has several advantages like it is simple, scalable, possibility to tailor the composition and crystallinity of the deposited alloy [14, 49]. Ivo Paseka reported the electrocatalytic activity of amorphous Ni-P alloys prepared by electrodeposition under galvanostatic conditions [33]. They concluded that the amorphous nature of the deposits enabled significant absorption of hydrogen, which resulted in high electrocatalytic activity. Later, Paseka correlated the increased hydrogen absorption to the stress developed in these amorphous alloys [38]. Hu and Bai studied the electrocatalytic activity of Ni-P deposits as a function of P content and inferred that 7 wt% P is optimum to achieve the highest activity [39]. Wei *et al* found 10 wt% P to be the most favorable Ni-P composition for HER [40]. Lu *et al* studied Ni-P for HER in an acidic medium and they concluded that as the P content increased, the catalytic activity decreased for HER, which they attributed to the decrease in grain boundaries with an increase in P content [43]. However, Kucernak *et al* proposed that the HER electroactivity for Ni-P increased with an increase in P content and that a very high P content in the alloy is beneficial [44]. From the above studies, it is established that Ni-P coatings prepared by electrodeposition are a promising electrocatalyst for HER. However, the morphology and P-content are crucial aspects that determine the performance of the deposits.

An important consideration while preparing Ni-P coatings by electrodeposition is that the properties of the deposits vary with electrodeposition operational parameters viz. composition i.e. the P-content, crystallinity, phase, morphology. Again, these properties of the NiP coatings will have a direct impact on the electrochemical properties of the coatings. The properties of the deposits defined by its composition, uniformity, porosity, and surface roughness play a crucial role. Thus, the electrodeposition operational parameters can modify the electrochemical performance of the deposits for HER. Several parameters can be varied during electrodeposition viz. current, current waveform, bath composition, additives, temperature of bath etc [35]. In this study, we report the preparation of Ni-P coatings under three different applied current conditions and investigate its effect on the nature and properties of the deposits. The current waveforms, i.e. pulsed or direct current during electrodeposition are modified and its consequent effect on structure, properties and electrochemical properties are investigated. Ni-P alloy coatings on copper substrate are prepared under direct and pulsed current waveforms at 10 $mAcm^{-2}$ and also at 100 $mAcm^{-2}$ current pulses. The Ni-P alloys are characterized for structure and morphology by powder-XRD and SEM-EDX techniques. The electrochemical properties of the Ni-P deposits are analyzed by cyclic voltammetry (CV), linear sweep voltammetry (LSV) and electrochemical impedances spectroscopy (EIS) techniques. Finally, the performances of the deposits for HER are evaluated by LSV and a morphology-electrochemical property co-relationship for the Ni-P alloy coatings is established.

## 2. Experimental

### 2.1. Materials

Highly conductive copper foils (99.9% pure) having a thickness 0.2 mm is employed as the substrate for electrodeposition in this study. $NiCl_2.6H_2O$ and $NaH_2PO_2.6H_2O$ are used as the precursors for nickel and phosphorous, respectively, and $NH_4Cl$ is used as an additive in the bath during electrodeposition. All the electrolyte solutions are prepared with analytical grade chemicals and nanopure distilled water. Before electrodeposition, the copper substrate is pretreated or cleaned to obtain a luminous finish. This pretreatment is performed by first polishing the surface with emery paper, washing with water, acetone, and then drying,

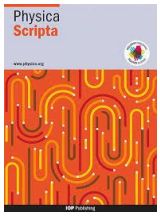

16

IOP Publishing Phys. Scr. 98 (2023) 075605 https://doi.org/10.1088/1402-4896/acdcc2

Physica Scripta

PAPER

# Tailoring of microwave power density in an ECR ion source using an optimized ridge coupler

OPEN ACCESS

RECEIVED
21 March 2023

REVISED
9 May 2023

ACCEPTED FOR PUBLICATION
8 June 2023

PUBLISHED
20 June 2023



**Monika Phogat and Jose V Mathew**

Ion Accelerator Development Division, Bhabha Atomic Research Centre, Mumbai - 400085, India

**E-mail:** josevm@barc.gov.in

**Keywords:** ECR ion source, bead pull measurements, plasma diagnostics, wave cut-off probe, multicusp ECR plasmas, ridge coupler

## Abstract

One of the interesting areas in the Electron Cyclotron Resonance Ion Source (ECR-IS) design which requires further exploration is the microwave power launching scheme and the power coupling optimization with the plasma chamber. The electron heating efficiency and thereby the plasma density highly depends on the electric field distribution inside the plasma chamber; therefore, it is important to optimize the coupling of microwave power to the plasma chamber, to maximize the electric fields in the plasma chamber for a given microwave power. For this, a single-step quarter wavelength ridge coupler design study has been carried out using CST MW Studio Suite along with the plasma chamber and ridge wave guide designs. The experimental measurements of electric and magnetic field profiles in the plasma chamber assembly with different coupling configurations have been done using an innovative bead pull technique and a magnetic field probe. The experimental results match well with the simulation results and the comparative studies of different coupling configurations reveal that the single step ridge coupler based scheme improves the electric field inside the plasma chamber to at least five times than the conventional ridge waveguide. To further improve the E-field amplitude in the plasma chamber by another 40%, a novel tuning scheme for the coupler has been introduced. Preliminary plasma studies have been carried out with the optimized coupler on a multicusp ECR plasma source and the plasma density measurements performed using a microwave cut-off probe. The plasma measurements show that even at low input microwave powers (~300 W) the plasma density is comparable with standard ECR-IS. The present study thus, sheds light on the coupling configuration of microwave to plasma chamber with experimental measurements of cavity mode and fields in the cavity which will be useful for high intensity accelerator applications in understanding the plasma evolution, beam parameters and its dependence on different operating parameters.

## 1. Introduction

Microwave based Electron Cyclotron Resonance Ion Source (ECR-IS) is widely used in high energy, high intensity accelerators for applications involving radioisotope production, spallation neutron sources, accelerator driven systems, high energy physics etc, since it can produce high intensity and high charge state ion beams with low beam emittance [1–6]. A high intensity ECR proton ion source has been developed for the Low Energy High Intensity Proton Accelerator (LEHIPA) at Bhabha Atomic Research Centre (BARC), India [4–6]. LEHIPA consists of H+ ion source at 50 keV which is accelerated to 3 MeV by Radio Frequency Quadrupole (RFQ) and thereafter to 20 MeV by an Alvarez type DTL consisting of 4 DTL tanks of 3 m each [7–9]. Currently LEHIPA has been commissioned to 11 MeV by acceleration through the RFQ and two DTL tanks [7, 8]. The LEHIPA ECR-IS has a two solenoid magnetic mirror field configuration with a conventional four-step ridge waveguide for microwave (MW) power coupling [4, 5].

One of the interesting areas of research in the ECR-IS is the MW power launching scheme and the power coupling optimization with the plasma chamber [3, 10–12]. The electron heating efficiency and thereby plasma density highly depends on the electric field distribution inside the plasma chamber; therefore, it is important to

optimize the coupling of MW power to the plasma chamber, to maximize the electric fields in the plasma chamber for a given MW power [10, 11]. This is more important for multicusp based ECR-ISs where the ECR heating efficiency is comparably weaker than the solenoid based ECR-IS [13–16]. Conventionally in ECR-IS systems, MW power is coupled to the plasma chamber using a ridge waveguide which can enhance the fields near to twice that of plain waveguide coupling [11, 12]. There have been efforts to design quarter wavelength coupler for ECR-IS to further improve the power density in the plasma chamber [3]. But, no measurements and analysis of the fields inside the plasma chamber with different coupling schemes have been reported to the best of our knowledge. As part of ongoing research on ECR-IS development at BARC we have developed a test setup for MW power optimization studies of the plasma source. For this, an optimized one-step $\lambda/4$ ridge coupler design study has been carried out using CST MW Studio Suite along with the designs of plasma chamber, and ridge wave guide [17]. The simulations show that, with the optimized coupler configuration, the maximum electric field in the plasma chamber has improved considerably to at least five times than with the conventional ridge waveguide coupling scheme. A novel tuning scheme for the ridge coupler has also been studied, which can further improve the E-field in the plasma chamber by another 40%. This tuning scheme is based on a movable tuner in the magnetic field region of the ridge coupler. Based on the simulations, the various components have been fabricated and assembled and electric and magnetic field profile measurements in the plasma chamber assembly with coupler for different coupling schemes have been carried out. Instead of using slotted line-based probes for field measurements in the plasma chamber, an innovative axial bead pull technique has been devised for E field measurements [18–21]. A magnetic loop probe has been developed for the magnetic field measurements. Preliminary plasma studies were also carried out using this optimized coupler, which was coupled with a multicusp ECR plasma source. The plasma density measurements were carried out using a microwave cut-off probe which measures the electron plasma density using transmission spectrum measurements [22, 23]. The design simulations; development of various plasma source components and probes for RF characterization and plasma diagnostics; experimental results of characterization of the field profiles inside the plasma chamber with different coupling schemes, and plasma measurements are presented in this paper.

This article is organized as follows. Section 2 describes the choice of the plasma chamber resonator cavity geometry and the design of single step ridge coupler using CST Microwave studio. The effect of various coupler parameters on electric field distribution of plasma chamber will be discussed here, along with the tuning scheme for E-field enhancement. In section 3 details of the experimental setup and the probes including the magnetic field probe and the bead pull technique which are used for experimental verification of field distribution profiles inside the plasma chamber and coupler are given. Also the experimental setup for the plasma measurements and details of the microwave cut off probe for plasma electron density measurements are also described in this section. The experimental results and analysis are given in section 4 which includes experimental identification of ion source cavity mode, E-field profiles obtained with bead pull technique, comparison of experimental and simulation-based study of different coupling configurations and preliminary plasma studies. Finally, a summary of the main results and conclusions are drawn in section 5.

## 2. Simulation studies

In this section, the design simulation studies of the plasma chamber, the 4-step ridge waveguide and quarter wavelength ridge coupler are discussed. These components are part of the experimental test bench for field measurements and plasma studies whose schematic is shown in figure 1. The waveguide adapter, 3-stub tuner, and transition waveguide shown in figure 1 are standard 2.45 GHz microwave transmission line components. The plasma chamber is a cylindrical resonator cavity, whereas the 4-step ridge waveguide and the quarter wavelength ridge coupler are designed in WR 284 rectangular wave guide configuration. The design details of each component are discussed in detail below.

### 2.1. Resonator cavity

Since the microwave power is coupled to the plasma chamber using $TE_{10}$ rectangular waveguide mode, TE mode has been chosen to be excited in the cylindrical plasma chamber, with the fundamental resonator cavity mode, $TE_{111}$ mode [21, 24, 25]. The resonant frequency for a TE mode is given by the relation [25],

$$f_{mnp}^{TE} = \frac{c}{2\pi\sqrt{\epsilon_r \mu_r}} \sqrt{\left(\frac{x'_{mn}}{r}\right)^2 + \left(\frac{p\pi}{l}\right)^2}, \quad (1)$$

where, $r$ and $l$ are the resonator cavity radius and length respectively, $c$ is the speed of light, $\epsilon_r$ and $\mu_r$ are, the relative electrical permittivity and magnetic permeability of the medium filling

17

A Letters Journal Exploring the Frontiers of Physics

August 2023

EPL, **143** (2023) 46003
doi: 10.1209/0295-5075/acedcb

www.epljournal.org

# Temperature-driven structural phase transitions in $0.05(Na_{0.50}Bi_{0.50})TiO_3$-$0.95NaNbO_3$ solid solution via amplitude mode analysis

V. B. Jayakrishnan, S. K. Mishra[a] and P. U. Sastry[b]

*Solid State Physics Division, Bhabha Atomic Research Centre - Mumbai 400085, India and Homi Bhabha National Institute - Anushaktinagar, Mumbai 400094, India*

received 21 April 2023; accepted in final form 7 August 2023
published online 18 August 2023

**Abstract** – Structural phase transitions in the $ABO_3$-type lead-free eco-friendly piezoelectric $0.05(Na_{0.50}Bi_{0.50})TiO_3$-$0.95NaNbO_3$ (05NBT) have been studied as a function of temperature using dielectric and X-ray diffraction techniques. Below 300 K, we observed dispersion in dielectric permittivity with the frequency, which confirmed relaxor behaviour in 05NBT. Using detailed analysis of temperature-dependent powder X-ray diffraction data of 05NBT, four phase transitions were identified across 600 K, 773 K, 823 K and 923 K. We found that on doping 5% NBT in pure sodium niobate, the low-temperature rhombohedral ferroelectric (N) phase and the high-temperature (S) phase of the sodium niobate get suppressed. To get a better insight about the temperature-driven structural phase transitions, various antiferrodistortive and additional distortive mode as well as the mode amplitude relative to high-symmetry cubic phase were computed and results are discussed.



**Introduction.** – Sodium niobate ($NaNbO_3$) has lately attracted tremendous attention owing to a distinctiveness of extraordinary structural phase transitions and its derivates are notable for eco-friendly piezo-ceramics for technological applications [1–11]. Structural phase transitions in this material involve tilt and/or rotation of the oxygen octahedra and cationic displacements [11–16], a classical example for the antiferrodistortive-type phase transitions [11,14,16–20]. The antiferrodistortive phase transitions result in multiplication of the unit cell due to anti-phase or in-phase octahedra rotations as a consequence of which the formula units in daughter phases are different from parent phase. These transitions can be identified on the basis of appearance and/or disappearance of the superlattice reflections and splitting of the main perovskite peaks in the powder diffraction patterns [21].

Material properties, such as phase transition temperature, crystal structure, dielectric and piezoelectric properties, can be effectively tuned by strain engineering. Furthermore, an external strain can even induce ferroelectricity in paraelectric/antiferroelectric materials. For example, ferroelectric phase in pure sodium niobate can be stabilized by application of external strain caused by chemical substitution either at the A or B sites of the $ABO_3$ perovskite. Several studies have been carried out to study the effect of external strain on the properties of NaNbO3. It is found that the strain induced by the homovalent ion ($Li_xNa_{1-x}NbO_3$, $K_xNa_{1-x}NbO_3$) and hetrovalent ($Na_{0.5}Bi_{0.5}$)$TiO_3$ ($x$NBT) [8,9,20–26], $BaTiO_3$ [17,18,27–29] $CaTiO_3$ [30,31], $SrTiO_3$ [7], $BiFeO_3$ [32,33], $PbTiO_3$ [34], etc., showed improvement in the ferroelectric and piezoelectric properties alongwith stabilization of various crystal structure.

Recently, we have reported the sequence of structural phase transitions in the $x$NBT system for the entire range of composition using combined powder X-ray and neutron diffraction techniques [35]. We found that in the composition range $0.0 \leq x < 0.15$, the orthorhombic antiferroelectric phase (space group $Pbma$) coexists with ferroelectric (space group $Pmc2_1$) phase and an orthorhombic symmetry with space group $Pbnm$ (cell

[a]E-mail: skmsspd@barc.gov.in (corresponding author)
[b]E-mail: psastry@barc.gov.in

dimensions $\sqrt{2}a_p \times \sqrt{2}b_p \times 6c_p$) gets stabilized for the composition range $0.15 \leq x < 0.20$. The tetragonal ($P4bm$) phase coexists with orthorhombic ($Pbnm$) phase for $0.20 < x < 0.60$, whereas in the region $0.60 \leq x \leq 0.80$, $P4bm$ coexists with the ferroelectric rhombohedral ($R3c$) phase. Finally, for the composition $x > 0.80$ it completely transforms to the rhombohedral ($R3c$) phase. The presence of phase coexistence in various composition ranges indicates the first-order nature of these phase transitions.

The end members of the $x$NBT system are well-known antiferroelectric (pure sodium niobate, $NaNbO_3$) and ferroelectric (sodium bismuth titanate, $Na_{0.5}Bi_{0.5}TiO_3$) at ambient conditions and would also be a prototype system to investigate the effect of competing antiferroelectric and ferroelectric interactions as well as relaxor behaviour in $x$NBT. We have selected the 05NBT composition for this study as it is near to pure sodium niobate, which undergoes a complex sequence of phase transitions with temperature. In a way, this system will also be a model to investigate the role of the A and B site doping on the phase stability of pure sodium niobate. In view of this, we have carried out the measurements of temperature dependence dielectric permittivity and investigated the phase stability in detail using a conjunction of dielectric and powder X-ray diffraction techniques. The presence of dispersion in dielectric permittivity with the frequency confirmed relaxor behaviour in 05NBT below room temperature. Detailed Rietveld analyses of temperature-dependent powder X-ray diffraction data of 05NBT were performed and a total of five polymorphs are identified across the temperature range ($13\,\mathrm{K} < T < 1273\,\mathrm{K}$). This result further reveals that on doping of 5% NBT in pure sodium niobate, the rhombohedral (N) phase and the orthorhombic (S) phase of pure sodium niobate [14] get suppressed. We have also investigated the main distortion responsible for the stabilization of different distorted structures in different temperature ranges with respect to the high temperature, high symmetry cubic phase using the amplitude distortion mode formalism [36,37]. It is found that the primary distortion modes for the stabilization of tetragonal phase and three orthorhombic phases belong to the $M$ $(1/2, 1/2, 0)$, $R$ $(1/2, 1/2, 1/2)$, and the DT $(q = 1/2, 1/2, q)$ with $q = 1/6$ and $1/4$ irreps associated with coupled stretching, twisting, and rotation distortions of $NbO_3$ octahedra.

**Experimental.** – The sample 0.05($Na_{0.5}Bi_{0.5}$)$TiO_3$-0.95$NaNbO_3$ sample was prepared using the solid-state reaction method and details are given elsewhere [23,35]. The X-ray diffraction studies were carried out using a rotating-anode–based powder diffractometer using Cu$K_\alpha$ radiation with a step interval of 0.02° in the $2\theta$ range of 20°–120°. To carry out temperature-dependent powder X-ray diffraction data, a sample environment facility (*i.e.*, low temperature (CCR) and for high-temperature furnace) attached to the diffractometer was utilized. All the refinements have been done using the FULLPROF program [38] and full angular range of data although only a limited range of X-ray diffraction patterns are shown in the figures for clarity. The dielectric properties were measured using a frequency-response analyser (Novocontrol TB-Analyser). A closed-cycle refrigerator with a He-gas exchange was used for cooling the sample down to 5 K. All the temperature-dependent diffraction and dielectric data were collected in the heating cycle.

**Results and discussion.** –

*i) Temperature dependence of dielectric studies.* Figure 1 shows the temperature dependence of relative real and imaginary parts of dielectric permittivity ($\epsilon'$ and $\epsilon''$) at various frequencies. The real part of dielectric permittivity ($\epsilon'$) increases with increasing temperature and shows a change in the slope around 100 K. A strong frequency dependence of the peaks in both real part of dielectric constant and dielectric loss as a function of temperature has been observed, which is characteristic of relaxor behaviour. The relaxor behaviour can be induced by many reasons, such as the merging of micropolar regions into nanopolar regions, the local compositional fluctuations and the existence of the dipolar glass state. In the 05NBT ceramics, $Na^+$ and $Bi^{3+}$ ions co-occupy the A-site and $Ti^{4+}$ and $Nb^{5+}$ ions co-occupy the B-site, of the $ABO_3$ perovskite structure. Therefore, the cations disorder in the perovskite unit cell may be reason for the appearance of the relaxor state in 05NBT. It is clear from this figure that the dielectric constant decreases with increase of frequency. The observed broad dielectric anomalies are a result of various competing interactions and are attributed to structural phase transitions. The activation energy associated with relaxation processes are determined by fitting (see fig. 1(b)) using the Arrhenius equation $\tau = \tau_0 \exp(\frac{-E_a}{k_B T})$, $\tau = \frac{1}{2\pi f_p}$, where $\tau_0$ is the prefactor, $E_a$ is the activation energy for relaxation process and $k_B$ is Boltzman constant. The activation energy $E_a$ is found to be 0.13 eV.

It is noteworthy that the dielectric constant of pure sodium niobate also shows similar type of behaviour with temperature exhibiting a change in the slope below 75 K, which is accompanied by a structural phase transition from antiferroelectric orthorhombic ($Pbma$) to ferroelectric rhombohedral ($R3c$) phase [11,39]. Hence, to explore the possibility of a structural phase transition in 05NBT with temperature, we have performed powder X-ray diffraction study in detailed and results are discussed below.

*ii) X-ray diffraction study.* Figure 2 shows the evolution of powder X-ray diffraction pattern of 05NBT in the temperature range of 12–1273 K. The powder diffraction pattern measured at lowest temperature 12 K can be indexed using two types of reflections. The first type of reflections belonging to the cubic phase of the perovskite structure appears around $2\theta \approx 22°$, 32°, 39° and 45°, which are known as main perovskite reflections and can

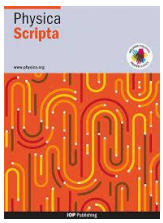

18

IOP Publishing Phys. Scr. 98 (2023) 115302 https://doi.org/10.1088/1402-4896/acfa3e

Physica Scripta

PAPER

OPEN ACCESS

RECEIVED
8 June 2023

REVISED
4 September 2023

ACCEPTED FOR PUBLICATION
15 September 2023

PUBLISHED
29 September 2023



# Tungsten-based polymer composite, a new lead-free material for efficient shielding of coupled neutron-gamma radiation fields: A FLUKA simulation study

**Avijit Das**[1,2,*], **Aditi Ray**[2,3] **and Tej Singh**[1,2]

[1] Research Reactor Services Division, Bhabha Atomic Research Centre, Mumbai 400085, India
[2] Homi Bhabha National Institute, Anushaktinagar, Mumbai 400094, India
[3] Theoretical Physics Section, Bhabha Atomic Research Centre, Mumbai 400085, India
[*] Author to whom any correspondence should be addressed.

**E-mail:** avijit@barc.gov.in

**Keywords:** FLUKA, W-PMMA composite shield, dose equivalent, secondary gamma, double-layer shield (DLS), specific dose

## Abstract

Metal-based polymer composites, a new category of advanced materials, are advantageous for effective protection of radiation field. Recent report of fabrication of tungsten (W)-Poly methyl methacrylate (PMMA) composite microcellular foams with enhanced mechanical strength properties opens up the possibility of its use in radiation attenuation. Objective of this theoretical study is to assess the efficacy of W-based polymer composite, a new lead-free shielding material for attenuating coupled neutron-gamma radiations. Current paper utilizes open-source Monte Carlo code FLUKA to evaluate shielding efficiency of PMMA composites reinforced with varying concentration W particles. Study shows that, adding even 20 vol% of W particles can significantly improve radiation shielding ability of PMMA. Performance of analogous composition Pb-based polymer composite is also examined to demonstrate its inadequacy in radiation protection compared to W-based composite. Study reveals an interesting fact that for any shield dimension, total radiation dose follows an initial descending trend with increase in heavy metal (W/Pb) proportion up to certain optimum value where dose becomes minimum, beyond that dose increases. Optimum heavy metal concentrations are found to be 70 vol% and 30 vol% for W and Pb respectively, with minimum dose for Pb shield being two orders of higher magnitude. Study is further extended to investigate shielding efficiency of conventional double-layer laminates employing W and PMMA in both high-Z/low-Z and low-Z/high-Z configurations as well as optimum concentration of W-PMMA composite and PMMA. It is shown that among all the potential designs, newly introduced composite-based double-layer shield performs best in terms of volumetric dose while single-layer optimized composite shield offers least specific dose.

## 1. Introduction

Dual radiation fields comprising of neutrons (n) and gamma rays ($\gamma$) are very common in various nuclear installations, such as, fission nuclear reactors, transportation and storage of nuclear materials, medical instruments (radiation therapy or diagnostics), etc. Physics design of mixed radiation shield is of great significance for these above mentioned utilities as well as for advanced special-purpose nuclear reactors, like, nuclear marine propulsion systems, space reactors, small modular reactors (SMRs) and upcoming fusion reactors. Primary objective of shield design is to *efficiently* attenuate *n* and $\gamma$ radiations so that the effective dose out of the shield remains within a prescribed limit. With this purpose, shields need to be constructed by appropriate combination of materials that are most suitable for attenuating individual radiation components i.e., n, $\gamma$ etc. In addition to excellent shielding performance, these materials should be lightweight and low-volume in support of increasing demand for miniaturization and should have good mechanical strength, durability leading to long service life, minimum radiation damage effect, low toxicity and finally cost-effective.

Traditionally lead (Pb), an element with high mass attenuation coefficient, was used for protecting from x-rays and $\gamma$ radiations in various applications. Recently, long-term health risk to medical personnel due to exposure of hazardous element Pb has been of a great concern [1]. Development of the new *lead-free*, lightweight, safe, robust and reliable radiation shielding materials for both industrial and space applications has made tremendous impetus [2, 3].

While constructing shield for dual radiation, it is to be noted that mid to high-Z elements like, Fe, Bi, Pb, W, etc are relatively good absorber of $\gamma$ rays but less effective against elastic scattering of neutrons. Whereas, materials like concrete, polyethylene, and others containing low-Z elements like H, Be, B, C are effective for attenuating neutrons through elastic scattering and/or absorption but not adequate for attenuating $\gamma$ energy. Major shortcoming of these materials is that they cannot shield the secondary $\gamma$ produced in the process of neutron interaction with shield material [4]. Homogeneous mixtures (composites) or multi-layer laminates (stratified) of light and heavy nuclei are preferable for shielding both n and $\gamma$ radiations [5, 6].

Polymer, is advantageous due to its low density, chemical stability and good neutron slowing performance. Due to good process ability and flexibility, Polymers are ideal for advanced manufacturing technologies. So, polymeric composites are promising substitutes for traditional shielding materials and have attracted recent attention. Only disadvantage is their inferior thermo-mechanical properties that further degrade on exposure to ionizing radiations for extended period of time [7]. However, blending polymers with inorganic fillers, mainly, metal-powders with good gamma shielding characteristics, have shown to improve the radiation resistance and mechanical properties. Demand for polymeric composites in radiation shielding application is rapidly increasing [8–10].

Polymers that are commonly used as matrix for fabrication of *metal-reinforced composite* include: polyethylene, polymethyl siliconate, PMMA, carbon fibre, polystyrene, neoprene, resin, nylon, polyvinyl chloride (PVC), teflon, epoxy, rubber, and many others. Gamma shielding characteristics of a plethora of different polymers are reported [11]. A comprehensive review of different inorganic compounds and polymers used for this purpose can be found in [12]. It is worth mentioning here that, radiation attenuation properties of polymeric composites are greatly enhanced by use of nanomaterials in place of bulk fillers, due to increase in surface to volume ratio [13].

Composite shields made out of thermoplastics have shown great potential for radiation shielding and possess the added advantage of flexibility to combine with variety of different fillers. PMMA ($C_5H_8O_2$) is a transparent thermoplastic with good tensile strength. Preparation of W-PMMA composite microcellular foam, with different W concentration, using melt-mixing and supercritical carbon dioxide foaming methods has been reported [14] with remarkably increased mechanical strength than those of pure PMMA. A recent work evaluated the gamma attenuation performance of $Bi_2O_3$ metal particles dispersed in PMMA matrix [15]. Present authors have evaluated gamma build-up factor of double-layer shield (DLS) involving iron and PMMA [16]. It was also shown that PMMA performs better than water or low-density polyethylene (LDPE) [17].

Promising metal powders considered for embedding in polymer matrix includes tungsten (W) [18–21], tantalum (Ta) [22], boron (B) [23], zirconium (Zr) [24], copper (Cu) [25], bismuth (Bi) [19], gadolinium (Gd) [26] and samarium (Sm) [27]. Various alloys involving Pb, W, Cu, Fe, Ni, Re and $B_4C$ have also been proposed as effective radiation shielding materials [28–32].

Among different high-Z elements, Pb and W are obvious choice for gamma shielding. A recent study reported comparable values of gamma shielding parameters, namely, linear and mass attenuation coefficients for Pb, W and tungsten carbide (WC). Study revealed that although mass attenuation coefficient of W is slightly lower than Pb [33], but high density of W makes it a potential alternative to Pb. Moreover, fast neutron removal cross-section of W is much higher than Pb. Tungsten containing polymer composites are attracting special interest due to their low toxicity, malleability and ability to effectively attenuate both neutron and gamma radiations. Effect of size and proportion of W particles on shielding properties of LDPE has been investigated [34]. In addition to metallic W, its oxides, carbides and bromides are also blended with polymers for shielding ionizing radiations [12]. Epoxy-based composite materials with Ta, WC and W metal particles have been explored for the application as dual radiation shields [22, 35].

So far, shielding properties of various metal-reinforced polymer composites have been studied extensively for mono-energetic neutron and $\gamma$ sources, but the same for broader spectrum of energy interval, so called *multi-group energy*, as produced in a nuclear reactor, has not been explored to that extent. Designing shield for coupled *n*-$\gamma$ sources, involving combination of high-Z and low-Z materials in composite or laminar form, is a complex problem as, it requires optimization of metal-particle content (composite) or layer thicknesses (laminar).

The aim of the current paper is to introduce a lead-free composite shield comprising of W and PMMA [14] and investigate its shielding properties in respect to *n*-$\gamma$ mixed radiation fields. Characterization of radiation protection capability of different composition W-PMMA homogeneous mixtures is made by exhaustive Monte Carlo particle transport simulation using general purpose *open-source* code, FLUKA (https://fluka.cern/).

# IOP Publishing

## Year 2024

| | | | |
|---|---|---|---|
| 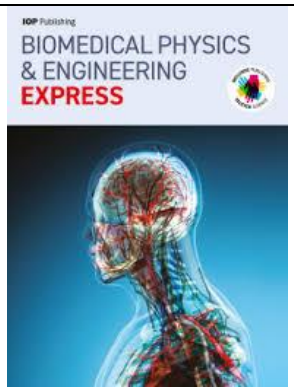 |  |  |  |
| Biomedical Physics & Engineering Express | Europhysics Letters | Environmental Research Communications | Journal of Cosmology and Astroparticle Physics |
|  |  |  | 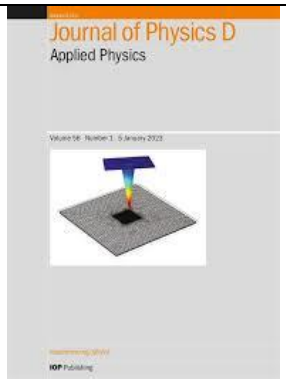 |
| Journal of Instrumentation | Journal of Physics B: Atomic, Molecular and Optical Physics | Journal of Physics: Condensed Matter | Journal of Physics D: Applied Physics |
| 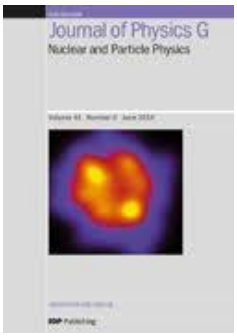 | 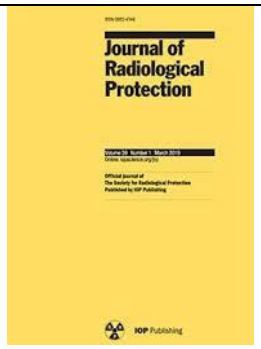 | 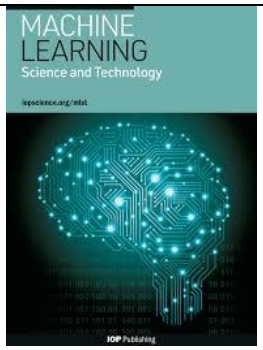 |  |
| Journal of Physics G: Nuclear and Particle Physics | Journal of Radiological Protection | Machine Learning: Science and Technology | Materials Research Express |
| 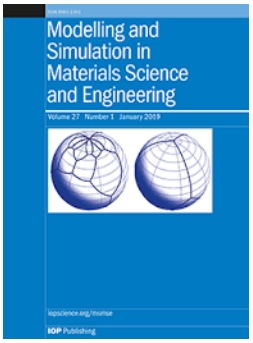 | 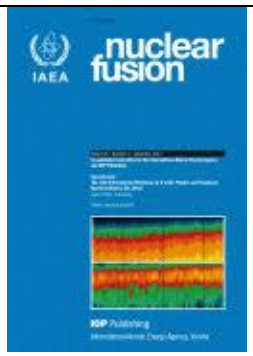 | 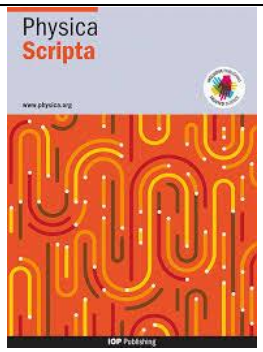 |  |
| Modelling and Simulation in Materials Science and Engineering | Nuclear Fusion | Physica Scripta | Surface Topography: Metrology and Properties |

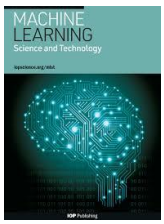

1

IOP Publishing Mach. Learn.: Sci. Technol. 5 (2024) 015011 https://doi.org/10.1088/2632-2153/ad1c31

MACHINE LEARNING
Science and Technology

PAPER

# A multi-stage machine learning algorithm for estimating personal dose equivalent using thermoluminescent dosimeter

**Munir S Pathan**[1,2,*], **S M Pradhan**[1,2], **T Palani Selvam**[1,2] and **B K Sapra**[1,2]

[1] Radiological Physics & Advisory Division, Health, Safety & Environment Group, Bhabha Atomic Research Centre, Mumbai, India
[2] Homi Bhabha National Institute, Mumbai, India
[*] Author to whom any correspondence should be addressed.

**E-mail:** mspathan@barc.gov.in

**Keywords:** radiation dosimetry, thermoluminescent dosimeters, artificial neural network, random forest algorithm

OPEN ACCESS

RECEIVED
17 August 2023

REVISED
20 November 2023

ACCEPTED FOR PUBLICATION
8 January 2024

PUBLISHED
18 January 2024



## Abstract

In the present age, marked by data-driven advancements in various fields, the importance of machine learning (ML) holds a prominent position. The ability of ML algorithms to resolve complex patterns and extract insights from large datasets has solidified its transformative potential in various scientific domains. This paper introduces an innovative application of ML techniques in the domain of radiation dosimetry. Specifically, it shows the applicability of ML in estimating the radiation dose received by occupational workers. This estimation is expressed in terms of personal dose equivalent, and it involves the utilization of thermoluminescence signals emitted by $CaSO_4$:Dy-based personnel monitoring badges. To estimate personal dose equivalent, three-stage algorithm driven by ML models is proposed. This algorithm systematically identifies the photon energy ranges, calculates the average photon energy, and determines personal dose equivalent. By implementing this approach to the conventional three-element dosimeter, the study overcomes existing limitations and enhances accuracy in dose estimation. The algorithm demonstrates 97.8% classification accuracy in discerning photon energy ranges and achieves a coefficient of determination of 0.988 for estimating average photon energy. Importantly, it also reduces the coefficient of variation of relative deviations by up to 6% for estimated personal dose equivalent, compared to existing algorithms. The study improves accuracy and establishes a new methodology for evaluating radiation exposure to occupational workers using conventional thermoluminescent dosimeter badge.

## 1. Introduction

Personnel monitoring is an essential radiation protection measure adopted in organizations dealing with the use of ionizing radiation, such as nuclear power plants, medical facilities, and research facilities. Personnel dosimeters, particularly, the thermoluminescence dosimeters (TLDs), are most commonly used to assess the dose received by radiation workers exposed to ionizing radiation from external sources. Personnel dosimeters often measure radiation exposure in terms of operational quantity which is personal dose equivalent ($H_p(d)$) such as $H_p(10)$, $H_p(0.07)$, and $H_p(3)$ [1, 2]. A realistic and conservative estimation of protection quantities is ensured by these quantities [3]. The accuracy of estimated $H_p(d)$ becomes crucial as this dose information serves as the foundation for evaluating the protection status of radiation workers, installations and practices including ensuring compliance with regulatory requirements.

In India, about 0.25 million occupational workers are monitored for external exposure due to gamma and beta radiation using $CaSO_4$:Dy-based TLD badges [4]. $CaSO_4$:Dy exhibits a strong energy-dependent response [5, 6]. To overcome this, TLD badge comprises of a TLD card with of three $CaSO_4$:Dy-Teflon discs loaded into a cassette having filters [7, 8]. However, the use of filters and the disc geometry of the dosimeter results in significant angular dependence. The energy and angular dependence of the response presents a challenge for the accurate estimation of occupational doses. The dose estimation algorithms presently used, either consider the angle-averaged response or the response at normal incidence to fit the response function

IOP Publishing Mach. Learn.: Sci. Technol. 5 (2024) 015011 M S Pathan et al

[9–13]. When dealing with lower and intermediate photon energy, both the angular and energy response changes rapidly. These variations cannot be adequately addressed using traditional, average response-based algorithms. Instead, a more flexible approach is needed, and machine learning (ML) algorithms seem to provide the necessary adaptability to account for these variations due to their capability to map complex relationships.

One of the earliest demonstrations of the potential of ML in TL dosimetry was by Moscovitch *et al* [14], who used an artificial neural network (ANN) to estimate doses in LiF:Mg:Ti-based four-element dosimeters. More recently, researchers have demonstrated the applicability of ML algorithms in TL dating, identification of anomalies in TL glow curves (GC), and classification of thermoluminescence features of natural halite [15–23]. In the present work, we aimed to develop an algorithm for estimating the average photon energy and the dose in terms of $H_p(d)$ from TL readouts of a three-element $CaSO_4$:Dy dosimeter. Two separate ML models were developed for estimating the dose in terms of $H_p(10)$ and $H_p(0.07)$. The study shows that excellent accuracy can be achieved in the estimation of $H_p(d)$ by using $CaSO_4$:Dy TLD badge with the help of ML models.

Furthermore, the present study focuses on the introduction of a data-driven approach aimed at enhancing radiation protection for occupational workers. We have developed a novel multi-stage ML technique that integrates energy estimation and dose estimation, resulting in a substantial enhancement in the precision of dose assessments, effectively transcending the limitations inherent in conventional algorithms. This novel approach is poised to play a pivotal role in strengthening occupational worker and installations safety, particularly within the diagnostic, medical, and nuclear industries where use of ionizing radiation is involved. The present study also demonstrates the significance of ML towards improving the occupational health and safety in radiation environments.

## 2. Material and methods

### 2.1. TLD badge

The TLD badge has three TL elements (Disc), each of 13.3 mm diameter and 0.8 mm thickness. They are clipped to an Aluminum plate to form the TLD card, which is inserted into a cassette having three filters/regions for the TL discs. The top disc (D1) placed between a composite metal filter, consisting of an Al filter with a thickness of 0.6 mm and Cu filter with a thickness of 1 mm. The middle disc (D2) is provided with a 1.6 mm thick Polystyrene filter. The bottom disc (D3) does not have any filters; it is covered by a polythene pouch and a paper wrapper. Figure 1 illustrates the pictorial representation of the TLD card and cassette with the filters. It is to be noted that the clip for wearing/fixing TLD badge is not shown in the figure 1.

### 2.2. Calibration and readout of TLD badge

TLD cards are read in the semi-automatic TLD badge reader using clamped heating profile [24]. The hot N2-gas is directed towards the TL element, maintaining a temperature of 285 °C for 30 s. The TL emitted during the heating cycle is recorded at every second as TL counts. For routine calibration of the TLD badge reader, TLD badges are exposed to Cs-137 gamma radiation at a distance of 50 cm in a panoramic geometry, and the badges are read in a TLD reader after 7 d to eliminate the effect of fading of low-temperature peaks. The reader calibration factor, which represents dose per unit TL counts is determined from the average TL counts from D1 and the delivered dose in terms of whole body dose or $H_p(10)/H_p(0.07)$ [24]. At present the personal dose is reported in terms of whole body dose and skin dose [24]. It is noted that the correspondence between the air-kerma/exposure for the panoramic in-air irradiation and the whole body dose/$H_p(10)$ and $H_p(0.07)$ for on phantom collimated irradiation has already been established.

To address the crosstalk observed when the three TL elements in TLD cards are sequentially heated in the TLD badge reader [25], disc calibration factors are applied. The disc calibration factors are determined by irradiating the TLD card in a 3 mm thick Perspex build-up so that all TL elements receive the same dose. After the readout, TL counts from D1 are used as a reference, and the TL counts from D2 and D3 are scaled to match D1. The scaling factors, i.e. disc calibration factors, along with reader calibration factors are always applied during the readout of service TLD badges.

### 2.3. Dataset preparation and preprocessing

Response of TLD badge in terms of operational quantities has been reported in a few studies [9, 10, 12, 13, 26]. These experimental TL response datasets were compiled, consisting of approximately 700 sets of TL readouts. The dataset contains response to various photon beams of energy 12.4 keV–1.25 MeV, angles of

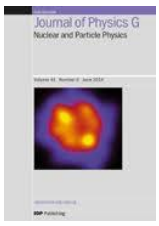

2

OPEN ACCESS
IOP Publishing
Journal of Physics G: Nuclear and Particle Physics
J. Phys. G: Nucl. Part. Phys. **51** (2024) 125102 (13pp)
https://doi.org/10.1088/1361-6471/ad8769

# Application of the surrogate reaction ratio method to measure the (*n, xp*) cross sections for nuclei with *A* ≈ 50–60

**Ramandeep Gandhi**[1,2,3,*] **and S Santra**[1,2]

[1] Nuclear Physics Division, Bhabha Atomic Research Centre, Mumbai 400085, India
[2] Homi Bhabha National Institute, Anushaktinagar, Mumbai 400094, India

E-mail: ramangandhipu@gmail.com and ssantra@barc.gov.in

Received 1 May 2024, revised 6 October 2024
Accepted for publication 16 October 2024
Published 11 November 2024

**Abstract**

We explore the applicability of the surrogate reaction (SR) ratio method for determining (*n*, *xp*) cross sections, where an incoming neutron induces the emission of at least one proton from a nuclear target with a mass range of *A* ≈ 50–60. These cross sections are relevant for advanced nuclear technologies. Our findings reveal that, under specific conditions, the SR ratio method can yield reliable (*n*, *xp*) cross sections, similar to its success in determining (*n*, *f*) cross sections in actinides. However, not all SR pairs meet these conditions across the entire excitation energy range, necessitating careful application of the SR ratio method for determining (*n*, *xp*) cross sections.

Keywords: surrogate reaction ratio method, transfer reactions, (*n*, *xp*) cross sections for radionuclides

## 1. Introduction

The cross-sectional data for n-induced reactions on a reactor's structural material has always been a top priority to assess operational characteristics and the safety of advanced reactors (e.g., fusion reactors and accelerator driven systems). The high-energy (HE) neutrons (e.g.,

[3] Present address: Semiconductor Materials Laboratory, Materials Science Section, Raja Ramanna Centre for Advanced Technology, Indore 452013, India
[*] Author to whom any correspondence should be addressed.

14.1 MeV neutrons produced by the D+T reaction in a fusion reactor) produced in these reactors open up several threshold channels (such as $(n, \alpha)$, $(n, d)$, $(n, p)$, $(n, 2n)$ and $(n, np)$ reactions) on the structural materials (stainless steel or SS) of these reactors. The HE neutron flux induce noticeable changes in the mechanical properties of the SS by altering its chemical composition through transmutation reactions. Various long-lived and short-lived radionuclei are formed in the $A \approx 50$–$60$ mass region (e.g., $^{60}$Fe, $^{53}$Mn, $^{55}$Fe, $^{54}$Mn, $^{57}$Co, $^{58}$Co and $^{62}$Cu with respective half-lives of $1.5 \times 10^6$ yr, $3.74 \times 10^6$ yr, 2.73 yr, 312.3 d, 271.79 d, 70.86 d and 9.67 min) within the SS by transmutation reactions. The n-induced $(n, xp)$ and $(n, x\alpha)$ reactions on SS that produce hydrogen (H) and helium (He) gases, are indeed crucial. These gases can accumulate (or diffuse) within the SS, resulting in material degradation mechanisms like swelling and embrittlement, which affect the reactor's operational lifespan. Therefore, obtaining accurate cross-sectional data of $(n, xp)$ and $(n, x\alpha)$ reactions on stable nuclei of SS as well as on radionuclides produced within the SS (via transmutation of SS), is vital for modeling and predicting the overall performance and lifespan of a reactor [1–9].

The n-induced reaction cross sections on stable nuclei can be directly measured by bombarding neutron beams on stable targets and detecting the reaction products. But direct measurements of n-induced reactions on unstable nuclei are sometimes extremely difficult because some nuclei are not naturally abundant, and are too difficult to produce or have half-life that is too short to serve as a target. This article exclusively centers on the surrogate reaction (SR) ratio method because it is being utilized to measure desired H-gas producing $(n, p)$ [10] and $(n, xp)$ [8, 9, 11, 12] cross sections for unstable nuclei in the $A \approx 50$–$60$ mass region.

Initially, surrogate techniques were utilized to determine the cross sections for $(n, f)$ and $(n, \gamma)$ reactions on unstable targets and historical development of these surrogate works can be found in [13]. In recent decade, a sizable number of experimental and theoretical developments have been made to apply the surrogate approach for determining various compound nuclear decay channels such as $(n, \alpha)$, $(n, p)$, $(n, xp)$, $(n, f)$, $(p, f)$, $(n, \gamma)$, $(n, n')$ and $(n, 2n)$ reactions [8–12, 14–26]. In a surrogate technique, the desired compound nucleus is formed through alternate stable target + beam combination and it is assumed that decay of the compound nucleus does not depend on the pathway leading to its formation. Application of the surrogate techniques involves various assumptions [13]. Researchers [27–29] have examined the validity of these assumptions and, applicability of the surrogate techniques to determine the $(n, f)$ and $(n, \gamma)$ cross sections for actinides and rare-earth nuclei. They have concluded that the determined cross sections are of desirable accuracy within a specific energy range, provided that certain conditions are met. Similar examinations [15, 26] have been made to check the applicability of surrogate techniques for determining the $(n, p)$, $(n, n')$ and $(n, 2n)$ cross sections. Recently, A. Sharma et al [30] have determined the $^{56}$Fe$(n, xp)$ cross sections by using the SR ratio method and compared their results with the directly measured $^{56}$Fe$(n, xp)$ cross sections available in the EXFOR [31]. It was observed that the surrogate data is not consistent with the corresponding n-induced direct measurements and concluded that the above method is unsuitable for determining $(n, xp)$ cross section. On the other hand, in our recent works [8, 9] we have utilized the above method to determine the cross sections for $^{57,58}$Co$(n, xp)$ reactions after addressing the reliability of the method in the measured energy region. Thus, the reliability conditions of the application of this method to determine the $(n, xp)$ cross sections for $A \approx 50$–$60$ mass region nuclei are yet to be settled.

The motivation of the present work is to investigate in detail the conditions under which the SR ratio method can be employed, if at all, to determine the $(n, xp)$ cross sections for the above target mass region. In the following section we have briefed the strategy applied in the surrogate methods and the associated approximations. Theoretical calculations and results of

3

IOP Publishing Environ. Res. Commun. 6 (2024) 085023 https://doi.org/10.1088/2515-7620/ad66b5

Environmental Research Communications

PAPER

# Assessment of bioaccumulation factors of trace metals for Upper Gangetic fish

OPEN ACCESS

RECEIVED
21 February 2024

REVISED
10 July 2024

ACCEPTED FOR PUBLICATION
23 July 2024

PUBLISHED
29 August 2024



Vyom Saxena

Industrial Hygiene & Safety Section, Health, Safety & Environment Group, Bhabha Atomic Research Centre, Mumbai, 400085, India

E-mail: vyomsaxena2@gmail.com

**Keywords:** bioaccumulation factor, atomic absorption spectrometry, trace metals, River Ganga, fresh water fish

## Abstract

The River Ganga basin is home to over 520 million people and 2500 species of flora and fauna, including several fish species. This study determines the bioaccumulation factors of fish for five trace metals, namely Cu, Fe, Zn, Mn, and Cr, in a stretch of the River Ganga in the upper Gangetic alluvial plain with limited industrial activities. The abundance of different trace metals in the water follows the order Fe > Zn > Mn > Cu > Cr. The concentrations in fish show a slightly different pattern and follow the relative quantitative order as Zn >≈ Fe >Mn > Cu >Cr. The trace metal levels in fish are well below the permissible limits set by various regulatory agencies. The bioaccumulation factor values are in order Zn>Cr>Mn>Cu>Fe. This stretch of the Ganga has not been extensively investigated for bioaccumulation by aquatic organisms. These values, therefore, represent site-specific baseline data for future anthropogenic activities that may affect the trace metal profile in this part of the Gangetic aquatic system. The study is also significant due to the presence of the Narora nuclear power plants, as the bioaccumulation factors of stable elements help predict the behavior of their radioactive counterparts and homologous elements in the environment.

## 1. Introduction

The River Ganga originates in the Himalayas in the state of Uttarakhand, India. The 2,704 km long river Ganga constitutes nearly 25% of India's freshwater resources and covers a heavily populated basin area of 861,404 $km^2$(GRBMP 2015). The entire Ganga drainage is estimated to be home to 350 fish species, several of which are endemic to the Ganga (Allen *et al* (2010)). A major study during 2007–2009 recorded a total of 133 native fish species in the Ganga River and its tributaries (Sarkar *et al* 2012). The river receives industrial and domestic sewage, apart from agricultural runoff, during its course (Paul 2017, Matta *et al* 2018). Heavy metals enter the rivers mainly from anthropogenic sources such as industrial discharges, fertilizers, mining, and domestic sewage (Pandey *et al* 2010, Martín *et al* 2015, Paul 2017, Genc and Yilmaz 2018). Although most heavy metals are toxic even in trace amounts, some (e.g., Cu, Fe, Mn, Ni, and Zn) are essential nutrients in trace amounts for biological processes but become toxic at higher concentrations (Li Daoliang 2019). Such heavy metals are, therefore, also classified as trace metals due to their presence in trace concentrations (Tchounwou *et al* 2012).

Metals from natural and anthropogenic sources entering the surface waters can be accumulated by aquatic organisms, including fish (Sara Karlsson 2002, Hosseini et al 2012). Trace metals mainly enter the aquatic food chain by direct consumption of water and food via the digestive tract and through muscles and gills (Oliveira Ribeiro *et al* 2005). Levels of heavy metals in fish usually depend on the levels found in the ambient aquatic environment of their habitat (Oliveira Ribeiro *et al* 2005, Obasohan *et al* 2008, Nhiwatiwa *et al* 2011, Annabi *et al* 2013). Heavy metal uptake in fish has been studied worldwide, including in the middle and lower Gangetic stretch (Prayagraj, West Bengal, Bangladesh). Research has revealed that metal accumulation in fish also depends on the type of metal (Genc and Yilmaz 2018, Maurya and Malik 2018, Sivakumar and Xiaoyu 2018, Oyakhilome and Ajiwe Vincent 2019). Bhattacharya *et al* studied the heavy metals' accumulation in water and fish at Rishra-Konnagar in the lower Gangetic stretch in West Bengal (Bhattacharya *et al* 2008). They concluded that Zn, Cr,

Cu, Cd, and Pb concentrations of heavy metals in water and commercially edible fish samples followed the trend: Zn > Cr > Cu > Cd > Pb. Similarly, Kar *et al* analyzed river Ganga water in West Bengal and reported the concentration patterns as Fe> Mn > Ni > Cr > Pb > Zn > Cu >Cd (Kar *et al* 2008). Gupta *et al* studied the bioaccumulation of metals Cu, Cr, Cd, Pb, and Zn in two catfish species of the middle Gangatic stretch at Prayagraj and reported heavy metal concentration patterns in Ganga water to be in the order Zn > Pb > Cu > Cr > Cd (Gupta *et al* 2009). Hossain *et al* studied metal bioaccumulation in 15 commonly consumed fishes from the lower Meghna River and adjacent areas of Bangladesh and found the concentration (mg $kg^{-1}$ wet weight) of selected metals in the order Fe > Zn > Cu > Cr > Mn (Hossain *et al* 2022). However, the upper Gangetic or the doab stretch of the River Ganga in the western part of the state of Uttar Pradesh, India has not been much investigated for the bioaccumulation of trace metals by fish. This study aims to address this gap by determining site-specific bioaccumulation factors in a representative section of the upper Gangetic region.

### 1.1. Bioaccumulation Factor (B.F.) and the significance of the present study

The Bioaccumulation Factor (B.F. or BAF) is the equilibrium ratio of the concentration of an element (or chemical) in the aquatic organism or tissue (fresh weight or dry weight) to the concentration of that element (or chemical) in the water. It is also symbolized as Bρ (Safety Series-57 1982, USEPA 1994) and referred to as Concentration Factor (C.F.) (Technical Report Series-364 1994) or Concentration Ratio (C.R.) (Staven *et al* 2003). This is generally accepted as a dimensionless parameter, though some works assign it units such as mg $kg^{-1}$ (wet or dry weight) per mg $l^{-1}$ of water, or in some works, L $kg^{-1}$ (Safety Series-57 1982, NCRP-76 1984, Technical Report Series-364 1994). This parameter is highly variable and can range, in some cases, over several orders of magnitude for a particular element or organism (Heinz *et al* 1999, Safety Series-57 1982). The present work has adopted Bioaccumulation Factors (B.F.) as a dimensionless coefficient, mathematically represented as follows (NCRP-76 1984):

$$B.F.=\frac{Concentration\ of\ element/chemical/\ radionuclide\ per\ unit\ fresh\ weight\ in\ tissue}{Concentration\ of\ element/chemical/\ radionuclide\ in\ water} \quad (1)$$

Various regulatory agencies suggest different criteria for the assessment of bioaccumulation endpoints. The European Union defines a chemical as 'bioaccumulative' if the Bio Concentration Factor (BCF) is $\geqslant$ 2000 and 'very bioaccumulative' if the BCF value is $\geqslant$ 5000. According to the US Environmental Protection Agency (USEPA), the BCF values for 'bioaccumulative' and 'very bioaccumulative' are 1000–5000 and $\geqslant$ 5000, respectively (Arnot and Gobas 2006). A detailed analysis of bioaccumulation factors used in regulatory assessments of organic chemicals in aquatic organisms is provided in a review by Arnot and Gobas (Arnot and Gobas 2006). As per this review, regulatory frameworks often consider bioaccumulation factor values greater than 1,000 to indicate a significant potential for bioaccumulation (Noman *et al* 2022). However, some references consider an average B.F. value exceeding one to indicate probable bioaccumulation of the metal from water, but not significant unless the B.F. is greater than 100 (Yu *et al* 2012, Zhe *et al* , Feng *et al* 2020).

Aquatic organisms also assimilate radionuclides discharged into the aquatic environment. The variability in the B.F. among isotopes of an element is minor compared to the variability among different elements and the general inherent variance in these parameters. Values of B.F. for radioisotopes can therefore be derived from stable element data and predicted by analogy, i.e., by selecting an element whose behavior is expected to be similar, such as homologous elements that belong to the same group of the periodic table (Safety Series-57 1982). The assessment of bioaccumulation factors of stable elements is of great help in predicting the behavior of their radioactive counterparts or homologous elements in the environment. This aspect of the study is extremely useful in regions with industries that have the potential for normal or accidental releases of radionuclides or other chemicals (Steven *et al* 2003, Uchida *et al* 2007). An isotope is considered radiologically important if it has a reasonably long half-life, high specific activity, high beta and gamma energies, significant branching ratios, a biologically selective nature (organ seeker), good fission yield, or importance in the human food chain (Technical Report Series-364 1994). In addition to generating fission products, nuclear reactor operation produces activation products from nuclear reactions with the structural materials in the reactor core. Stainless steel, an important material used in nuclear reactor components, results in the formation of several radionuclides due to nuclear reactions. These include $^{60}Co$, $^{65}Zn$, $^{59}Fe$, $^{51}Cr$, $^{54}Mn$, $^{55}Fe$, $^{63}Ni$, and $^{64}Cu$ - all of which have moderately long half-lives and high Gamma activities (Eisenbud 1997).

The present study is a systematic effort to address the gaps in the bioaccumulation factor data for five trace metals significant from radiological, environmental, fish, and human health perspectives. The primary objective of the study is its radiological significance due to the presence of two nuclear reactors at the study location. The bioaccumulation factor values derived for stable elements can be used to predict the transport, bioaccumulation, and human uptake of their radioisotopic counterparts released into the environment during normal reactor operations or accidental conditions (NCRP-76 1984).

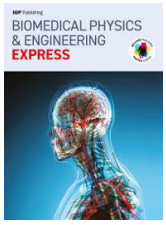


4

IOP Publishing Biomed. Phys. Eng. Express 10 (2024) 035004 https://doi.org/10.1088/2057-1976/ad2b02

Biomedical Physics & Engineering Express

PAPER

# Calculation of biological effectiveness of SOBP proton beams: a TOPAS Monte Carlo study

**Arghya Chattaraj**[1,2] **and T Palani Selvam**[1,2]

[1] Radiological Physics and Advisory Division, Health, Safety and Environment Group, Bhabha Atomic Research Centre, Mumbai—400 085, India

[2] Homi Bhabha National Institute, Anushaktinagar, Mumbai—400 094, India

**E-mail:** pselvam@barc.gov.in

**Keywords:** relative biological effectiveness, TOPAS Monte Carlo, microdosimetry, SOBP protons

OPEN ACCESS

RECEIVED
1 November 2023

REVISED
6 February 2024

ACCEPTED FOR PUBLICATION
20 February 2024

PUBLISHED
8 March 2024



## Abstract

*Objective.* This study aims to investigate the biological effectiveness of Spread-Out Bragg-Peak (SOBP) proton beams with initial kinetic energies 50–250 MeV at different depths in water using TOPAS Monte Carlo code. *Approach.* The study modelled SOBP proton beams using TOPAS time feature. Various LET-based models and Repair-Misrepair-Fixation model were employed to calculate Relative Biological Effectiveness (RBE) for V79 cell lines at different on-axis depths based on TOPAS. Microdosimetric Kinetic Model and biological weighting function-based models, which utilize microdosimetric distributions, were also used to estimate the RBE. A phase-space-based method was adopted for calculating microdosimetric distributions. *Main results.* The trend of variation of RBE with depth is similar in all the RBE models, but the absolute RBE values vary based on the calculation models. RBE sharply increases at the distal edge of SOBP proton beams. In the entrance region of all the proton beams, RBE values at 4 Gy i.e. RBE(4 Gy) resulting from different models are in the range of 1.04–1.07, comparable to clinically used generic RBE of 1.1. Moving from the proximal to distal end of the SOBP, RBE(4 Gy) is in the range of 1.15–1.33, 1.13–1.21, 1.11–1.17, 1.13–1.18 and 1.17–1.21, respectively for 50, 100, 150, 200 and 250 MeV SOBP beams, whereas at the distal dose fall-off region, these values are 1.68, 1.53, 1.44, 1.42 and 1.40, respectively. *Significance.* The study emphasises application of depth-, dose- and energy- dependent RBE values in clinical application of proton beams.

## 1. Introduction

Proton therapy is one of the fast-growing treatment modalities in radiotherapy. One of the important features of proton therapy is its inherent tissue-sparing capabilities which reduces the burden of treatment-related complications on patients and the healthcare system (Newhauser and Zhang 2015). The potential advantage of using proton beams for clinical purpose is related to their distinct energy deposition characteristics. The Bragg curve, generated by monoenergetic protons, exhibits a well-defined, localized peak at the end of the proton track (Raju *et al* 1978). This results in low dose deposition to the healthy tissue which leads to a reduction in normal tissue toxicity (Lühr *et al* 2018). Moreover, proton therapy presents the additional benefit of lower integral dose deposition when compared to modern photon-based therapies such as Intensity Modulated Radiation Therapy or Volumetric Modulated Arc Therapy. This characteristic underscore the potential of proton therapy to reduce the risk of secondary neoplasms to develop (Lühr *et al* 2018). Adhering to clinical requisites, the Spread-out Bragg peak (SOBP) can be generated by modulating the proton energy, ensuring the uniform delivery of the prescribed dose across the targeted volume (Conte *et al* 2019).

The biological effectiveness of ionizing radiation depends on the Linear Energy Transfer (LET) of the interacting particles (Conte *et al* 2019). In contrast to low-LET particles, high-LET particles produce clusters of interactions in few of the irradiated cells (Conte *et al* 2019). These clusters give rise to highly complex patterns of damage. In the context of particles other

IOP Publishing Biomed. Phys. Eng. Express 10 (2024) 035004 A Chattaraj and T P Selvam

than electrons and photons, the absorbed dose needs to be weighted by the appropriate Relative Biological Effectiveness (RBE) (Conte *et al* 2019).

One of the major concerns in proton therapy treatment planning, especially for sites closely located to organs at risk, is the uncertainties associated with the RBE value of clinical proton beams (Koh *et al* 2022). Upon interaction with matter, high-energy protons give rise to a composite radiation field comprising diverse particles, each possessing varying LET(Conte *et al* 2019). At any given depth, both primary and secondary particles produced from non-elastic nuclear interactions of protons contribute to the biological damage of the living systems (Paganetti 2002). Consequently, the resulting RBE of this composite radiation field reflects the amalgamation of RBE values attributed to multiple constituents of the resultant mixed radiation spectrum (Conte *et al* 2019). In current clinical practice, proton therapy treatments are planned assuming a constant RBE value of 1.1 irrespective of beam energy, treatment depth and biological endpoints (Paganetti 2014, Qutub *et al* 2016, Newpower *et al* 2019). However, the dependency of RBE on factors like LET, cell or tissue type, and dose per fraction leads to fluctuations in RBE along the depth-dose profile (Giovannini *et al* 2016, Qutub *et al* 2016). Lühr *et al* (2018) extensively explored the existing understanding of the upcoming challenges pertaining to the RBE in the context of proton beam therapy. Qutub *et al* (2016) introduced a straightforward algorithm for risk assessment in RBE-weighted treatment planning across a two-dimensional plane, and they compared the outcomes with those derived from the conventional RBE assumption of 1.1.

Several radiobiological experimental studies reported an increasing trend of RBE along the SOBP and the RBE values vary significantly from the constant value of 1.1 (Paganetti *et al* 2002, Chaudhary *et al* 2014, Paganetti 2014, Conte *et al* 2019). Paganetti *et al* (2002) experimentally showed that the RBE of SOBP proton beams (65–250 MeV) varies from 0.9–2.1 for in-vitro scenarios, whereas in-vivo RBE values vary from 0.7–1.6 (Paganetti *et al* 2002). Chaudhary *et al* (2014) measured variation in cell killing RBE for both Human fibroblasts (AG01522) and glioma (U87) cells across varying depths, employing 62 MeV monoenergetic and SOBP proton beams. The authors then compared their experimental findings against that calculated using Geant4 Monte Carlo toolkit coupled with Local Effect Model (LEM). The outcomes of the study revealed a significant variance between the predicted biological dose, which was calculated using the variable RBE extracted from the experimental data, and the conventionally utilized constant RBE value of 1.1 in clinical practice (Chaudhary *et al* 2014).The RBE value derived from radio-biological experiments is a precisely defined parameter and its applicability remains confined to the specific experimental circumstances. Directly extrapolating this value to patient scenarios is generally not possible (Fossati *et al* 2018). Furthermore, radiobiological experiment for measuring RBE is expensive and very time consuming. Several phenomenological and biophysical models based on microdosimetric distributions and dose-average LET ($LET_d$) are proposed for predicting RBE more conveniently (Griffiths 1985, Paganetti *et al* 2002, Paganetti 2014, Giovannini *et al* 2016, Qutub *et al* 2016, Lühr *et al* 2018, Takada *et al* 2018, Conte *et al* 2019, Newpower *et al* 2019, Colautti *et al* 2020). The $LET_d$ is not a directly measurable quantity and it can be calculated using Monte Carlo methods as they are capable of transporting all the primary and secondary particles (Conte *et al* 2019). The precision and accuracy of simulated $LET_d$ values can be influenced by uncertainties in cross sections and the sensitivity of LET distributions to frequently adjustable simulation parameters (Conte *et al* 2019). Microdosimetric technique is an efficient approach to model RBE of ionizing radiations (Griffiths 1985, Anderson *et al* 2017, Conte *et al* 2019, Vassiliev *et al* 2019). Microdosimetry measures not only the average dose but the pattern of dose deposition at the micrometric scale (Conte *et al* 2019). Microdosimetric distributions can be measured and it can also be calculated using Monte Carlo codes. Several published studies are available on estimation of RBE of protons based on microdosimetric distributions and $LET_d$ (Takada *et al* 2018, Conte *et al* 2019, Newpower *et al* 2019, Colautti *et al* 2020). The majority of the microdosimetry-based studies are based on measured microdosimetric distributions and for limited SOBP proton beams such as 62 and 155 MeV SOBP beams (Kase *et al* 2013, Takada *et al* 2018, Conte *et al* 2019, Newpower *et al* 2019, Colautti *et al* 2020). It's worth highlighting that the instrument dependent threshold value for $y$ in the range of 0.3–0.5 keV/$\mu$m for reducing the electronic noise may affect the bin-wise yield of measured microdosimetric distributions, particularly in the low $y$ region (Rollet *et al* 2004, Chattaraj and Selvam 2020). Additionally, the measurements may suffer from inherent uncertainties such as detector position accuracy, experimental setup variations, variation in gas pressure of the filling gas of the Tissue Equivalent Proportional Counter (TEPC) etc. Notably, these limitations are absent in Monte Carlo calculations (Chattaraj *et al* 2019).

Numerous published investigations have explored the assessment of RBE for clinical proton beams (Paganetti *et al* 2002, Chaudhary *et al* 2014, Paganetti 2014, Conte *et al* 2019). Predominantly, these studies are based on radiobiological experiments. A more limited subset of published works has focused on measured microdosimetric distributions specifically for 62 and 155 MeV SOBP proton beams (Kase *et al* 2013, Conte *et al* 2019). Yet, a significant gap remains in the literature, as there lacks a report on Monte Carlo-based microdosimetric distributions for SOBP proton beams aimed at RBE estimation as a function of proton energy and depths in water.

This present study endeavours to compute the RBE of SOBP proton beams as a dynamic function of

5

OPEN ACCESS
IOP Publishing
Journal of Physics: Condensed Matter
J. Phys.: Condens. Matter **37** (2025) 045402 (9pp)
https://doi.org/10.1088/1361-648X/ad8b8f

# Charge transfer induced phase transition in $Li_2MnO_3$ at high pressure

**Ajinkya P Khangal[1,2], Nishant N Patel[1] and Ajay K Mishra[1,2,*]**

[1] High Pressure & Synchrotron Radiation Physics Division, Bhabha Atomic Research Centre, Trombay, Mumbai 400085, India
[2] Homi Bhabha National Institute, Anushaktinagar, Mumbai 400094, India

E-mail: akmishra@barc.gov.in

Received 16 July 2024, revised 15 October 2024
Accepted for publication 25 October 2024
Published 12 November 2024

**Abstract**

Efficient and better energy storage materials are of utmost technological importance to reduce energy dependence on the fossil fuels. $Li_2MnO_3$ is one such material having potential to meet most of the requirements for energy storage. This material has been synthesized using solid state synthesis route. High pressure structural and vibrational studies on this material have been carried out upto ~22 and 26 GPa respectively. These investigations show occurrence of a hitherto unknown second order phase transition to a new low symmetry phase whose symmetry is constrained to be monoclinic with space group $P2_1/n$ at pressure of ~2.3 GPa in $Li_2MnO_3$. The bulk modulus and its derivative determined by fitting the $P$–$V$ data with third order Birch–Murnaghan equation of state are 113.3 ± 13.1 GPa and 4.1 ± 1.2 respectively. Mode Grüneisen parameter calculated for all the Raman modes show positive values which indicates the absence of any soft mode in this material. A microscopic mechanism based on bond-charge transfer is invoked and applied to understand the spectroscopic changes occurring in this material which also manifests second order structural phase transition. Enhancement in covalent character of Li–O bonds in the Li–O polyhedra is inferred based on the spectroscopic observation and above mechanism.

Keywords: Raman scattering, x-ray diffraction, high pressure, charge transfer, phase transition

## 1. Introduction

Energy requirement of the growing world population demand consumption of higher amount of non-renewable energy sources such as fossil fuels leading to severe global warming related problems. The key for providing alternative solution to problems related with fossil fuel exhaustion and global warming etc [1, 2]. Could be the lithium ion based batteries which are very promising power storage sources. Li-ion batteries power almost all the electrical devices in our day-to-day life; let it be mobile phones, laptops, etc. There has been a substantial increase in demand for Li-ion batteries with high power and energy density, for large-scale applications such as electric vehicles, which are more environment friendly as compared to their counterpart vehicles, which primarily use fossil fuels. Li-rich materials, particularly the transition metal oxides have more importance as cathode materials due to their intrinsic ability to provide high reversible capacity on subsequent electrochemical activation [3].

$Li_2MnO_3$ (LMO) is one such lithium rich manganese (Mn) based cathode material with high energy density and is a promising future candidate in Li-ion batteries [4]. This is feasible as manganese oxide intercalated with lithium is economical, safer, and less toxic battery material. $MnO_6$ octahedral

* Author to whom any correspondence should be addressed.

units separated by lithium layers are basic building blocks of $Li_2MnO_3$. In general, Mn cannot be oxidized beyond +4 oxidation state in octahedral oxygen environment which limits the highest voltage obtained in Mn based cells. The higher oxidation state of Mn represents the *d*-orbital lying in lower energy level and therefore higher electrode potentials. The inability of Mn to be oxidized beyond +4 further limits the extraction of Lithium from Lithium manganese oxide. The removal of $Li^+$ ion from lithium manganese oxide is accompanied by the oxidation of Mn beyond +4. Thus, it limits the cell capacity to store the charge. However, $Mn^{4+}$ compound of $Li_2MnO_3$ adopt layered structure and it is rich in $Li^+$ ions, the removal of $Li^+$ ion from Lithium manganese oxide can be feasible by simultaneous removal of oxygen in the form of $Li_2O$ to balance the charge [5, 6].

LMO shows a good electrochemical characteristic making it a potential candidate for rechargeable lithium batteries. Based on earlier studies, it has been found that the energy capacities of this material depend on its synthesis conditions and test parameters, and a range of discharging capacity values have been reported. Synthesis method plays an important role in the optimization of the crystal structure, particle size and morphology [7]. In fact, earlier studies on LMO by implementing different synthesis methods, precursors, and different annealing conditions, have suggested the use of Li-rich materials rather than relying on Li-ion battery material [8]. From the point of view of positive electrodes in lithium cells, it was demonstrated that the cathodes comprising nanoparticles of $LiMn_{0.5}Ni_{0.5}O_2$ [8] and $LiMn_{1.5}Ni_{0.5}O_4$ [9] display faster kinetics than electrodes based on micrometric-size particles. Theoretical calculations have also been implemented to study the thermodynamic properties of LMO [10]. It has been reported that Li+ ion of LMO is exchange with $H^+$ ion generated from alkyl carbonate electrolyte at 4.5 V and 55 °C during charging. This is a two-step process, initially in the first step, by charging at 30 °C, $Li^+$ ion is removed from LMO by elimination of oxygen from oxide lattice and in the second step as charging temperature reaches to 55 °C, $Li^+$ ion exchange with $H^+$ of electrolyte [11]. Lithium intercalated manganese oxides, being technologically important, have been widely explored owing to their structural diversity such as spinel, orthorhombic and layered type of structures. Hence, it is very interesting to understand the vibrational and structural properties of this material under varying thermodynamic conditions such as pressure.

Raman spectroscopy being more sensitive to short-range ordering has been employed to understand the local molecular level structure/dynamics in this material. Here, we report the high pressure behaviour of $Li_2MnO_3$ investigated through Raman scattering and x-ray diffraction techniques at high pressures up to ∼26 and 22 GPa respectively with the aim to understand its structural integrity and phase changes occurring in LMO with compression.

## 2. Structural details

Lithium Manganese Oxide (LMO) belongs to the space group C12/c1, having monoclinic structure at ambient pressure and room temperature conditions. $Li_2MnO_3$ adopts a layered structure having an ABCABC stacking. One third of the crystallographic positions in the Mn-plane are replaced by Li to form an ordered $LiMn_2$ slab while the octahedral sites of the inter-slab are only occupied by lithium ions [11, 12] as shown in figure 1. The advantage of Li-rich materials is that the additional Li+ ions in the transition metal layer causes an in-plane ordering, which changes the structural symmetry from R-3 m to C2/c [13]. $Li_2MnO_3$ crystallises with lattice parameter as $a = 4.921$ Å, $b = 8.526$ Å, $c = 9.606$ Å and $\beta = 99.47°$ as reported by Strobel and Andron [11]. This consists of $MnO_6$ octahedral with Mn in 4+ state. In this structure the Inter slab octahedral sites are occupied by lithium (Li) atoms only which are called as 'interlayer Li' atoms forming edge shared polyhedral network. Moreover, another type of Li ions exist in the Mn–Li–Mn layer as an alternate ordering of Mn and Li. It is noteworthy here that Mn–O and Li–O polyhedra are all connected by edge sharing in LMO i.e. the Mn–O octahedral connect with each other by edge sharing (two O atoms) forming one-dimensional 'twisted chains', and these chains are assembled by sharing O vertex, making LMO look like a regular porous material as seen in figure 1. For the sake of clarity, first type of Li atoms are written as ($Li_{inter}$) and second type of atoms are described as ($Li_{intra}$) hereafter.

## 3. Experimental details

### 3.1. Synthesis

$Li_2MnO_3$ was synthesised by solid state reaction method using analytical grade $Li_2CO_3$ and $MnO_2$ as the starting reactant materials as described by the chemical reaction given below.

$$Li_2CO_3 + MnO_2 \rightarrow Li_2MnO_3 + CO_2. \quad (1)$$

The as synthesized sample has been characterized using, x-ray diffraction, Raman scattering and SEM-EDX [14]. More details about the synthesis procedure and sample characterization results are reported in [14].

### 3.2. Raman measurements

For generating high pressure, modified Mao Bell type of diamond anvil cell having culet diameter ∼400 $\mu$m as shown in figure 2 has been used in combination with a lever arm mechanism based device to apply force on the sample through diamond anvils [15].

A metallic (steel/tungsten) gasket with initial thickness ∼250 $\mu$m is indented to ∼60 $\mu$m and sample chamber is made

6

IOP Publishing Mater. Res. Express 11 (2024) 076506 https://doi.org/10.1088/2053-1591/ad5cd8

Materials Research Express

PAPER

# Comparison of mathematical and supervised machine-learning models for ductile-to-brittle transition in bcc alloys

**Parag M Ahmedabadi**

Materials Processing & Corrosion Engineering Division, Bhabha Atomic Research Centre, Trombay, Mumbai 400 085, India

**E-mail:** aparag@barc.gov.in

**Keywords:** impact energy, mathematical models, supervised machine learning, normalized impact energy, ductile-to-brittle transition

OPEN ACCESS

RECEIVED
3 April 2024

REVISED
18 June 2024

ACCEPTED FOR PUBLICATION
27 June 2024

PUBLISHED
8 July 2024



## Abstract

This study focuses on modelling Ductile-to-Brittle Transition (DBT) curves using various mathematical and supervised machine learning models. Charpy impact energy values are converted to normalized energy values to account for reductions in upper-shelf energy. The research introduces a saturation parameter in mathematical models to capture these variations and examines the influence of alloying elements, microstructure, and neutron irradiation on DBT behaviour in nuclear structural materials. Detailed analyses reveal how fitting parameters vary with these factors and demonstrate that mathematical models' fitting parameters generally align with observed DBT curve trends. The predictive capabilities of these mathematical models are also compared with those of supervised machine learning models, highlighting the strengths and limitations of each approach in modelling DBT behaviour. An explainable approach is used for interpretation of machine learning models and it is shown that this approach can be effectively used for the influence of various independent parameters on impact energy.

## 1. Introduction

Ductile-to-Brittle Transition (DBT) is observed in bcc (body centred cubic) metals and alloys [1] that results in change in the fracture mode from ductile to brittle at temperatures lower than room temperatures [1]. It is associated with the sharp reduction in impact energy (as determined by impact testing of notched specimens) at such lower temperatures. Such a transition is not observed in fcc metals and alloys. The DBT curves show variation of impact energy with temperature and exhibit typical sigmoidal behaviour. A typical DBT curve consists of three region viz. upper shelf (comparatively higher impact energy, ductile fracture), transition regions (sharp reduction in impact energy), and lower shelf (lower impact energy, brittle fracture). The DBT behaviour is influenced by several factors, e.g. nature of alloying elements [2], secondary phases in matrix [3], radiation damage in Reactor Pressure Vessel (RPV) steels [4–8], microstructure [9], residual strain [10], grain boundary characteristics [11].

To evaluate impact energy, Charpy V-notch specimens are generally used [12], however, Charpy U-notch specimens are also used to evaluate DBT curves [13]. The DBT curves are generally modelled using sigmoidal functions such as the hyperbolic tangent (tanh) function [14–16]. Analysis of impact energy have also been done using Bayesian approach [17, 18] and data-mining approach using rough-set theory [19]. Modelling of the transition region of the DBT curves has been also attempted in the past using an Avrami equation [20]. Two-parameters exponential curve [21] and an error function [22] were also used to model the DBT curves. Other approaches for modelling Charpy impact energy include neuro-fuzzy models [23], granular computing [24], numerical modelling [25], and Gaussian mixture models [26]. Fracture simulation model was developed for prediction from Charpy impact test data in DBT temperature range [27]. Charpy impact toughness was also predicted using combination of micromechanics and stochastic fracture model in low alloy steel [28].

IOP Publishing Mater. Res. Express 11 (2024) 076506 P M Ahmedabadi

Using tanh-function, the impact energy, $E$, is given by following equation [14, 15]:

$$E = A + B\tanh\left(\frac{T - T_0}{C}\right)$$

Here, the parameter $C$ is a measure of the slope in the transition region between upper and lower shelf. And, $T_0$ is the temperature at the mid-point of the transition, $A + B$ represents the upper shelf energy, and $A - B$ represents the lower shelf energy. The above equation can also be represented in another way as follows (Boltzmann sigmoid) [3, 29]:

$$E = \frac{E_L - E_U}{1 + \exp(\beta(T - T_0))} + E_U \tag{1}$$

Here, $E_U$ and $E_L$ are the upper and lower shelf energy, respectively, $T_0$ is the temperature corresponding to the average of the upper and lower shelf energy, $\beta$ represents the slope in the transition region.

Sometimes, the values of impact energy are used in models after converting them to normalized impact energy, $f_D$, which can be defined as follows [15]:

$$f_D = \frac{E - E_L}{E_U - E_L} \tag{2}$$

Clearly, the value of $f_D$ lies in the interval [0, 1] with $f_D = 0$ refers to the lower shelf energy and $f_D = 1$ refers to the upper shelf energy. Hence, equation (1) can be written, using equation (2), as

$$f_D = \frac{1}{1 + \exp(-\alpha(T - T_0))} \tag{3}$$

Here, $\alpha$ is a positive parameter for the DBT curves and is related to the slope in the transition region.

In addition, two other sigmoidal models have also used to fit impact energy data using normalized energy [15, 16]. These models are

$$f_D = (1 + \exp(-k(T - T_0)))^{-m} \quad \text{(Burr distribution)}$$
$$f_D = 1 - \exp(-k(T - T_0)^{-m}) \quad \text{(Weibull distribution)}$$

Here, $k$, $T_0$, and $m$ are fitting parameters. The parameter $f_D$ correlates with the fraction of ductile fracture on the specimen's surface after impact testing. The fraction of brittle region $f_B$ can be correlated to $f_D$ as follows ($f_B + f_D = 1$)

$$f_B = 1 - f_D = \frac{E_U - E}{E_U - E_L} \tag{4}$$

$$f_B = \frac{\exp(-\beta(T - T_0))}{1 + \exp(-\beta(T - T_0))} \tag{5}$$

Thus, $f_D$ normalizes impact energy for each DBT curve in the range of [0, 1] .

The increase in the value of $f_D$ with the increase in temperature can be described as the transformation of brittle regions to ductile regions on fracture surfaces. The rate of transformation in the value of $f_D$ with respect to temperature can be obtained by differentiating equation (3):

$$\frac{df_D}{dT} = \alpha f_D(1 - f_D) = \alpha f_D f_B \tag{6}$$

Thus, the rate of transformation from brittle to ductile fracture with temperature is directly proportional to the product of the fractions of ductile and brittle regions. Also, the rate of change of impact energy with temperature can be obtained by differentiating equation (1)

$$\frac{dE}{dT} = \beta(E_U - E)(E - E_L) \tag{7}$$

Equation (7) can be derived from (6) using the definitions given in equations (2) and (4). This leads to the following relationship

$$\alpha = \beta\Delta E \tag{8}$$

Here $\Delta E = E_U - E_L$ is the difference between the upper shelf and lower shelf energy.

However, this can be a limitation when studying the effect of a particular parameter on impact energy. For example, it is known that an increase in the carbon content in plain carbon steels reduces impact energy, i.e., the upper shelf energy decreases with an increase in the carbon content. The above approach always maps the impact energy in the range of [0, 1]. Hence, while comparing the effect of carbon content on impact energy, the reduction in the upper shelf energy is not reflected in the definition of $f_D$ and $f_B$.

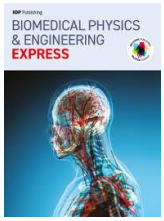


7

IOP Publishing Biomed. Phys. Eng. Express 10 (2024) 025022 https://doi.org/10.1088/2057-1976/ad222a

Biomedical Physics & Engineering Express

PAPER

# Dosimetry audit in advanced radiotherapy using in-house developed anthropomorphic head & neck phantom

Nitin R Kakade[1], Rajesh Kumar[1], S D Sharma[1,2] and B K Sapra[1,2]

[1] Radiological Physics & Advisory Division, Bhabha Atomic Research Centre, Mumbai-400094, India
[2] Homi Bhabha National Institute, Mumbai-400094, India

E-mail: ni3kakade@gmail.com

OPEN ACCESS

RECEIVED
20 November 2023

REVISED
16 January 2024

ACCEPTED FOR PUBLICATION
24 January 2024

PUBLISHED
7 February 2024

Keywords: dosimetry audit, radiotherapy, anthropomorphic phantom, thermoluminescent dosimeters



## Abstract

The treatment of head and neck (H&N) cancer presents formidable challenges due to the involvement of normal tissue and organs at risk (OARs) in the close vicinity. Ensuring the precise administration of the prescribed dose demands prior dose verification. Considering contour irregularity and heterogeneity in the H&N region, an anthropomorphic and heterogeneous H&N phantom was developed and fabricated locally for conducting the dosimetry audit in advanced radiotherapy treatments. This specialized phantom emulates human anatomy and incorporates a removable cylindrical insert housing a C-shaped planning target volume (PTV) alongside key OARs including the spinal cord, oral cavity, and bilateral parotid glands. Acrylonitrile Butadiene Styrene (ABS) was chosen for PTV and parotid fabrication, while Delrin was adopted for spinal cord fabrication. A pivotal feature of this phantom is the incorporation of thermoluminescent dosimeters (TLDs) within the PTV and OARs, enabling the measurement of delivered dose. To execute the dosimetry audit, the phantom, accompanied by dosimeters and comprehensive guidelines, was disseminated to multiple radiotherapy centers. Subsequently, hospital physicists acquired computed tomography (CT) scans to generate treatment plans for phantom irradiation. The treatment planning system (TPS) computed the anticipated dose distribution within the phantom, and post-irradiation TLD readings yielded actual dose measurements. The TPS calculated and TLD measured dose values at most of the locations inside the PTV were found comparable within 4%. The outcomes affirm the suitability of the developed anthropomorphic H&N phantom for precise dosimetry audits of advanced radiotherapy treatments.

## 1. Introduction

Radiotherapy is one of the major modalities for cancer treatment, along with surgery and chemotherapy. Advanced radiotherapy techniques, such as Intensity Modulated Radiation Therapy (IMRT) and Volumetric Modulated Arc Therapy (VMAT), offer the remarkable ability to precisely deliver concentrated doses to tumors while minimizing radiation exposure to critical organs at risk (OARs) and normal tissue [1]. This attribute proves particularly valuable in treating complex clinical sites like the head and neck (H&N), where sensitive structures like parotid glands, spinal cord, and eyes are situated in close proximity to the tumor [2]. The fundamental objective in H&N cancer treatment is to deliver the prescribed dose to the tumor while ensuring minimal radiation exposure to OARs [3]. Customized radiotherapy plans are devised to achieve this dual aim. It's essential that these patient-specific treatment plans are executed with meticulous care. A small error in the treatment procedure can results in large deviation between planned and delivered dose [4]. Hence, for the delivery of precise and accurate dose it is required to perform all the steps in the treatment procedure with great accuracy [5].

The pre-treatment dose verification is an important part to assure accurate delivery of the prescribed dose [6]. This verification method provides an instantaneous verification of dose calculations before the start of a patient's treatment and hence, assures the accurate delivery of the planned treatment. In general, every radiotherapy center performs the pre-treatment

IOP Publishing Biomed. Phys. Eng. Express 10 (2024) 025022 N R Kakade et al

dose verification right before the treatment delivery. Institutional pre-treatment dose verification is basically a self-evaluation which is prone to miss systematic errors that may be involved in the planning, treatment and dose analysis procedures. The methods that are selected for validating advanced radiotherapy treatment plans are rather dependent upon the decision of each institution. Third party dosimetry quality audit (QAu) program is an independent verification and is free from these limitations [7]. The dosimetry QAu procedure is important to assess whether the participating institutes are providing the accurate dose delivery using uniform dosimetry methodology mentioned in the international protocols [8].

To ensure accurate dosimetric verification, an ideal phantom must replicate the tumor site with realism and encompass heterogeneous structures in its vicinity [9]. Such phantoms are vital for the commissioning and clinical implementation of IMRT and VMAT for specific clinical scenarios. The materials used for fabrication must closely resemble human tissue in terms of scattering and attenuation. Although air-filled ionization chambers, electronic portal imaging devices, ion chamber arrays, and liquid ion chambers are commonly employed for pre-treatment dose verification [10], remote dosimetry QAu programs typically favor passive dosimeters such as thermoluminescent dosimeters (TLDs) and radiochromic films [11]. Thus, the phantom should be designed to accommodate these dosimeters within the planning target volume (PTV) and OARs. In line with these requisites, an indigenous anthropomorphic and heterogeneous H&N phantom was conceived and developed. This study aims to explore the feasibility of utilizing this phantom for dosimetry QAu of advanced radiotherapy techniques, namely IMRT and VMAT.

## 2. Design and development of anthropomorphic H&N phantom

An anthropomorphic and heterogeneous head and neck (H&N) phantom, devised for dosimetry QAu purposes, was meticulously designed and developed, taking into account the following salient considerations:

a. **Representative Patient Size:** The phantom's dimensions were tailored to closely resemble the average dimensions of a typical H&N patient.

b. **Material Properties:** Materials chosen for fabrication were not only non-toxic but also possessed structural integrity for seamless transportation.

c. **Anatomical Fidelity:** The design was meticulously crafted to mirror anatomical accuracy, ensuring conformity with internal geometries.

d. **Material Properties Resembling Human Tissue:** The selected materials were required to closely mimic the radiological and physical characteristics of the actual relevant tissues.

e. **Structural Differentiation:** Visual distinction of neighbouring structures was incorporated to facilitate accurate delineation in the treatment planning system.

f. **Ease of Assembly and Disassembly:** User-friendly assembly and disassembly mechanisms were integrated into the design.

g. **Geometrical Repositioning Facilitation:** The phantom incorporated tools to simplify geometrical repositioning.

h. **Provision for Different Dosimeters:** The phantom was equipped to accommodate a range of dosimeters, facilitating comparative analyses.

i. **Appropriate Weight:** The weight was optimized for easy handling and transportation.

The dimensions of the H&N phantom including PTV and OARs were established based on averaged dimensions extracted from ten nasopharyngeal cancer patients. However, the final shapes were simplified in order to ease the manufacturing procedure. The different parts of the phantom such as phantom body, PTV insert and OAR inserts were fabricated from the blocks of requisite material. These blocks were shaped as per the planned design using cutting tools, such as CNC machine. The different parts of phantom were assembled and joined together using ABS-compatible bonding material to form the final structure of H&N phantom. The developed phantom is made up of body structure accurately emulating the general contours of the human H&N region. Within this body, a detachable cylindrical insert measuring 10 cm in diameter and 15 cm in length can be introduced. This removable insert encompasses a C-shaped PTV and assorted OARs, including the spinal cord, oral cavity, and bilateral parotid glands. The PTV assumes a C-shaped configuration with a diameter of 4.5 cm and a length of 7.5 cm. Correspondingly, the various OARs, such as the spinal cord, left parotid, right parotid, and oral cavity, are modeled as cylindrical structures measuring 2 cm in diameter and 7.5 cm in length. For illustrative purposes, figure 1 shows a photograph of the developed H&N phantom alongside the removable insert housing the PTV and OARs.

The selection of materials for the fabrication of distinct phantom components was determined by the radiological properties of the tumor and OARs within the H&N region. Acryline Butadiene Styrene [(C8H8·C4H6·C3H3N)n] (ABS) is a copolymer made by polymerizing acrylonitrile and styrene in the presence of polybutadiene. The composition of ABS is: Acrylonitrile (15 to 35%); Butadiene (5 to 30%) and Styrene (40 to 60%). An ABS plastic being a tissue equivalent material was used in the fabrication of PTV

8

IOP Publishing Phys. Scr. 99 (2024) 065923 https://doi.org/10.1088/1402-4896/ad3b4e

Physica Scripta

PAPER

# Effect of porosity on deuterium retention in titanium thin film

**Basanta Kumar Das**[1,*], **Rashmita Das**[1], **C Prathap**[2], **Rishi Verma**[1,3] **and Archana Sharma**[1,3]

[1] Pulse Power and Electromagnetic Division, Bhabha Atomic Research Centre, Atchutapuram, Visakhapatnam, -531011, India
[2] Atomic and Molecular Physics Division, Bhabha Atomic Research Centre, Atchutapuram, Visakhapatnam, -531011, India
[3] Homi Bhabha National Institute, Anushaktinagar, Mumbai, -400094, India
[*] Author to whom any correspondence should be addressed.

**E-mail:** basanta@barc.gov.in **and** dasbabu31@gmail.com

**Keywords:** deuterium diffusion, deuterated target, gettering, thermal desorption, SEM, RGA, XRD

**OPEN ACCESS**

**RECEIVED**
7 December 2023

**REVISED**
29 March 2024

**ACCEPTED FOR PUBLICATION**
5 April 2024

**PUBLISHED**
6 May 2024



## Abstract

The absorption process of deuterium in titanium was studied in titanium film produced in two different types of copper substrate, one was a polished copper substrate and the other one was chemically etched copper substrate. Titanium film was produced by thermal evaporation method. It was activated at a temperature of 500 °C followed by deuteration at room temperature. Titanium film was characterized by XRD for crystallographic information, SEM for surface morphology, RGA for deuterium desorption studies and weight measurement for D/Ti ratio. The difference in porosity of both the samples is confirmed from XRD analysis and SEM images. Different diffusion process is observed in two different substrates from the RGA spectra. Presence of multiple trap sites in the thin film of both the substrates is observed from the RGA spectra. From the weight measurement, D/Ti ratio in polished substrate is found to be 1.03 whereas in case of chemically etched substrate it is 1.54.

## 1. Introduction

Solid deuterated targets are used in accelerator based neutron generators for generation of neutrons [1–3]. Quantity of deuterium in the solid target is one of the important factors for high yield of neutrons. These targets are usually made up of titanium thin film coated on copper substrate. Group IV and V elements of the periodic table have a distinct property to retain deuterium at room temperature through a process called gettering [4]. Titanium being group IV element of periodic table has the property of gettering. Gettering is a process in which deuterium absorption takes place in three step processes. First the deuterium molecule is adsorbed after dissociation at the surface of the titanium film, then the dissociated atom penetrates to the near surface region of the film and at the end, diffuses into the bulk of the film. The quantity of deuterium diffused in the titanium thin film depends upon the deuterium concentration at the surface, temperature of substrate,voids, defects, grain size and grain boundary in the titanium thin film. The deuterium concentration at the near surface region depends up on the concentration of deuterium adsorbed at the surface after dissociation. The dissociative adsorption at the surface depends on the dissociation energy, sticking probability, surface area and surface temperature whereas penetration in to the near surface region depends on voids, grain size and grain boundaries in the thin film and concentration gradient of deuterium. Required dissociation energy can be provided either by charging the film at higher deuterium pressure or heating the surface. The effect of higher pressure for higher retention of deuterium in titanium thin film is experimentally demonstrated in [5]. Surface morphology plays an important role for absorption of deuterium in the titanium thin film. Effective surface area of the titanium thin film increases with roughness of the film. If the substrate surface area is rough, the film produced on this rough surface also carries the roughness while coating. Effective surface area increases with repetitive peak and valley formation on the film. With increased surface area, the probability of interaction of deuterium molecule with surface increases and this leads to higher rate of adsorption of deuterium.

The molecules at bulk of a solid experience zero resultant force due to the surrounding molecules. But the molecule at the surface experiences a force towards the bulk of the solid. Thus a surface tension is created. Hence the molecule at the surface has affinity to adsorb gas molecules to reduce the resultant force. The van der Waals force is involved in the interaction of a gas with a solid and this physical process is known as physisorption. In physisorption,

at the equilibrium of charge distribution there is no sharing or transfer of electrons takes place. In this case the properties of adsorbent and adsorbate do not change. The interaction which involves exchange of electrons is known as chemisorption and in this process the properties of the adsorbent and the adsorbate change. The Lennard-Jones potential function [6, 7] as mentioned below describes the process of physisorption.

$$\phi(r) = 4\varepsilon\left[\left(\frac{\sigma}{r}\right)^{12} - \left(\frac{\sigma}{r}\right)^{6}\right] \quad (1)$$

Where ε is the depth of the potential well, $\sigma$ is the distance at which the inter particle potential is zero and r is the distance between the particles. The first term in above equation $\left(\frac{\sigma}{r}\right)^{12}$ is the Pauli repulsion at short ranges whereas the second term $\left(\frac{\sigma}{r}\right)^{6}$ is the van der Waals force at long ranges. The exponents used in this equation can be modified for different surface conditions. For interaction of gas molecules with flat surface the exponents would be 10 and 4 whereas for the interaction of gas molecules and pores it would be 9 and 3 respectively. Depending on the equation (1) above, plots have been shown for Lennard-Jones potential function versus the pore size [7]. It is demonstrated that the pores with smaller size have enhanced interactions of the gas molecule and the atoms of the adsorbent.

The van der Waals forces between gas molecules and the flat surface or porous surface is described in [8]. The adsorption mechanism between gas molecules and a flat surface is not significant. In this case the gas molecules are partially interactive with surface atoms from one side. In case of porous surface the gas molecule to be adsorbed is surrounded by atoms of the adsorbent. Due to additive properties of van der Waals force, the gas molecule inside the pore, capillary, crack or cavities is surrounded by many neighbouring atoms of the adsorbent. When a molecule is adsorbed, it executes attractive force and contributes to the adsorption energy, so further adsorption takes place. From the theory, it is assumed that the adsorption of gases would be better in porous surface rather than in the flat surface. Better adsorption leads to better penetration of gaseous atoms into the near surface region which leads to better diffusion due to building up of higher concentration gradient of deuterium. Because of this reason the porous surface of the adsorbent could be used for higher absorption of gases. A gas molecule goes through three different processes before adsorption on a solid surface. These are free gas diffusion, Knudsen diffusion and surface diffusion [9]. The porous surface favours the Knudsen diffusion. When the mean free path of the gas molecules is higher than the dimension of the pore, the gas molecule collides more frequently with the wall of the pore rather than with each other. So probability of getting adsorbed for the gas molecule increases.

In this work, a comparative study was carried out for retention of deuterium in uniformly flat titanium thin film and porous titanium thin film on copper substrate. Porosity is observed by the micrograph of the thin film and crystallographic measurements by the x-ray diffraction. Effect of porosity on the diffusion of deuterium in titanium thin film is observed by residual gas analyzer. Quantitative measurement of the deuterium retention in porous as well as flat surfaced samples is done by measuring the mass of deuterium absorbed in the sample. Experimental details and results are described in the following sections.

## 2. Methods and materials

Titanium thin films were prepared on two types of copper substrates; mechanically polished and chemically etched by thermal evaporation method. Copper substrate of 30 mm diameter and 1 mm thick was used. Mechanical polishing of the sample was done in the automatic grinding/polishing machine made by Metatech Industries with model no. Autopol-II. Polishing of the sample was carried out on the emery with varying grit sizes from 200 up to 1500 followed by diamond polishing. Diamond polishing was carried out with diamond particle sizes of 1 and 0.25 $\mu$m subsequently. Chemical etching was performed in aqueous solution consisting of ammonium hydroxide $NH_4OH$ 50% in volume, hydrogen peroxide ($H_2O_2$) 3% in volume, and distilled water 47% in volume. Chemical attack was performed at room temperature for 20 min with a quick stirring of the solution [10]. The etched copper substrate was coated with titanium by thermal evaporation method in a vacuum system described in earlier work [5]. Titanium wire of 0.5 mm diameter was heated to its vaporization temperature in a tungsten spiral coil in a vacuum system pumped by turbo molecular pump. Coating was carried out at a vacuum of the order of $10^{-7}$ mbar. During coating, one interesting event was observed; instead of pressure rise, vacuum improved. As the titanium vapors were coated throughout the chamber, the vacuum during evaporation was improved to the order of $10^{-8}$ mbar. This was due to the fact that when the titanium film was coated on the chamber wall the freshly coated surface pumped the residual gases by gettering. The thickness of the film was estimated volumetrically as 2 micron by weight difference method. The weight of the substrate before and after coating was measured by precision microbalance. Coating thickness depends on evaporation rate which is decided by the current in the tungsten spiral coil. In our case the current in the coil was 85 A which

9

A Letters Journal Exploring the Frontiers of Physics

August 2024

EPL, **147** (2024) 35003
doi: 10.1209/0295-5075/ad5e1c

www.epljournal.org

# Enhanced optical pumping using mutually orthogonal magnetic fields for quantum sensing

Sudip Mandal[1], Raghwinder Singh Grewal[2] and Swarupananda Pradhan[1,3(a)]

[1] *Photonics and Quantum Optics Section, Atomic and Molecular Physics Division, Bhabha Atomic Research Centre Facility - Visakhapatnam-531011, India*
[2] *Division of Mathematical and Physical Sciences, School of Arts and Sciences, Ahmedabad University Commerce Six Roads, Navrangpura, Ahmedabad-380009, India*
[3] *Homi Bhabha National Institute, Department of Atomic Energy - Mumbai-400094, India*

received 22 April 2024; accepted in final form 2 July 2024
published online 22 August 2024

**Abstract** – The atomic population trapped in irrelevant atomic states is a limiting factor for sensors based on laser-atom interaction. Using a bi-chromatic light field along with a specific combination of magnetic fields, we show a significant increase in the amplitude (*i.e.*, more than seven times) of a two-photon coherent population trapping (CPT) resonance, which can be effectively used for atomic magnetometry. This increase in amplitude can be explained through enhanced optical pumping via the transfer of population to the relevant Zeeman states. Our experimental observations are consistent with the theoretical calculations carried out for a realistic three-level atomic system using density matrix formalism. We further discuss the optimum condition for enhanced optical pumping by adjusting the ground-state decoherence rate. Enhanced optical pumping through the manipulation of the magnetic field is quite important and is of great interest in the field of quantum technology.



The efficient quantum state engineering is the basis of many atom-based quantum technologies, such as quantum computation, quantum sensors, and quantum communication [1–3]. The pursued methodology has been instrumental in testing fundamental principles of physics, and the underlying processes have unleashed new avenues of research in different areas [4–6]. The optical pumping of the atoms to a desired atomic state using the light field has been a widely used tool since its inception for functioning/improving the performance of atomic devices [7]. Generally, the performance of an atomic device scales as [8]

$$\frac{1}{\sqrt{NTt}}, \tag{1}$$

where the term $T$ is transverse relaxation time, $t$ is measurement time, and $N$ is the fraction of atoms contributing to the signal. In an ideal situation, the $N$ is desired to be the total number of atoms. However, the partial spectral overlap of the light field with the atomic ensemble and the atomic population in irrelevant states limits $N$. This partial overlap can be an issue while working with anti-relaxation-coated cells where a narrow linewidth laser can only couple with atoms of a particular velocity group. For a buffer gas-filled cell, most of the atoms can be coupled to the light field as the collisional homogeneous width is typically larger than the inhomogeneous Doppler broadening.

However, the atoms in the irrelevant states are a concern for both anti-relaxation-coated and buffer gas-filled cells. Hence, developing a suitable methodology to access these remaining atoms (not contributing to producing resonance signals) is quite important for efficiently working the atomic devices. In many instances, a repump laser is used to populate the desired atomic level [9,10], which effectively increases the amplitude of the resonance signal. However, it brings additional complexities and has a limited role in populating desired Zeeman states of the atomic level.

On the other hand, the coherent population trapping (CPT) based systems are immune to any population loss

(a)E-mail: spradhan@barc.gov.in (corresponding author)

as both hyperfine ground states of an atom are simultaneously coupled to a common excited-state using a bi-chromatic laser field [5,11–14]. In these systems, the amplitude of the CPT resonances is optimized by transferring the population to the desired Zeeman sublevels via manipulating the laser polarization and the direction of the applied magnetic field [15,16]. For example, Cox *et al.* [14] showed the possibility of building a vector magnetometer by measuring the relative amplitude of multiple CPT resonances at different magnetic field orientations using a linearly polarized bichromatic laser field. Similarly, several other groups have used the two-photon CPT resonances to build scalar atomic magnetometers to measure a longitudinal magnetic field applied parallel to the light propagation direction [5,17–20]. Careful application of an orthogonal magnetic field (*i.e.*, perpendicular to the light propagation direction) along with a longitudinal magnetic field can lead to very interesting population dynamics among ground-state Zeeman sublevels of a CPT-based system, and its implementation for enhanced magnetometry has not been explored in the past.

In this article, we show the efficient accumulation of population in relevant Zeeman states by using a circularly polarized bi-chromatic light field in combination with longitudinal and orthogonal magnetic fields. The prolonged interaction of the atoms with the light field in buffer gas is used to its advantage of rapid optical pumping. But most importantly, the Zeeman sublevels with the maximum population contribute to the form desired CPT resonance, resulting in a phenomenal increase in its amplitude (around 7-fold) under this combined action. This amplitude increase will help in improving the sensitivity for the magnetic field measurement. In addition, the envisaged methodology is suitable for the compact operation of the device [21].

The paper is organized with a brief description of the experimental apparatus. The amplitude of the CPT resonances for various combinations of the longitudinal and transverse magnetic fields is shown. A discussion on the utilized theoretical framework based on the semi-classical density matrix approach is presented. A comparison between the experimental and calculated signal profile with a reason for the deviation is discussed. The underlying physical process leading to enhanced optical pumping is described. In addition, we have discussed the role of Rabi frequency and ground-state relaxation rate in optimizing the strength of the CPT resonance.

Figure 1 shows the schematics of the experimental setup and the relevant atomic energy level used to produce the coherent population trapping (CPT) resonances with a bi-chromatic light. The experiment is performed on rubidium (Rb) atoms (natural isotopic composition) with $N_2$ gas at 25 torr in a glass cell (50 mm length and 25 mm diameter) at 48 °C. The vapor cell is mounted at the center of a four-layer magnetic shield, which is used to reduce the ambient magnetic field. A three-axis Helmholtz coils setup was installed inside the shield to apply bias

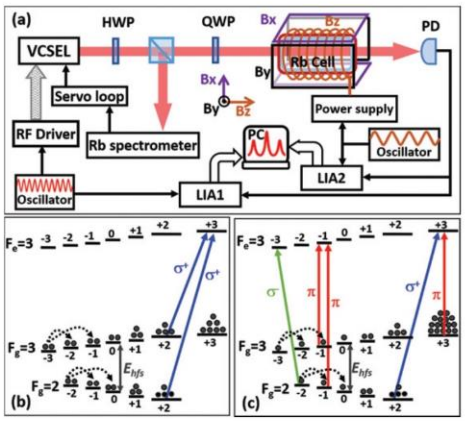


Fig. 1: (a) Schematic diagram showing essential components of the experimental setup. Energy level diagram showing (b) the $\sigma^+$ transitions in the presence of longitudinal magnetic field $B_z$, and in (c), the $\sigma^+$ and $\pi$ transitions when both $B_z \neq 0$, $B_y \neq 0$. The stretched CPT resonance is formed by ($|F_g = 2, m_F = +2\rangle$, $|F_g = 3, m_F = +3\rangle$) coupled with blue and red solid lines. The green $\sigma^-$ arrow also participate in many CPT manifolds but it is not shown due its feeble strength.

magnetic fields in all three directions. A Vertical Cavity Surface Emitting Laser (VCSEL) at 795 nm, 60 $\mu$W power with beam diameter 4.5 mm is frequency modulated by a radio frequency (RF) oscillator at 1.517866 GHz to generate sideband beams resonant from both ground states of $^{85}$Rb to a common excited state $F_e = 3$ in D1 line. The RF oscillator is modulated at a frequency 440 Hz with a modulation of depth of 12 kHz. We consider the propagation direction of the laser beam along the $z$-axis. Using a quarter wave plate (QWP) before the vapor cell, the light polarization is set to circular. The light transmitted through the atomic sample is demodulated using a lock-in amplifier (LIA1) at the modulation frequency applied to the RF oscillator. Two-photon CPT resonances are observed by scanning the RF oscillator as the frequency difference ($\Delta\omega$) between the side mode of the laser beam matches with the separation between the ground Zeeman states ($E_{hfs}$) that are simultaneously coupled to an excited level Zeeman state of $^{85}$Rb, as shown in fig. 1(b). Multiple $\Lambda$-systems are formed at different values of two-photon detuning defined as $\Delta = \Delta\omega - E_{hfs}$. Consequently, the magnetic field insensitive clock transition is observed at $\Delta = 0$ and magnetic field sensitive transitions at $\Delta \neq 0$.

We consider the propagation direction of the light field as the axis of quantization (*i.e.*, $z$-axis). The degeneracy in the hyperfine Zeeman sublevels is lifted by applying a longitudinal magnetic field $B_z$. Since the laser beam is circularly polarized, only $\sigma^+$ transitions are possible in the presence of $B_z$ field (fig. 1(b)). The presence of any orthogonal magnetic field ($B_x$ or $B_y$) leads to population redistribution among the Zeeman states, which can

10

IOP Publishing J. Radiol. Prot. 44 (2024) 041512 https://doi.org/10.1088/1361-6498/ad8fb8

Journal of Radiological Protection

PAPER

# Estimation and analysis of S values for $^{131}$I using paediatric mesh type reference computational phantoms

**Pradeep Kumar Singh*, Hemant Kumar Patni, Deepak Kumar Akar and Pramilla D Sawant**

Internal Dosimetry Section, Radiation Safety Systems Division, Bhabha Atomic Research Centre, Mumbai 400085, India

* Author to whom any correspondence should be addressed.

**E-mail:** pradeepsingh@barc.gov.in

**Keywords:** paediatric mesh phantoms, Geant4, *S* values, $^{131}$I

Supplementary material for this article is available online

OPEN ACCESS

RECEIVED
9 September 2024

REVISED
1 November 2024

ACCEPTED FOR PUBLICATION
7 November 2024

PUBLISHED
25 November 2024



## Abstract

This study examines the effect of paediatric mesh-type reference computational phantoms on organ *S* values resulting from radioiodine ($^{131}$I) intake. Using Geant4, we estimated $^{131}$I *S* values for 30 radiosensitive target tissues due to emission from the thyroid (Target ← Thyroid) in these phantoms. Our results show that *S* values differ between male and female phantoms of the same age and *S* values also decrease as phantom age increases. The male-to-female *S* value ratio typically varies within 10%, with larger differences observed for the esophagus, extra-thoracic regions, muscles, bladder, and sex organs. On average, *S* values for mesh phantoms are approximately 17% higher than those for voxel phantoms, with larger discrepancies for organs remodelled separately in mesh phantoms. The study provides organ *S* values for the paediatric population due to $^{131}$I exposure from the thyroid, based on the reference mesh-type computational phantoms, enhancing organ dose estimation in emergency situations and during radioiodine treatment.

## 1. Introduction

Radioiodine ($^{131}$I) is a widely used radiopharmaceutical for treating thyroid cancer and other thyroid disorders across all age groups. Its thyroid seeking property and high energy electron emission ($E_{max} = 606$ keV) makes it particularly effective in delivering the required dose to the thyroid gland while minimizing exposure to other organs and tissues [1]. However, this benefit of radioiodine treatment comes with the disadvantage of high-energy gamma emissions ($E = 364$ keV), which results in an unwanted dose to organs/tissues other than the thyroid. Previous studies suggest that younger age groups are more susceptible to the radiation dose for a given amount of radioiodine intake [2, 3]. Therefore, it is essential to assess the radiation dose delivered to organs other than the thyroid for these age groups.

The dose coefficient (DC) for an internally deposited radionuclide is estimated using two factors: (1) its biokinetic model, which provides the time-integrated activity in source regions and (2) the *S* values, defined as the mean absorbed dose in target regions per unit disintegration of radionuclide in the source region [4]. The absorbed dose is estimated by Monte Carlo simulations performed with computational phantoms, specifically designed for dosimetric purposes. From Medical Internal Radiation Dose stylized phantoms (1st Generation) to mesh-type phantoms (4th Generation), there has been significant evolution in terms of scientific methodology and computational power used in phantom development [5]. The voxel phantoms (3rd Generation) released by the International Commission on Radiological Protection (ICRP) [6, 7], based on 3D-CT scans and MRI images of real individuals, have gained popularity due to their detailed representation of human anatomy and enhanced accuracy in radiation dose calculations. Despite having millions of voxels to represent whole-body organs, even these phantoms have limitations in representing micron-scale organs such as those in the skin, eye lens, urinary bladder, alimentary tract, and respiratory tract [6, 7]. As a result, alternative surrogate geometries have been employed for calculating absorbed doses

IOP Publishing J. Radiol. Prot. 44 (2024) 041512 P K Singh et al

in these tissues [8, 9]. In view of these limitations, the replacement of voxel phantoms with more advanced computational phantoms is long overdue.

Addressing these limitations, the ICRP Task Group 103 first developed Polygon Mesh (PM) adult computational phantoms by converting adult reference voxel phantoms into high-quality mesh formats, using 3D surface rendering and refinement procedures [5]. These phantoms offer notable advantages, enabling the representation of even the smallest tissues using mesh modelling. The importance of mesh phantoms has been demonstrated in various studies focusing on their dosimetric applications and ability to deform. For instance, Yeom *et al* investigated the influence of thyroid location on iodine *S* values [10] and developed a comprehensive dataset of body-size-dependent $^{131}$I *S* values [11]. In other studies, they estimated DCs due to external exposure of neutrons, protons, and helium ions [12] as well as due to electrons and photons [13]. While the DCs for most organs and the effective dose were found to be similar to those derived from voxel-based models, considerable differences were observed for low-energy electrons, particularly in smaller organs/tissues and skeletal tissues, due to the improved representation of organs in mesh-type phantoms [12, 13].

Following the same trend, ICRP Task Group 103 has recently developed a series of 10 paediatric mesh-type reference computational phantoms (PMRCPs), representing various age groups viz. newborn (00), 1-year-old (01), 5-year-old (05), 10-year-old (10), and 15-year-old (15) for both genders (male (M) and female (F)), addressing the limitations of their predecessors, the paediatric voxel-type reference computational phantoms (PVRCPs) [14]. PMRCPs have been used to estimate DCs due to idealized external exposure. The DCs are found to be similar to PVRCPs for most organs and energies. However, considerable differences have been observed for low-energy electrons and some specific organs [14]. Given these differences in DCs for external exposure, it is necessary to investigate the effects in internal exposure scenarios as well.

In this study, we estimate *S* values for 30 radiosensitive target tissues of PMRCPs, resulting from radioiodine decay in the thyroid. Additionally, we investigated the influence of paediatric mesh phantoms on organ doses by comparing them to voxel-model-based values reported in a previous study [15]. The *S* values provided in this study are based on reference mesh-type computational phantoms and will be beneficial for evaluating organ doses in paediatric populations in cases of radioiodine intake, in both medical and emergency scenarios.

## 2. Materials and method

### 2.1. PMRCPs and Monte Carlo simulation

A detailed procedure for the development of PMRCPs is outlined in the work of Choi *et al* [14]. Few specific aspects are discussed in this paragraph. The PM models for the organs of the PMRCPs were derived by converting PVRCPs (ICRP Publication 143) and the paediatric phantom series from the University of Florida and the National Cancer Institute into high-resolution mesh formats using 3D surface rendering and refinement techniques [7, 14, 16]. While the reference paediatric mesh and voxel phantoms exhibit general similarities, subtle differences have emerged due to adjustments made in the mesh phantoms. These adjustments include the incorporation of organ blood content based on the regional blood volume listed in table 7 from Wayson *et al* [17], slight differences in the organ masses between genders of the same age [18], and the incorporation of detailed geometries for micron-layered organs [19, 20]. These factors have also led to noticeable variations in the relative positioning of organs and slight variations in the organ masses between male and female mesh phantoms of the same age. These developed PM models have also been converted into tetrahedral-mesh (TM) format for improved computational efficiency and compatibility with various Monte Carlo codes [21, 22].

In this study, Monte Carlo particle transport simulations are performed in Geant4 (Geometry And Tracking), an open source simulation toolkit [23]. The TM models of PMRCPs were incorporated into Geant4 using the *G4Tet* class with a parameterization approach [21, 24]. $^{131}$I was assumed to be uniformly distributed in the thyroid, and its radioactive decay was simulated using *G4UserPrimaryGenerationAction* by setting the particle definition to ion. A complete $^{131}$I decay spectrum was used during the simulation based on Evaluated Nuclear Structure Data maintained by the National Nuclear Data Centre [25]. Electron and photon transport simulations were achieved using the *G4EmLivermorePhysics*. Uniform random points were generated within the thyroid by employing a rejection technique: initially, random points were generated within the bounding box of the thyroid, and then, out of these, points falling outside the tetrahedral mesh of the thyroid were rejected based on the provided organ ID during the simulation. A total of $5.0 \times 10^8$ primary particles were simulated for each phantom to minimize the simulation error. The simulations were performed on Intel Xeon, W-2295 (18 cores) workstation in multi-thread mode. Figure 1 shows the implementation of male PMRCPs in Geant4.

11

OPEN ACCESS
IOP Publishing
Journal of Physics B: Atomic, Molecular and Optical Physics
J. Phys. B: At. Mol. Opt. Phys. **57** (2024) 215701 (13pp)
https://doi.org/10.1088/1361-6455/ad7943

# Exploring the influence of plasma temperature on the evolution of boron molecular species in laser-induced plasma

**Anandhu Mohan**[1], **Anannya Banerjee**[2] and **Arnab Sarkar**[1,2,*]

[1] Homi Bhabha National Institute, Anushakti Nagar, Mumbai 400 094, India
[2] Fuel Chemistry Division, Bhabha Atomic Research Centre, Mumbai 400 085, India

E-mail: arnab@barc.gov.in and asarkar@ymail.com

Received 1 April 2024, revised 16 August 2024
Accepted for publication 10 September 2024
Published 26 September 2024

**Abstract**

The impact of plasma temperature on the formation and evolution of distinct and unique molecular species recorded as molecular signatures from laser induced plasma (LIP) was examined in this study. A definitive correlation between plasma temperature and the formation of molecular species has been established through a comprehensive temporal analysis of BO and $BO_2$ molecular bands. The utilization of the signal-to-envelope ratio diagrams allowed for pinpointing the optimal temperature range for molecule emission. Notably, the molecule BO exhibited an ideal temperature range of 10,000–11,000 K for the proper formation of molecular emission bands, while $BO_2$ preferred temperatures between 8,000–9,000 K. These optimal temperature ranges remained consistent regardless of the laser irradiation wavelength or ambient gas conditions of Ar, air or He studied in this work. These key findings highlight the significant influence of plasma temperature in shaping the molecular species observed in LIP.

Keywords: LIP, molecular spectra, temporal evolution, plasma temperature, BO, $BO_2$

## 1. Introduction

The study of emission signatures from a laser-induced plasma (LIP), particularly the evolution of molecular emission signatures, is a fascinating and intricate tool that helps to explore the complexities of sample matrix [1, 2]. In the past few decades, the laser spectroscopy community has been utilizing molecular emission signatures in LIP for various qualitative and quantitative applications [3–7]. The increased interest is mainly driven by the valuable information offered by molecular species, a characteristic feature absents in atomic emission lines. This is evident in the detection of isotopes, halogens, and actinides, among other elements, [8–10]. In this scenario, a thorough understanding of the evolution dynamics of molecular emission signatures and the factors affecting them is of paramount significance.

The plasma electronic temperature ($T_e$), a key parameter in this process, plays a pivotal role in determining the behavior of molecules within the plasma. As the temperature rises, the molecular species present in the sample undergo various transformations, including dissociation, ionization, and excitation. These processes give rise to distinctive emission signatures, which can be probed and analyzed to gain insights into the sample's composition and the underlying physical and chemical phenomena [11, 12]. Previous studies already identified a relationship between plasma temperature and the formation of molecular species. Bai *et al* discovered a maximum plasma

* Author to whom any correspondence should be addressed.

temperature range for the optimum analysis of Al lines without any interference caused by oxide formation (AlO) [13]. A previously conducted study from our group already noticed the influence of plasma temperature in the formation of molecular emission of (0–2) B–X band of BO molecule [14]. Baudelet *et al* showed that the lower plasma temperature reduces the interferences from ambient air in the analysis of CN and $C_2$ molecular emission [15]. To the best of our knowledge till date, no comprehensive study is available for a thorough understanding of the relationship between plasma temperature and molecular species evolution, and this demands an in-depth insight into the situation.

This study focuses on untying the unexplored knot of the influence of plasma temperature in the evolution of molecular species and opens a gateway to understanding the proper idea behind the optimization of the parameters. Given the broad applicability of boron isotopic composition information in fields like geochemistry [16, 17], cosmological studies [18, 19], nuclear industry [20, 21], and environmental sciences [22, 23], our group has investigated the use of BO molecular emission signatures for isotopic composition determination [14]. We have also studied the temporal evolution of transient molecular species, including BO and $BO_2$ [24]. The dependency of molecular species on $T_e$ in LIP was analyzed using three different laser irradiation wavelengths: 1064 nm (IR), 532 nm (VIS), and 266 nm (UV). Furthermore, the relationship between $T_e$ and the molecular information was explained using signal-to-envelope ratio (SER) under different laser irradiation wavelengths and different ambient gas atmosphere conditions of helium (He), air, and argon (Ar).

## 2. Experimental setup

Previous study [24] provides a comprehensive overview of the experimental setup. In brief, the ablation source was a Q-switched Nd:YAG laser (Brilliant B, Quantel) which underwent reflection through mirrors (Thorlabs, NB1-K13) before passing through a biconvex focusing lens ($f = 15$ mm, MH-10X-532, Thorlabs). An indigenously developed collimator was used for the collection of emitted light from the plasma. The sample was positioned on a computer-controlled *XYZ* translation stage to enable precise spatial control during analysis. Light collected by the collimator was then delivered to the spectrograph using an optical fiber bundle (SR-OPT-8024, Andor, $D = 200$ $\mu$m) via an F-matcher. The study employed a Czerny–Turner spectrometer (Shamrock SR750, Andor) equipped with mechanical gratings of 1200 grooves $mm^{-1}$ ($\Delta\lambda = 55$ pm, bandpass $\sim$13 nm) and 2400 grooves $mm^{-1}$ ($\Delta\lambda = 25$ pm, bandpass $\sim$6 nm). Molecular emission lines were detected and recorded using an iCCD camera (iStar DH334T-18F-03, Andor, 1024 $\times$ 1024 pixels). The experiment was conducted for various laser wavelengths obtained using second (532 nm) and fourth (256 nm) harmonic generation setup.

Boron sample pellets required for the analysis were prepared using natural boric acid crystalline powder (Chemco Fine Chemicals, purity: 99.5%). To prepare the pellet, a pressure of 5 tons was applied on approximately 1 gm of sample powder taken in a 10 mm dye for 2 min. For the plasma temperature analysis, 0.1% ferrous oxide (FeO) was added to the boric acid powder and thoroughly mixed for the preparation of pellets. Spectral data was collected by accumulating 200 single-shot laser ablation spectra in digging mode under three ambient gas atmospheric conditions (He, air and Ar), with each new spectrum obtained by ablating a fresh surface.

For the analysis of the temporal evolution of molecular bands, spectra were recorded while maintaining a gate width ($t_w$) same as that of acquisition delay time ($t_d$). Before analysis, the recorded spectra were normalized for $t_w$. The algorithms used for spectral analysis were developed using the LabVIEW platform (LabVIEW 2020, National Instruments).

## 3. Result and discussion

### 3.1. Influence of laser wavelength

Previous temporal analyses have revealed that the rate of temporal intensity decay remains consistent regardless of the ro-vibrational transition occurring within an electronic transition [24]. Therefore in this study, one representative ro-vibrational band (RVB) is selected from each transition viz., (1–1) band of BO:A–X, (0–2) band of BO:B–X, and (300–000) band of $BO_2$:A–X. The temporal decay of these representative RVBs was analyzed for different laser irradiation wavelengths by maintaining a constant irradiance of $\sim 1.3 \times 10^{11}$ W $cm^{-2}$. The temporal spectral evolution and decay of the above-mentioned three boron molecular bands for different laser wavelengths are given in figures 1–3.

Figure 1 depicts the temporal evolution of the (0–2) band of BO:B–X transition. The band head appears earliest under UV irradiation, observed at 0.3 $\mu$s onwards. However, the time required for the initial band head appearance in VIS and IR irradiation increases to 0.6 $\mu$s and 1 $\mu$s, respectively. Under UV laser irradiation, the molecular emission signatures are observable up to 5 $\mu$s, after which the RVB signatures disappear. For VIS and IR laser irradiation, the emission timescales increase up to 15 $\mu$s and 40 $\mu$s, respectively, beyond that the RVB structures fade.

In contrast to the BO:B–X transition, a distinct band head is typically not observed with the BO:A–X and $BO_2$:A–X transitions. However, they exhibit a similar trend regarding the timescale for RVB structure formation (figures 2 and 3). Under UV irradiation, BO:A–X RVBs appear around 0.3 $\mu$s and persist up to 10 $\mu$s. Consistent with prior observations, the timescale for RVB formation increases for VIS laser irradiation (1 $\mu$s to 30 $\mu$s) and further extends under IR irradiation (2 $\mu$s to 65 $\mu$s). The $BO_2$:A–X RVBs also display a similar dependence on the laser irradiation wavelength. Well-defined molecular emissions appear from approximately 0.6 $\mu$s and persist up to 8 $\mu$s under UV-irradiation. VIS laser irradiation leads to a delayed onset of RVB formation, with initial emissions observed around 1 $\mu$s and well-developed structures emerging by 3 $\mu$s. These molecular emissions are detectable up to 16 $\mu$s.

12

IOP Publishing J. Radiol. Prot. 44 (2024) 011510 https://doi.org/10.1088/1361-6498/ad270c

Journal of Radiological Protection

PAPER

# Exploring the role of large language models in radiation emergency response

**Anirudh Chandra**[1,*] and **Abinash Chakraborty**[2]

[1] Radiation Safety Systems Division, Bhabha Atomic Research Centre, Mumbai 400085, India
[2] Health Physics Division, Bhabha Atomic Research Centre, Mumbai 400085, India
[*] Author to whom any correspondence should be addressed.

**E-mail:** anirudh.chandra@outlook.com

**Keywords:** large language models, ChatGPT, radiation emergency, emergency response, disaster management

OPEN ACCESS

RECEIVED
19 December 2023

REVISED
8 January 2024

ACCEPTED FOR PUBLICATION
7 February 2024

PUBLISHED
15 February 2024



## Abstract

In recent times, the field of artificial intelligence (AI) has been transformed by the introduction of large language models (LLMs). These models, popularized by OpenAI's GPT-3, have demonstrated the emergent capabilities of AI in comprehending and producing text resembling human language, which has helped them transform several industries. But its role has yet to be explored in the nuclear industry, specifically in managing radiation emergencies. The present work explores LLMs' contextual awareness, natural language interaction, and their capacity to comprehend diverse queries in a radiation emergency response setting. In this study we identify different user types and their specific LLM use-cases in radiation emergencies. Their possible interactions with ChatGPT, a popular LLM, has also been simulated and preliminary results are presented. Drawing on the insights gained from this exercise and to address concerns of reliability and misinformation, this study advocates for expert guided and domain-specific LLMs trained on radiation safety protocols and historical data. This study aims to guide radiation emergency management practitioners and decision-makers in effectively incorporating LLMs into their decision support framework.

## 1. Introduction

In the recent past, large language models (LLMs) have greatly emerged as transformative tools in various domains. Interest grew especially after the introduction of OpenAI's ChatGPT in November 2022 [1] which saw a frenzy in internet search activity for more information on LLMs (figure 1). This emergence of LLMs, including OpenAI's GPT-4 [2] and Google's PaLM 2 [3], with their intuitive conversational mode of interaction, has witnessed a surge in their utilization across several diverse industries [4] due to their remarkable language generation capabilities and contextual understanding.

But new technologies are often touted as double-edged swords and artificial intelligence (AI) in general and LLMs in particular being no different [5]. On the one hand, their ability to process vast amounts of textual data and generate human-like responses [6, 7] is a potential game-changer in natural language understanding [8], sentiment analysis [9–11], and question-answering tasks [6, 12]. And on the other hand, difficulty in distinguishing between human-written and machine-generated text [13, 14], potential for mass production of misleading and deceitful content [6, 13] and questions of reliability and truthfulness of generated content [13, 15, 16] have raised concerns.

Understanding the two sides of the LLMs becomes especially important when this technology is used in a sensitive domain such as disaster or emergency response in the nuclear and radiological industry. The infamous nuclear accidents at Chernobyl and Fukushima and the recent attacks on the Zaporizhia nuclear power plant in Ukraine have raised apprehensions in the minds of the public about all things radiation. In such an environment, it is critical that a potentially disruptive technology such as LLMs be examined comprehensively on its use by practitioners as well as the lay-person. As far as we know, this paper is the first of its kind to explore the application of LLMs in the domain of radiation emergency response management.

IOP Publishing J. Radiol. Prot. 44 (2024) 011510 A Chandra and A Chakraborty

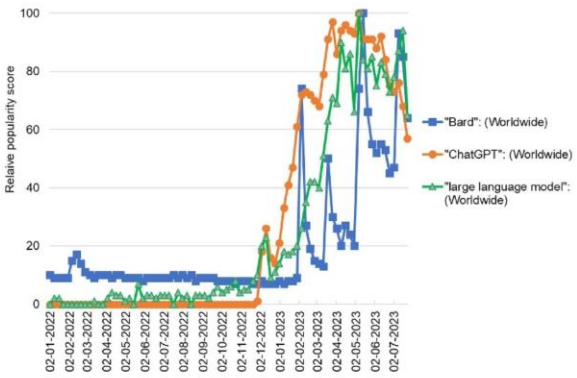


**Figure 1.** Dramatic rise in popularity of keywords 'Bard', 'ChatGPT' and 'large language model' in Google searches from Jan 2022 till July 2023(data source: Google Trends™).

The rest of the paper is structured as follows—sections 2 and 3 introduce the domain of radiation emergency management and traditionally used decision support tools in this domain. The scope of using LLMs as decision support tools is discussed in section 4. Insights on who could be potential users of this application and their use in radiation emergency is explored in sections 5 and 6 respectively. Section 6 also includes preliminary results of a user-ChatGPT simulation exercise. Section 6 also discusses the challenges and precautions to take while using LLMs in radiation emergency management. Appropriate conclusions are drawn in section 7.

## 2. Radiation emergency management

Radiation emergencies[3] or accidents, while relatively infrequent, are challenging events to respond to because they involve dealing with radioactive sources and their potential dispersal, handling of specialised equipment, coordination between different stakeholders and dealing with the public wariness of radiation. The challenge lies in effectively responding in the face of high uncertainty and public fear. Accurate and rapid decision-making in such accidents is critical, and can significantly mitigate the extent of harm incurred.

A radiation emergency can encompass a range of situations, from smaller incidents involving radioactive sources [17] to larger nuclear accidents like a core meltdown in a nuclear reactor [18]. Within this spectrum, various individuals play distinct roles. These roles include victims, first responders, incident commanders, medical doctors, public relations officers, and concerned citizens. Each stakeholder has specific concerns, which vary depending on the scale of the emergency. For instance:

- Victims of acutely high radiation exposure incidents would be worried about any symptoms they may experience;
- First responders would seek guidance on conducting radiation monitoring in hazardous environments;
- Incident commanders would want efficient methods to manage their responding team's radiation exposure;
- Medical doctors would require information on distinguishing radiation sickness symptoms from other diseases;
- Public relations officers would want to convey information without causing unnecessary alarm among the public;
- Concerned citizens would seek comprehensive knowledge about the radiation emergency and the hazards associated with radiation.

These diverse set of participants would look towards any tool that could alleviate their concern and add value to any decision they would make.

Among the experts and practitioners of emergency response management, decision support tools and systems are commonly employed to address their concerns during and after disasters [19]. These tools serve

[3] Radiation emergency is an umbrella term that includes nuclear emergency (involving nuclear material) and radiological emergency (involving radioactive material).

13

OPEN ACCESS
IOP Publishing
Modelling and Simulation in Materials Science and Engineering
Modelling Simul. Mater. Sci. Eng. **32** (2024) 055017 (15pp) https://doi.org/10.1088/1361-651X/ad4b4b

# Identifying sub-cascades from the primary damage state of collision cascades

**Utkarsh Bhardwaj**[1,*] **and Manoj Warrier**[1,2]

[1] Computational Analysis Division, BARC, Vizag, AP 530 012, India
[2] Homi Bhabha National Institute, Mumbai, Maharashtra 400 094, India

E-mail: haptork@gmail.com

Received 9 February 2024; revised 2 May 2024
Accepted for publication 14 May 2024
Published 29 May 2024

**Abstract**

The morphology of a collision cascade is an important aspect in understanding the formation of defects and their distribution. While the number of sub-cascades is an essential parameter to describe the cascade morphology, the methods to compute this parameter are limited. We present a method to compute the number of sub-cascades from the primary damage state of the collision cascade. Existing methods analyze peak damage state or the end of ballistic phase to compute the number of sub-cascades which is not always available in collision cascade databases. We use density based clustering algorithm from unsupervised machine learning domain to identify the sub-cascades from the primary damage state. To validate the results of our method we first carry out a parameter sensitivity study of the existing algorithms. The study shows that the results are sensitive to input parameters and the choice of the time-frame analyzed. On a database of 100 collision cascades in W, we show that the method we propose, which analyzes primary damage state to predict number of sub-cascades, is in good agreement with the existing method that works on the peak state. We also show that the number of sub-cascades found with different parameters can be used to classify and group together the cascades that have similar time-evolution and fragmentation. It is seen that the number of SIA and vacancies, % defects in clusters and volume of the cascade, decrease with increase in the number of sub-cascades.

Keywords: sub-cascades, cascade morphology, collision cascades, radiation damage, molecular dynamics, ML applications

* Author to whom any correspondence should be addressed.

Modelling Simul. Mater. Sci. Eng. **32** (2024) 055017 U Bhardwaj and M Warrier

## 1. Introduction

The collision cascades that are caused by high energy irradiation can have different cascade morphologies. One of the standard parameter to understand the cascade morphology is the number of sub-cascades. Sub-cascades are damage spots with high density of atomic displacements, separated from each other by less dense regions of damage [1, 2]. The collision cascades initiated by low energy primary knock-on atom (PKA) have a single damage spot. The PKA energy at which the average number of sub-cascades are greater than one is called the sub-cascade threshold energy and differs for different materials. At higher energies a collision cascade may get fragmented into smaller sub-cascades. A sub-cascade can be either well-separated from other sub-cascades or it may overlap with one or more sub-cascades [3].

The cascade morphology and the formation of the sub-cascades affects the defect formation, defect sizes, defect morphologies and the spatial distribution of the defects [4, 5]. Morphology parameters such as sub-cascade count and volumes have been used to compare and evaluate inter-atomic potentials [6]. Vacancies occupy the central region in a sub-cascade and interstitials form the surrounding in a roughly spherical fashion. This arrangement is very strictly found in low energy disconnected sub-cascades or low energy collision cascades. In case of connected sub-cascades, large SIA clusters are formed at the locations of the connections of the sub-cascades [7]. A cascade with more number of sub-cascades will also have a relatively higher fraction of smaller clusters of vacancies and interstitials [5], except for the case of connected sub-cascades where large interstitial clusters get formed at the overlapping region. The damage from the disconnected sub-cascades caused by secondary knock-on atoms with a fraction of the energy of the PKA resemble a lower energy collision cascade. Above a certain energy threshold, cascade fragmentation becomes very probable and the damage regions do not show a linear increase in size and properties but rather they become a combination for lower energy cascades [8]. The time evolution of a cascade can be divided into three phases, initial recoil phase, peak displacement phase and the primary damage state at the end of the recombinations. The damage regions of all the phases have been shown to spatially correlate well with each other [3].

Sub-cascades simulated with binary collision approximation Monte-Carlo (BCA-MC) method have been extensively studied since decades using various methods such as fuzzy clustering [9], fractal method [10–12], identifying vacancy rich regions [11] etc. A relatively recent BCA-MC study of sub-cascades uses a different method of decomposing the complete domain into cubes named as elementary cubes (ECs) and finding connected regions of cubes that are above an energy threshold to calculate the sub-cascades. A similar approach has been recently used for analyzing the collision cascades in MD based on their peak damage state [13]. The method requires the position and energy of all the atoms at the peak damage state of the collision cascade for analysis. The other important parameters of interest in collision cascades such as the number of defects, defect sizes, defect morphologies [14], can all be calculated from the primary damage state. In databases of collision cascades such as the open CascadesDB database [15], only the primary damage state is provided. Outputting the intermediate steps also increases the simulation output data size by 10–50 times depending on the output frequency and impacts the efficiency due to high amount of data that is required to be written to disk. Moreover, it is the distribution of defects and damage regions at the primary damage state which are of interest from the point of view of initializing higher scale models of radiation damage with better spatial distribution. The higher scale models that incorporate spatial distribution such as the kinetic Monte Carlo account for reaction rates more accurately

14

Published by IOP Publishing for Sissa Medialab

Received: November 10, 2023
Revised: February 6, 2024
Accepted: March 21, 2024
Published: May 10, 2024

# Imaging of low Z masked with high Z (Pb, U) materials using 14 MeV neutron

**Saroj Bishnoi**,* **Tarun Patel, P.S. Sarkar and L.M. Pant**

*Technical Physics Division, Bhabha Atomic Research Centre, Mumbai 400085, India*

*E-mail:* saroj@barc.gov.in

Abstract: An experimental study has been performed using 14 MeV neutrons for imaging of low Z material (particularly composed of C, H, O elements) masked with thick layers of dense and high Z materials. The experimental setup consists of a D-T neutron generator, a metallic collimator and an imaging system. The imaging system is designed with a polypropylene zinc sulphide scintillator screen integrated with a lens coupled 16-bit ICCD camera. Imaging capability of the system was investigated using iron test samples with holes and line pair features. The minimum hole size of 2 mm could be imaged at a contrast of 36% and a line of 2 mm width visible at a contrast of 24% indicating the system's resolution of ~ mm. Low Z samples such as water ($H_2O$) and polyethylene $(C_2H_2)_n$ placed behind thick layers of Pb (40 mm) and Uranium (35 mm), were imaged successfully. These images reveal the system's ability towards low Z material imaging in the presence of heavier metals. Good contrast images acquired at a lower neutron yield of $\sim 5 \times 10^8$ n/sec of D-T neutron generator has provided a possibility to realise fast neutron imaging having moderate resolution (~ mm) with a smaller footprint and an economical system design for field applications.

Keywords: Neutron radiography; Inspection with neutrons; Accelerator Applications

2024 JINST 19 P05022

*Corresponding author.



https://doi.org/10.1088/1748-0221/19/05/P05022

## Contents



## 1 Introduction

Fast neutron radiography (FNR) is a powerful and rapidly growing non-destructive evaluation (NDE) tool with wide applications [1]–[4]. Fast neutrons are highly penetrating compared to most of the other existing NDE probes such as X/gamma-rays, thermal or cold neutrons etc., due to their low interaction cross section. Because of its strong penetrating capability and weak dependency on the atomic number (Z) of the material, FNR is the preferred approach for imaging and investigation of low Z materials to simultaneously be observed with heavier metals. Another important feature of fast neutrons is that they do not transmute nuclei as readily as thermal neutrons, since the capture cross-sections of fast neutrons are relatively very small. This feature allows objects to be released immediately after inspection and investigation without waiting too long for radioactive nuclei to decay to an acceptable safe radiation level.

Due to these unique and distinctive features, FNR has been explored in different industrial fields, such as security applications (cargo inspection for contraband such as narcotics, explosives, and illicit drugs) [5, 6] Imaging of special nuclear materials (SNM) [7, 8], radiography and tomography of encapsulated heavy shielded low Z compound materials [9, 10], cultural heritage investigation [11], etc. FNR can be performed with a variety of neutron sources, extending from fission neutrons to neutron generators, accelerators or spallation neutron sources, and nuclear reactors. Among them, reactors and large accelerators have been successfully used to develop advanced fast neutron imaging facilities, by virtue of their high neutron fluxes. Fast neutron imaging beam lines or test facilities for example, NECTAR: radiography and tomography station using fission neutrons [12], fast neutron tomography system designed at 500 kW research reactor, Ohio State University [13], and Fast neutron tomography (FNCT) experiments at an accelerator facility of PTB, Germany [14] have proven the potential use of these sources in producing high quality images. The neutron radiography facility relying on large neutron source has good beam quality, high imaging collimation ratio, and high beam intensity at the imaging plane, but the disadvantage is that the facilities are too large and the cost is high, which prevents them from meeting the users local testing needs. Other sources, like neutron generators (NGs), provide an advantage in designing FNR systems with a smaller footprint and higher neutron energies. The NGs are usually deuterium-deuterium (D-D) and deuterium-tritium

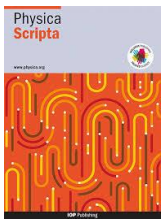

15

IOP Publishing Phys. Scr. 99 (2024) 065952 https://doi.org/10.1088/1402-4896/ad451f

Physica Scripta

PAPER

# Impact of $B_4C$ buffer layer on interface diffusion in Cr/Sc multilayers: combined study by x-ray reflectivity, scattering and fluorescence

P Sarkar[1,*], A Biswas[1], Sanjay Rai[2], M H Modi[2], Gurupada Ghorai[4], Pratap K Sahoo[4], S N Jha[3] and D Bhattacharyya[1]

[1] Atomic and Molecular Physics Division, Bhabha Atomic Research Centre, Mumbai, India
[2] Indus Synchrotron Utilisation section, Raja RamnnaCentre for Advanced Technology, Indore- 752013, India
[3] Beamline Development section, Bhabha Atomic Research Centre, Mumbai-400085, India
[4] School of Physical Sciences, National Institute of Science Education and Research, HBNI, Jatni, 752050, India
* Author to whom any correspondence should be addressed.

**E-mail:** piyali@barc.gov.in

**Keywords:** interface, multilayer thin film, soft x-ray reflectivity, barrier layer, GIXRF

OPEN ACCESS

RECEIVED
14 February 2024

REVISED
18 April 2024

ACCEPTED FOR PUBLICATION
29 April 2024

PUBLISHED
13 May 2024



## Abstract

In thin film multilayer based optical componentsof x-ray imaging system, diffusion of one material into the other degrades the reflectivity of the mirrors severely. Along with this thermodynamically driven diffusion, there are also growth generated interface roughness of different special frequencies and microstructures which can increase the diffused scattering from the multilayer and reduce the resolution of an image. Generally grazing incidence x-ray reflectivity in specular geometry (specular GIXR) and diffused x-ray scattering measurement in rocking scan geometry yield information regarding microstructure and overall diffusion at the interfaces of a multilayer. In this paper it is shown that grazing incidence x-ray fluorescence (GIXRF) measurement in standing wave condition alongwith the above measurements can give precise information regarding element-specific diffusion at the interfaces of a multilayer structure. Periodic multilayers made of 75 Cr/Sc bilayers with bilayer thickness ~4 nm with and without $B_4C$ barrier layer of 0.2 nm thickness at the interfaces have been prepared using ion beam sputtering system and characterized by GIXR, diffused x-ray scattering and GIXRF measurements using synchrotron x-ray radiation just above the Cr K-edge. From the above measurements, drastic reduction in interface diffusion of Cr and improvement of interface morphology after addition of $B_4C$ barrier layer at the interfaces of Cr/Sc multilayers have been observed which is also corroborated by cross-sectional transmission electron microscopy of the multilayers. Finally, in the water window soft x-ray region of 2.3–4.4 nm performance of these multilayers have been tested and the Cr/$B_4C$/Sc multilayer with improved interface quality has been found to yield ~30.8% reflectivity at 3.11 nm wavelength which is comparable with the best reported reflectivities in the literature at this wavelength.

## Introduction

Diffusion at the interfaces of two materials in thin film multilayers is one of the limiting phenomena in deciding the performance of these reflecting optical devices in x-ray imaging systems. In x-ray imaging applications, such as in optics for EUV lithography, BEUV lithography [1], x-ray microscopy [2], x-ray telescope [3] etc, interface diffusion reduces the contrast between consecutive layers, thus degrades the performance of the multilayer mirrors and finally reduces the image intensity. Same is also true for other applications of multilayer optical devices such as Laue lenses for free electron lasers [4], normal incidence soft x-ray mirrors [5, 6], neutron supermirrors [7] etc where interface diffusion decreases the throughput of the devices. Along with the thermodynamically driven diffusion of one element into the other, growth of physical roughness and microstructure during deposition is another source for imperfections of the interfaces. In case of thin film

multilayer based imaging system, the morphologies of the multilayer interfaces thusalso play key role in deciding the quality and resolution of the image.

Thus, characterization of the interface morphology of the multilayers and probing elemental diffusion across the interfaces are very much essential to have an in-depth understanding of the interface evolution, to improve the quality of the interfaces and to achieve the best performance of the devices. Grazing incidence x-ray reflectivity (GIXR) provides a straight-forward non-destructive way to characterize the interface imperfections of a multilayer sample [8]. In specular GIXR technique, x-ray reflectivity from the sample is measured as a function of grazing angle of incidence which depends only on the electron density profile perpendicular to the surface. Thus, the specular reflectivity technique can provide information only about the perpendicular component of momentum transfer ($q_z$) and the rms interfacial width ($\sigma$).The parameter $\sigma$ is a measure of either interfacial roughness in the case of a purely rough interface, or an diffusion width in the case of a purely a diffuse interface, or some combination of the two properties in the case of an interface that is both rough and diffuse. However, specular reflectivity cannot distinguish between graded (inter-diffused) and physically rough interfaces. Further information regarding interface roughness, interface diffusion and lateral correlation lengths of interface imperfections can be obtained by measuring diffused x-ray scattering of the sample with a nonzero lateral (along an interface) component of the scattering vector ($q_x$). As only interface roughness ($\sigma_r$) contributes [9] towards diffused scattering, by measuring both specular GIXR and diffused x-ray scattering, we can extract interface diffusion ($\sigma_d$) from total interface width ($\sigma$) using the following relation:

$$\sigma = \sqrt{\sigma_r^2 + \sigma_d^2} \tag{1}$$

Grazing incidence x-ray fluorescence (GIXRF) [10] technique, which is also non-destructive in nature, can also be used very effectively in probing the concentration profiles of elements across the depth of a multilayer particularly when bi-layer thickness of a multilayer is in nm scale where secondary ion mass spectrometry (SIMS) [11], x-ray photoelectron spectroscopy (XPS) [12], Rutherford back scattering (RBS) [13] etc are not very effective. In GIXRF technique,x-ray standing wave (XSW) induced x-ray fluorescence from a particular element present in the sample is measured as a function of the grazing angle of incidence, which depends on the elemental concentration profile of that particular element across the depth of the multilayer. Through specular and diffused GIXR measurements we cannot distinguish between the roles of two different elements of the multilayer towards interface diffusion. GIXRF, being element specific unlike GIXR, is selectively sensitive to interface diffusion of individual atomic species at the interfaces, for example on diffusion of Cr and Sc separately in case of a Cr/Sc multilayer. Thus a combined analysis of GIXR and GIXRF provides complete information on inter-diffusion in a multilayer and uniquely probes the role of constituent materials. De Boer [14] first derived the theoretical expression of GIXRF profile of a multilayer thin film and subsequently several researchers have effectively used this technique in characterisation of thin film multilayers [15]. Recently in case of Ni/Ti multilayers [16], by measuring Ni and Ti fluorescence from Ni/Ti multilayer samples annealed at different temperatures we have shown that at lower temperature Ni diffusion dominates while at higher temperature Ti diffusion dominates at the interfaces.

In the present study, Cr/Sc multilayer has been chosen for investigation as it is the best material combination of multilayer Schwarzschild objective for water window regime (2.3–4.4 nm) of soft ray microscopes. Although theoretically Cr/Sc possesses around 44% near normal reflectivity at $\lambda = 3.11$ nm with 400 numbers of bi-layers, the soft x-ray reflectivity obtained from such multilayers are strongly influenced by the interface imperfections and degrade drastically due to rough and graded interfaces. To have sharp and chemically abrupt interfaces, researchers have applied different interface engineering in Cr/Sc multilayer systems. Introduction of an ultrathin layer of a third material at each interface as a barrier layer is a well-known method to control diffusion. It has resulted in drastic improvement in the performance of the multilayers with material combinations like Mo/Si [17], Sc/Si [18], Cr/Ti [19], Cr/V [20] etc. Materials having lower surface energy such as C that helps in wetting of the interface [19] whereas $B_4C$ which is known to reduce interlayer mobility of metal atoms, are generally chosen as barrier layers as these results in two-dimensional growth of the multilayers with abrupt interfaces and reduced interface roughness [21, 22]. In case of Cr/Sc multilayer system also, there are a number of reports with $B_4C$ [22, 23], however, the above works mostly have reported the improvement in reflectivities and thermal stability obtained in Cr/Sc multilayer system upon inclusion of $B_4C$ [24, 25] and have not really estimated the elemental diffusion at the interfaces of Cr/Sc multilayers and the extent to which $B_4C$ helps to reduce it.

In the present work, periodic multilayers made of 75 Cr/Sc bilayers with bi-layer thickness ~ 4 nm with and without $B_4C$ barrier layer of 0.2 nm thickness have been prepared using an ion beam sputtering system and characterized by specular GIXR, diffused x-ray scattering and GIXRF techniques. The combined measurement and multi-parameter analysis of specular GIXR, diffused x-ray scattering and GIXRF data could uniquely probe the interface morphology and estimate the elemental diffusion at the interfaces which is very critical for improving the reflectivity of such multilayer systems. Finally, the performance of the multilayers at water

16

Journal of Cosmology and Astroparticle Physics
An IOP and SISSA journal

Received: January 12, 2023
Revised: June 17, 2024
Accepted: July 10, 2024
Published: August 9, 2024

# Inclusive fluxes of secondary air-shower particles

**Hariom Sogarwal and Prashant Shukla**

*Nuclear Physics Division, Bhabha Atomic Research Centre, Mumbai 400085, India*
*Homi Bhabha National Institute, Anushakti Nagar, Mumbai 400094, India*

*E-mail:* sogarwalhariom@gmail.com, pshukla@barc.gov.in

Abstract: The particle showers produced in the atmosphere due to the interactions of primary cosmic particles require a thorough understanding in the backdrop of searches for rare interactions. In this work, we made a comprehensive study of air shower simulations using various combinations of hadronic models and particle transport code of the CORSIKA package. The primary proton and helium distributions are taken as power law which are scaled to match the measured flux in balloon and satellite-based experiments at the top of atmosphere. The shower simulation includes production, transport and decays of secondaries up to the ground level. In this study, we focus on the bulk of the spectra and particles which is computationally intensive and hence parallel processing of events is done on computer cluster. We provide a way to normalize the simulation results to be compared with the ground-based measurements namely, single and multiple muon yields and their charge ratios as a function of zenith angle and momentum. This provides a basis for comparisons among the six model combinations used in this study and the differences are outlined. Most of the hadronic models in CORSIKA produce the bulk ground based measurements fairly well. We use one of the best model combinations to quantitatively predict the absolute and relative yields of various particles at ground level as well as their correlations with primaries and with each other. The leptonic ratios are obtained as a function of energy and zenith angle which are important inputs for the neutrino oscillation physics.

Keywords: cosmic ray theory, cosmic ray experiments, particle physics - cosmology connection, ultra high energy cosmic rays

ArXiv ePrint: 2211.02427



https://doi.org/10.1088/1475-7516/2024/08/013

JCAP08(2024)013

## Contents



## 1 Introduction

The cosmic rays consisting of high energy charged particles continuously bombard the Earth from all directions and have remained one of the most interesting and active areas of research [1]. The particle showers produced in the atmosphere due to the interactions of these primary cosmic particles have provided a natural laboratory of physics of standard and beyond standard models which led to many discoveries. Accurate knowledge of both the primary as well as secondary particles is an important prerequisite for search of rare interactions. The primary cosmic rays consist of protons (90%), helium nuclei (9%) and other heavy nuclei (1%) which have been produced and accelerated in astrophysical processes to high energies as large as $10^8$ TeV. Upon entering the atmosphere, the primary cosmic particles interact with the nuclei of oxygen and nitrogen gases roughly 12 km above Sea level. These interactions lead to the production of shower of hadrons, mainly pions and kaons with a small percentage of heavier particles which move downwards while losing energy and decaying. These particles introduce cosmogenic signal and background for the measurement of neutrino oscillation physics and hence their study is very useful to precisely understand the mass difference of the neutrinos in the 2-3 sector and the mass hierarchy. Although neutrinos are the most abundant shower particles at the Earth surface, muons are the most abundant charged particles and are responsible for half of the terrestrial radiation dose taken by a body on Earth. Measurements of muon distributions at ground is an active field and the improved theoretical understanding and detection technologies are providing more insights in the particle production in showers [2, 3]. LHC is working on a dedicated experiment of proton-oxygen collisions to understand the air shower physics. This dedicated LHC run will help in tuning of various hadronic interaction parameters used in the cosmic ray packages for better understanding of the air shower produced in the atmosphere and spectra of various particles at ground level [4].

The shower simulation codes employ hadronic interaction models which have energy dependent hadronic cross-section calculations as the main body of the simulation. CORSIKA



JCAP08(2024)013


17

IOP Publishing Surf. Topogr.: Metrol. Prop. 12 (2024) 015022 https://doi.org/10.1088/2051-672X/ad331d

Surface Topography: Metrology and Properties

PAPER

# Influence of swift heavy ion irradiation on structure and morphology of $La_{0.25}Pr_{0.375}Ca_{0.375}MnO_3$ film

**Harsh Bhatt**[1,2], **Yogesh Kumar**[3], **R B Tokas**[4], **A P Singh**[5], **Fouran Singh**[6] and **Surendra Singh**[1,2,*]

[1] Solid State Physics Division, Bhabha Atomic Research Centre, Mumbai 400085, India
[2] Homi Bhabha National Institute, Anushaktinagar, Mumbai 400094, India
[3] UGC-DAE Consortium for Scientific Research, R-5 Shed, BARC, Mumbai 400085, India
[4] Atomic and Molecular Physics Division, Bhabha Atomic Research Centre, Mumbai 400085, India
[5] Physics Department, Dr B R Ambedkar National Institute of Technology, Jalandhar 144027, India
[6] Material Science Group, Inter University Accelerator Centre, Aruna Asaf Ali Marg, New Delhi 110067, India
[*] Author to whom any correspondence should be addressed.

**E-mail:** lucky1708@gmail.com (Y Kumar) and surendra@barc.gov.in

**Keywords:** structure and morphology of manganite thin film, swift heavy ion irradiation, x-ray reflectivity, atomic force miscroscopy

**OPEN ACCESS**

**RECEIVED**
30 October 2023

**REVISED**
30 January 2024

**ACCEPTED FOR PUBLICATION**
12 March 2024

**PUBLISHED**
21 March 2024



## Abstract

The effects of $Ag^{15+}$ (120 MeV) swift heavy ion (SHI) irradiation on the structural and morphological properties of epitaxial $La_{0.25}Pr_{0.375}Ca_{0.375}MnO_3$ (LPCMO) thin films were investigated by x-ray scattering and atomic force microscopy (AFM) techniques. LPCMO films of thickness ~ 280 Å were irradiated with an $Ag^{15+}$ ion beam at different fluences of $1 \times 10^{11}$, $5 \times 10^{11}$, and $1 \times 10^{12}$ ions $cm^{-2}$. XRD results suggested the development of the tensile stress along the out-of-plane direction of the LPCMO film upon ion irradiation, which increases on increasing the ion fluence. The morphology of the film was also modified with the irradiation and an increase in the fluence of the ion beam enhanced the in-plane height-height correlation length scale (grain size) with a loss of the fractal behaviours. The linear variation of microstrain with ion irradiation fluence in thin LPCMO film can be considered for a possible strain-driven application in modifying functional properties of such a phase separated complex oxide.

## Introduction

Manganite-based complex oxides are strongly correlated electronic systems which exhibit magnetoelectronic phase separation that gives rise to properties like colossal magnetoresistance (CMR), metal-to-insulator transition (MIT), colossal electroresistance (CER) and colossal piezoresistance (CPR) [1–5]. The competition and interplay among charge, spin, orbital, and lattice degrees of freedom lead to the coexistence of multiple phases and related electronic and magnetic properties in manganite oxides [1, 6]. Mixed valance bulk $(La_{1-y}Pr_y)_{1-x}Ca_xMnO_3$ manganite, a prototypical electronic phase-separated system, has been studied extensively and it shows a phase separation of nanometer and micron length scale [5–11]. However thin films of $(La_{1-y}Pr_y)_{1-x}Ca_xMnO_3$ have exhibited properties different from bulk behaviour because of the additional knob (strain) accessible in the case of thin films, suggesting that the strain field can tune the transport and magnetic properties as well as the phase coexistence [7, 12–20]. In the bulk phase, a nanometer and micron length scale phase separation has been observed for two manganites with slightly different compositions i.e. $(La_{1-y}Pr_y)_{1-x}Ca_xMnO_3$ ($y = 0.6$) with $x = 0.33$ and $x = 0.375$ [7, 9]. Different phenomena, like magnetic anisotropy driven single to multi-domain transition [12], electronic phase separation (EPS) [13–18], correlation of electronic and magnetic phases [16, 17], coupling of bending strain and magnetism [13, 14, 19, 20], and electric field-driven phase separation [3, 21] have been reported for the thin film of $(La_{1-y}Pr_y)_{1-x}Ca_xMnO_3$ with $x = 0.33$ and $y = 0.6$. However, the $(La_{1-y}Pr_y)_{1-x}Ca_xMnO_3$ film with $x = 0.375$ and $y = 0.6$ has been studied rarely even though a larger phase separation (length ~ micron) was suggested for this system in their bulk form [9].

Strain and related structural disorders can influence the competing interactions between different degrees of freedom and phase coexistence in the manganite films by modifying the structure and morphology. The effect of strain in manganite films is studied in both ways by

IOP Publishing Surf. Topogr.: Metrol. Prop. 12 (2024) 015022 H Bhatt et al

applying strain (i) directly for substrate-induced strain [22–26], bending strain [4, 13, 14, 19, 20], and (ii) indirectly i.e. ion implantation [27–29] and swift heavy ion (SHI) irradiation [30–35]. The SHI irradiation using 100 MeV $O^{7+}$ ions with different fluences of $LaMnO_3$/$Nd_{0.7}Sr_{0.3}MnO_3$/STO heterostructure showed a change in strain field across interfaces [35]. The influence of SHI irradiation on the magnetic proximity effect in oxide-based manganite/superconductor heterostructure has also been demonstrated as a modification in structure, magnetic, and superconducting properties upon irradiation [36]. Recently, Matthews *et al* [34] observed the formation and percolation of a network of disorder in the $LaMnO_3/SrTiO_3$ heterostructures on ion irradiation, which led to a change in structural and morphological properties at interfaces. Using x-ray resonant magnetic scattering (XRMS), Singh *et al* [16, 17] correlated the electronic and magnetic phases across MIT temperature of the $(La_{1-y}Pr_y)_{1-x}Ca_xMnO_3$ thin film with $x = 0.375$ and $y = 0.6$ and found that these properties are highly dependent on the morphology of the interfaces.

There are several ways to control the structure and morphology of the surfaces and interfaces of thin film and a suitable characterization in this respect is required to study its influence on macroscopic properties. Thin films, grown by physical vapour deposition techniques like thermal evaporation [37], sputtering [38], and pulsed laser deposition (PLD) [12, 19, 39] have shown great structural and compositional stabilities. The PLD is an ideal and preferred technique for the deposition of compound oxide films because it maintains the stoichiometry of the target compound. The SHI irradiation [37], as well as low energy ion irradiation [38] of the thin films, have shown modification in microstructure (change in microstrain and crystallite size) and morphology without changing the crystalline structure (atomic length scale) even on varying the fluence of ion by an order of three [40]. Here, we report the evolution of structure and morphology upon ion irradiation of the $(La_{1-y}Pr_y)_{1-x}Ca_xMnO_3$ film with $x = 0.375$ and $y = 0.6$ (i.e. $La_{0.25}Pr_{0.375}Ca_{0.375}MnO_3$ film) (LPCMO) grown on single crystal (110) $NdGaO_3$ (NGO) substrate. Combining the x-ray scattering and atomic force microscope (AFM) measurements we have investigated the structural and morphological properties of the LPCMO film upon ion irradiation with different influences. These results suggest a strong modification in the microstrain and morphology of LPCMO film upon ion irradiation and parameters describing the depth-dependent structure and morphology are strongly correlated. The surface shows self-affine fractal behaviours which reduces upon irradiating the LPCMO film with a high ion fluence. We found a linear increase in the out-of-plane lattice constant (tensile strain) on increasing the fluence of SHI ion, suggesting that a controlled strain can be applied in oxide films using ion irradiation for studying the strain-field dependent properties.

## Experimental details

### Sample growth, swift heavy ion irradiation and structural characterization

The LPCMO thin film of thickness ~300 Å was deposited from a high-density bulk target on a single crystal (110) NGO substrate using the PLD technique [39]. Extensive studies related to the structure and magnetic properties of manganite films have been reported earlier on similar thicknesses of the film [11, 16, 17]. The exact thickness of the film was estimated to ~ 280 Å using x-ray reflectivity (XRR) measurements (discussed later). A KrF excimer laser ($\lambda = 248$ nm, pulse width = 20 ns) with an energy density of ~4 J $cm^{-2}$ was used to ablate the high-density LPCMO target. The PLD chamber was evacuated to a pressure of $10^{-6}$ mbar before the deposition to avoid any impurities. The oxide film was grown in an oxygen environment. During the deposition oxygen partial pressure of 0.2 mbar and a substrate temperature of 750 °C were maintained. Annealing of the thin film was carried out at the same substrate temperature after deposition for 30 min in a 1000 mbar oxygen environment after which the film was allowed to cool naturally in the same oxygen environment. The pristine LPCMO thin film (10 mm × 10 mm) was cut into four equal pieces (5 mm × 5 mm) and three pieces of the sample were irradiated at room temperature using 120 MeV $Ag^{15+}$ ions at a fluence of $1 \times 10^{11}$, $5 \times 10^{11}$, and $1 \times 10^{12}$ ions $cm^{-2}$. Thus, for the present study, we have a pristine LPCMO film and three ion-irradiated LPCMO films with different fluences mentioned above. The ion-irradiation experiment was carried out at the Inter University Accelerator Centre (IUAC), New Delhi using the 15UD tandem accelerator under high vacuum conditions.

Depth-dependent structure analysis using *ex situ* XRR measurements (discussed later) suggested the growth of high-quality film with very small substrate-film roughness of ~3 Å. The compositional analysis of the pristine film is carried out using energy-dispersive x-ray (EDX) analysis. Scanning electron microscopy (SEM) image of the pristine film was recorded using SERON Technologies Inc. (Model: AIS 2100) operating at 20 keV. The EDX measurements were carried out using Oxford Instruments (Model: INCA E350) coupled to the Vega MV2300t/40 scanning electron microscope. Structural characterization of the pristine and irradiated films was carried out using x-ray scattering with Cu $K\alpha$ radiation from a rotating anode source, where x-ray diffraction (XRD) was used to investigate the atomic structure (strain) and XRR was used to investigate the depth-dependent structure.

### Morphological analysis using AFM

The surface topographic measurements were carried out using NT-MDT's solver-P47H ambient-based multimode AFM in intermittent-contact mode. A

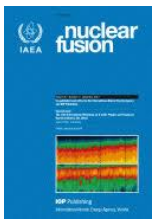

18

OPEN ACCESS
IOP Publishing | International Atomic Energy Agency
Nuclear Fusion
Nucl. Fusion 64 (2024) 056007 (16pp)
https://doi.org/10.1088/1741-4326/ad2b5f

# Micro-particle injection experiments in ADITYA-U tokamak using an inductively driven pellet injector

**Sambaran Pahari[1,*], Rahulnath P.P.[1], Aditya Nandan Savita[1], Pradeep Kumar Maurya[1], Saroj Kumar Jha[1], Neeraj Shiv[1], Raghavendra K.[1], Harsh Hemani[1], Belli Nagaraju[1], Sukantam Mahar[1], Manmadha Rao[1], I.V.V. Suryaprasad[1], U.D. Malshe[8], J. Ghosh[2,3], B.R. Doshi[2], Prabal Kumar Chattopadhyay[2,3], R.L. Tanna[2,4], K.A. Jadeja[2,5], K.M. Patel[2], Rohit Kumar[2], Tanmay Macwan[2,3], Harshita Raj[2,3], S. Aich[2,3], Kaushlender Singh[2,3], Suman Dolui[2,3], D. Kumawat[2], M.N. Makwana[2], K.S. Shah[2], Shivam Gupta[2], V. Balakrishnan[2], C.N. Gupta[2], Swadesh Kumar Patnaik[2], Praveenlal Edappala[2], Minsha Shah[2], Bhavesh Kadia[2], Nandini Yadava[2,4], Kajal Shah[2,6], G. Shukla[2], M.B. Chowdhuri[2,3], R. Manchanda[2], Nilam Ramaiya[2], Manoj Kumar[2], Umesh Nagora[2,3], Varsha S.[2,3], S.K. Pathak[2], Kumudni Asudani[2], Paritosh Chaudhuri[2], P.N. Maya[2], Rajiv Goswami[2], A. Sen[2,3], Y.C. Saxena[2,3], R. Pal[7] and S. Chaturvedi[1,2,3]**

[1] Computational Analysis Division, Bhabha Atomic Research Centre, Visakhapatnam, Andhra Pradesh 531011, India
[2] Institute for Plasma Research, Bhat, Gandhinagar 382428, Gujarat, India
[3] Homi Bhabha National Institute, Training School Complex, Anushaktinagar, Mumbai 400094, India
[4] Institute of Science, Nirma University, Ahmedabad 382481, Gujarat, India
[5] Department of Physics, Saurashtra University, Rajkot, Gujarat, India
[6] Pandit Deendayal Petroleum University, Raisan, Gandhinagar 382007, Gujarat, India
[7] Saha Institute of Nuclear Physics, Kolkata, India
[8] Bhabha Atomic Research Centre, Trombay, Mumbai 400085, India

E-mail: sambaran@barc.gov.in

Received 28 March 2022, revised 30 November 2023
Accepted for publication 21 February 2024
Published 15 March 2024

**Abstract**

A first-of-its-kind, inductively driven micro-particle (Pellet) accelerator and injector have been developed and operated successfully in ADITYA-U circular plasma operations, which may ably address the critical need for a suitable disruption control mechanism in ITER and future tokamak. The device combines the principles of electromagnetic induction, pulse power technology, impact, and fracture dynamics. It is designed to operate in a variety of environments, including atmospheric pressure and ultra-high vacuum. It can also accommodate a wide range of pellet quantities, sizes, and materials and can adjust the pellets' velocities over a coarse and fine range. The device has a modular design such that the maximum velocity can be increased by increasing the number of modules. A cluster of lithium titanate/carbonate

* Author to whom any correspondence should be addressed.

Nucl. Fusion **64** (2024) 056007 S. Pahari *et al*

($Li_2TiO_3$/$Li_2CO_3$) impurity particles with variable particle sizes, weighing ∼50–200 mg are injected with velocities of the order of ∼200 m $s^{-1}$ during the current plateau in ADITYA-U tokamak. This leads to a complete collapse of the plasma current within ∼5–6 ms of triggering the injector. The current quench time is dependent on the amount of impurity injected as well as the compound, with $Li_2TiO_3$ injection causing a faster current quench than $Li_2CO_3$ injection, as more power is radiated in the case of $Li_2TiO_3$. The increase in radiation due to the macro-particle injection starts in the plasma core, while the soft x-ray emission indicates that the entire plasma core collapses at once.

Supplementary material for this article is available online

Keywords: pellet injector, fusion, disruption mitigation, electromagnetic launcher, ITER

(Some figures may appear in colour only in the online journal)

## 1. Introduction

The global energy crisis and challenges of reducing carbon footprint are being addressed by actively pursuing nuclear fusion research through magnetic confinement of high-temperature plasmas. International efforts to build commercial fusion reactors are currently plagued by many unresolved issues related to the deleterious effects of mechanical load (due to electromagnetic effects), heat load, energetic particles generated from the plasma disruption, and sudden termination of plasma [1, 2]. Research and development are underway globally to develop robust mitigation systems against disruptive events by quenching a burning fusion plasma using pellet injectors. These injectors mostly inject gas [3] or frozen-gas (cryogenic) pellets [4–6], the latter often shattered before injection (shattered pellet injection or SPI) [7–10]. Massive gas injection (MGI) techniques are inherently limited by complex quench requirements, and high energy barriers at the edge of the plasma which further get aggravated when large-volume plasmas must be accessed [11–13]. SPI systems remain much superior and are chosen as the baseline technology for ITER disruption mitigation (DMS) [10]. While it was initially thought that a large fraction may get vaporized upon shattering thereby reducing the chances of deep fragmentation, however, these concerns are now well addressed by Gebhart *et al* [14]. Though inherently limited by the slow response time of mechanical valves present in the gas-feed system and/or issues connected with situating the valves near the reactor vessels, a response time of SPI is now well within ∼20 ms outlined by the ITER DMS specifications [14–16]. The experiments on DIII-D have experimentally demonstrated the advantages of SPI over the MGI in all regards achieving pellet velocities of ∼200 m $s^{-1}$, before fragmentation [7, 8, 17].

Despite the good progress made with Shattered Neon Pellet Injection, presently considered the most promising candidate for ITER DMS, challenging scenarios can be envisaged during disruption with conflicting requirements that demands simultaneous reduction of induced vessel forces, conducted heat loads, and runaway electrons. In recent times pneumatically driven Solid Shell Pellets [18] have also been injected to achieve discharge shutdown. The radiative material that is typically held in a shell can accomplish deep penetration without ablation and is directly deposited in the desired region where it is the most effective. The resulting inward–outward thermal quench (TQ) lowers the conducted heat load as is predicted for high-Z shutdowns, whereas prolonged current quench and reduced induced vessel forces are expected as a characteristic of lower Z-shutdowns. The tracer-encapsulated solid pellets of ∼900 $\mu$m are injected into the Large Helical Device with a velocity of 300–500 m $s^{-1}$ [19]. However, due to the higher masses of shell or solid particle injection approaches based on well-established pneumatic drives may fall well short of reaching the desired injection velocity. Due to the modest thermal velocity of the propellant gas molecules, velocities are expected to be restricted to 300–400 m $s^{-1}$ [16], this increases the time required to travel the few meter lengths before it reaches the plasma edge. Furthermore, even though it is anticipated that most ITER disruptions will have a warning time of at least 20 ms, due to the involvement of mechanical valves, such acceleration techniques may not be appropriate in case of a shorter warning time scale in the incident of shutting down the plasma discharge with a large plasma volume. Apart from DMS dissipation of post-disruption runaway electron plateaus by SPI in DIII-D is also reported [20].

An electromagnetic pellet injector is projected to readily overcome these restrictions since higher velocities can be attained and such a device can accomplish short warning timelines [21]—both of which are critical for large-sized fusion-grade reactors. Acceleration is due to Lorentz forces experienced by current-carrying conductors in a magnetic field. In one such proposal being actively pursued by Raman *et al* [21, 22], the concept of a Railgun has been adapted to accelerate a solid pellet. An external energy source has been used to drive a primary current through two current-carrying rails. A conducting capsule placed across the rails helps to complete the primary circuit and is also configured to act as a solid pellet to be released into the fusion reactor. Depositing the radiative material directly in the runaway current channel formation region both the TQ and formation of runaway electrons could be suppressed [22].

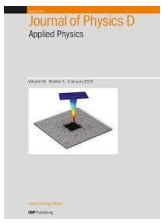

19

OPEN ACCESS
IOP Publishing
Journal of Physics D: Applied Physics
J. Phys. D: Appl. Phys. **58** (2025) 033003 (27pp)
https://doi.org/10.1088/1361-6463/ad7ff8

**Topical Review**

# Multifunctional 2D $MoTe_2$: Recent developments and future perspectives

**Fency Sunny[1], Chitra Lekha C S[1,2], Nandakumar Kalarikkal[1,3,4], C S Rout[5,*] and Brahmananda Chakraborthy[6,7,*]**

[1] International and Inter University Centre for Nanoscience and Nanotechnology, Mahatma Gandhi University, Kottayam 686 560, Kerala, India
[2] School of Nanoscience and Nanotechnology, Mahatma Gandhi University, Kottayam 686 560, Kerala, India
[3] School of Pure and Applied Physics, Mahatma Gandhi University, Kottayam 686 560, Kerala, India
[4] Centre for Ultrafast Studies, Mahatma Gandhi University, Kottayam 686 560, Kerala, India
[5] Centre for Nano and Material Sciences, Jain University, Jain Global Campus, Jakkasandra, Ramanagaram, Bangalore 562112, India
[6] High Pressure and Synchrotron Radiation Physics Division, Bhabha Atomic Research Centre, Trombay, Mumbai 400 085, India
[7] Homi Bhabha National Institute, Mumbai 400 094, India

E-mail: csrout@gmail.com and brahma@barc.gov.in

Received 24 February 2024, revised 14 June 2024
Accepted for publication 26 September 2024
Published 22 October 2024

**Abstract**

Two-dimensional (2D) transition metal dichalcogenides (TMDs), especially molybdenum ditelluride ($MoTe_2$), are an attractive topic in the modern era due to their unique properties. Although research progress on 2D materials has gained a lot of attention due to new synthesis methods and their extraordinary properties compared to their bulk counterparts, there is room for modification for large-scale production and tailoring the output performance in specific applications, such as solar cells, energy storage and conversion devices. Compared to other 2D TMDs, $MoTe_2$ offers a lower band gap, which in turn gives the possibility to replace Si in many applications. This review is an attempt to assemble and encapsulate the physical properties, recent developments in the fabrication of 2D $MoTe_2$ and its different applications in the field of batteries, transistors, energy conversion, solar cells, etc. This review will help to provide a deep insight into the research on $MoTe_2$ for modifying the structure and enhancing the properties of these layered materials.

Keywords: transition metal dichalcogenides, $MoTe_2$, Weyl semi-metals, property enhancement, synthesis approaches, energy applications

* Authors to whom any correspondence should be addressed.

J. Phys. D: Appl. Phys. **58** (2025) 033003 Topical Review

## 1. Introduction

In recent years, research advances in two-dimensional (2D) transition metal dichalcogenides (TMDs) have increased dramatically due to their distinctive properties [1–5]. Their larger surface area and novel properties make them promising candidates for a wide range of applications [6]. The remarkable elementary properties that provide promising energy solutions also cause TMDs to attract significant attention. The typical layered crystal structure consists of each unit with a transition metal (M) layer sandwiched between two atomic layers of chalcogen (X) (table 1). TMDs crystallize in thermodynamically stable phases of either 2H or 1T. Other alternate phases are obtained as metastable ones, wherein the formation of TMDs completely depends on the chalcogen and metal elements involved in the reaction. Within each layer, the atoms are bonded covalently as X–M–X with oxidation states +4 and −2 for the metal and chalcogen atoms, respectively. The distinct layers found in all TMDs are connected by weak van der Waals (vdW) forces, which make the exfoliation to 2D form easier compared to other nanostructures such as thin films and thick films. The synthesis of 2D TMD nanosheets by the top-down approach, such as exfoliation of layers from bulk crystals, or the bottom-up approach, such as the building up of individual atoms via different deposition techniques, is perfectly implemented in large-scale production of 2D materials because of the presence of weak vdW forces between the atomic layers [7, 8].

Among the TMD family, molybdenum ditelluride ($MoTe_2$) has attracted massive research interest recently owing to its promising opto-electronic properties [9]. The semiconductor to semi-metal transition based on its phase has attracted attention to $MoTe_2$ since the 1970s [11]. Having a lower band gap than the other TMDs with a value comparable to that of silicon puts $MoTe_2$ at the pedestal for electrostatic gating applications by efficient control of both holes and electrons [12]. The smaller band gap along with the improved absorption throughout the solar spectrum and strong spin–orbit coupling (SOC) make $MoTe_2$ one of the promising TMDs for optoelectronic, photovoltaic, spintronic and valleytronic applications.

One of the main features of this TMD is the easy interchangeability of phases. Different chemical and physical treatments have been reported to induce a structural phase transition between the hexagonal semiconducting phase (2H) and the monoclinic metallic phase (1T′) of $MoTe_2$. Alkali metal doping, electrostatic doping, laser irradiation, etc. are some of the investigated triggers to achieve the phase transition [12]. The 2H phase of the molybdenum ditelluride (2H-$MoTe_2$) semiconductor, in its 2D form, has attracted the attention of researchers owing to its favorable physical properties for future electronic devices, such as the band gap, suitable ambipolar transport and superior chemical stability [12, 13]. The different phases of $MoTe_2$ exhibit differing properties and characteristics. McGlynn *et al* reported the catalytic performance of the monoclinic metallic phase of 1T′ $MoTe_2$ for a hydrogen evolution reaction (HER) [14]. The developed nanocrystalline 1T′ $MoTe_2$ with metallic character showed a large enhancement in the electrocatalytic activity toward HER. Ma *et al* reported that the effective structural variance between the 2H and 1T′ phases due to tellurium defects increases the rate of $Li^+$ diffusion [15]. Pradan *et al* showed the effectiveness of few-layered $MoTe_2$ as a field effect transistor (FET) [16]. These results in applications are varied, efficient and practical. There has been a growing research interest that has not been completely summarized.

**Table 1.** Constituent elements of group VI TMDs along with the nature of the compounds.

| Group VI transition metals | Chalcogens | Nature of compounds formed |
|---|---|---|
| Mo | S, Se, Te | $MoS_2$, $MoSe_2$: Semiconducting $MoTe_2$: Semiconducting/semi-metallic |
| W | S, Se, Te | $WS_2$, $WSe_2$: Semiconducting $WTe_2$: Semi-metallic [9, 10] |

There have been works consolidating the properties and applications of other TMDs, such as $MoS_2$ alone, and a combined review of all the TMDs [5, 10, 17]. As far as we know, there has not been any comprehensive review of $MoTe_2$, comprising its properties and applications. This review attempts to provide a comprehensive outlook on the multifunctional facet of two-dimensional $MoTe_2$. In this review, we first discuss the different properties of 2D $MoTe_2$ that make it stand out among group-VI TMDs. The structural properties and the crystal structure along with the unique electronic, optical, electrical, magnetic and superconducting properties are summarized and discussed. The various synthesis procedures involved, belonging to both the top-down and bottom-up categories, are described. The synthesis methods that are scalable and simpler are given detailed attention. Finally, the different applications of 2D $MoTe_2$ are described, including those in energy conversion and storage, photocatalysts, sensors, solar cells, FETs and field emitters.

## 2. Properties

### 2.1. Crystal structure and properties

TMDs typically crystallize in a layered trigonal prismatic structure characterized by strong in-plane covalent bonds, weak in-plane vdW bonds, strong SOC and the absence of inversion symmetry [16].

Generally, TMDs like $MoS_2$ crystallize in two isotropic phases: the hexagonal 2H phase and the octahedral 1T phase (as shown in figure 1). In $MoTe_2$, a distortion in the 1T phase gives rise to a 180° rotation of the upper Te atom with respect to the lower Te atom, forming a Mo-centered octahedral. This leads to the formation of either 1T′ or $T_d$ phases [18]. Altogether, layered $MoTe_2$ possesses two stable phases: a

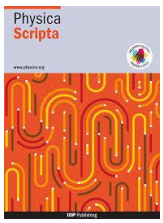

20

IOP Publishing Phys. Scr. 99 (2024) 125971 https://doi.org/10.1088/1402-4896/ad9120

Physica Scripta

PAPER

# Normalization of hot deformation parameters for activation energy analysis in metallic alloys

Parag M Ahmedabadi

Materials Processing & Corrosion Engineering Division, Bhabha Atomic Research Centre, Trombay, Mumbai 400 085, India

E-mail: aparag@barc.gov.in

Keywords: hot deformation, activation energy, normalized variables, strain rate sensitivity, Arrhenius-type model

OPEN ACCESS

RECEIVED
24 April 2024

REVISED
5 November 2024

ACCEPTED FOR PUBLICATION
11 November 2024

PUBLISHED
21 November 2024



## Abstract

Depending on the melting point of a given alloy, the temperature range for hot deformation of alloys varies widely. Consequently, the apparent activation energy of hot deformation, $Q$, is greatly influenced by the temperature range as well as the strain rate applied during hot deformation. The purpose of this investigation is to normalize hot deformation parameters—temperature and strain rate—to study their effects on activation energy. Seventy published hot-deformation datasets were used to investigate the effects of normalized hot-deformation variables on Arrhenius-type constitutive model parameters. Flow stress, strain rate, and temperature from sample datasets were normalized to the range [0, 1] and fitted with an Arrhenius-type model. The results showed that, for normalized parameters, the activation energy has exponential relationships with the partial derivative of flow stress with respect to strain rate and temperature.

Flow stress behavior during hot deformation is generally described using the following Arrhenius-type constitutive model.

$$\ln Z = \ln \dot{\varepsilon} + \frac{Q_d}{RT} = \ln j(\sigma) = \begin{cases} \ln A_1 + n' \ln \sigma \\ \ln A_2 + \beta\sigma \\ \ln A_3 + n \ln [\sinh(\alpha\sigma)] \end{cases} \quad (1)$$

Here, $\sigma$ is flow stress, $\dot{\varepsilon}$ is strain rate, $T$ is temperature, and $Z$ is the Zener-Holloman parameter[1]. In equation (1), $R$ is the universal gas constant, and $A_1$, $A_2$, and $A_3$ are scaling factors. The coefficients of flow stress, $n'$, $n$, $\beta$, and $\alpha$, are material parameters with $\alpha \approxeq \beta/n'$. Generally, the parameters in equation (2) are calculated at peak flow stress to avoid mentioning the strain value [2].

Let representations of flow stress be collectively denoted by the symbol $z$, $x = \ln \dot{\varepsilon}$, and temperature as $y = 1/T$. The partial derivatives of flow stress $z$ with respect to $x$ and $y$ are given by

$$m = \left(\frac{\partial z}{\partial x}\right)_y, \quad b = \left(\frac{\partial z}{\partial y}\right)_x \quad (2)$$

Where $m = 1/n'$ is the strain rate sensitivity parameter, and $b = Q/n'R$ for $z = \ln \sigma$. Therefore, according to equation (3), the activation energy of hot deformation, $Q$, is given by (for all forms of flow stress),

$$Q = R\left(\frac{\partial z}{\partial y}\right)_x \left(\frac{\partial z}{\partial x}\right)_y^{-1} = R\frac{b}{m} = -R\left(\frac{\partial x}{\partial y}\right)_z \quad (3)$$

The value of $Q$ is always compared with the activation energy for self-diffusion. However, $Q$ is generally higher than the energy for self-diffusion due to obstacles to dislocation motion, for example, a second phase in the matrix [3]. The above method for calculating $Q$ assumes that the slopes $m$ and $b$ are constants; this means that the plots of $z$ versus $x$ (and $z$ versus $y$) should be parallel. However, this is not usually the case, and generally, the average values of $m$ and $b$ are considered for calculating $Q$.

The values of $m$ depend on $y$ (temperature), and $b$ depends on $x$ (strain rate); both these slopes are not independent of each other. This suggests a possibility of mathematical relationships among $m$, $b$, and $Q$ for

IOP Publishing Phys. Scr. 99 (2024) 125971 P M Ahmedabadi

different materials. However, no such mathematical dependence has been reported so far. Further, since $m$ and $b$ (hence, $Q$) also depend on the ranges of hot deformation variables, normalization of variables $x$, $y$, and $z$ may bring uniformity in the values of $m$, $b$, and $Q$ for different metallic materials.

This investigation aims at evaluating the effects of normalization of variables on $m$, $b$, and $Q$ and also exploring mathematical relationships among $m$, $b$, and $Q$ for normalized variables. Variables $x = \ln\dot{\varepsilon}$, $y = 1/T$, and three forms of $z$ are normalized to the range [0, 1] using the following equation.

$$X' = \frac{X - X_{\min}}{X_{\max} - X_{\min}} \tag{4}$$

Here, $X'$ can be $x$, $y$, or $z$, and $X_{\min}$ and $X_{\max}$ are respectively the minimum and maximum values of variable $X$ in a given data set. Applying transformation of equations (4) to (2) we get,

$$m' = \left(\frac{\partial z'}{\partial x'}\right)_{y'} = \left(\frac{x_{\max} - x_{\min}}{z_{\max} - z_{\min}}\right) m = \frac{\Delta_x}{\Delta_z} m \tag{5}$$

$$b' = \left(\frac{\partial z'}{\partial y'}\right)_{x'} = \left(\frac{y_{\max} - y_{\min}}{z_{\max} - z_{\min}}\right) b = \frac{\Delta_y}{\Delta_z} b \tag{6}$$

Where, $\Delta_x = x_{\max} - x_{\min}$, $\Delta_y = y_{\max} - y_{\min}$, and $\Delta_z = z_{\max} - z_{\min}$. The activation energy for normalized variables is given by,

$$Q' = R\frac{b'}{m'} = -R\left(\frac{\partial x'}{\partial y'}\right)_{z'} = \left(\frac{y_{\max} - y_{\min}}{x_{\max} - x_{\min}}\right) Q = \frac{\Delta_y}{\Delta_x} Q \tag{7}$$

The values of $m'$, $b'$, and $Q'$ can also be calculated by fitting normalized data using equation (1). The material parameters of equation (1) for normalized data will be different from the corresponding values for the original data.

Normalized flow stress from several published data sets was fitted using equation (1) as a function of normalized strain rate and temperature. Because $Q$ is dependent on $m$ and $b$, the possibility of a mathematical relationship between these variables is explored for original and normalized data sets. All three forms of flow stress mentioned in equation (1) were investigated. A large number of sample data sets were selected from the literature to investigate the effects of normalization on slopes and activation energy [4–51]. The total number of sample data sets is 70 from 47 references, with many investigations providing more than one data set. For example, [24] provides 6 data sets for 6 different steels, while [30] gives 8 data sets for 8 different strain levels. All sample data sets were randomly selected and consisted of ferrous and non-ferrous alloys. It is worth mentioning that only metallic materials are considered.

The fitting of flow stress was done using equation (1) for the original and normalized sample data sets separately for $z = \ln\sigma$. The accuracy of the fitting is measured using the coefficient of determination ($R^2$) and Absolute Average Relative Error (denoted by $A_r$) [21]. The values of $Q$ and $Q'$ are calculated using equations (3) and (7), respectively.

To check for a possible mathematical relationship, the values of $Q$ for all sample data sets are plotted against the corresponding slopes $m$ (figure 1(a) and $b$ (figure 1(b)). The scatter in both figures indicates that $Q$ cannot be expressed as a mathematical function of either $m$ or $b$.

Figure 2 shows $Q'$ as a function of $m'$ (figure 2(a) and $b'$ (figure 2(a)) for three forms of flow stress. The nature of variations in $Q'$ with $m'$ and $b'$ indicates a possibility of an exponential relationship; to confirm, the values of $Q'$ are fitted with $m'$ and $b'$ using the following exponential relationship and plotted as solid lines (red curves) in figure 2.

It can be observed that the value of $Q'$ decreases gradually with the increase in $m'$ and tends to reach a saturation value for higher values of $m'$. On the other hand, the value of $Q'$ increases with the increase in $b'$, approaching a saturation value for larger values of $b'$. The general expression for the variation of $Q'$ with $m'$ and $b'$ can be written as:

$$Q' = Q'_0 + a_1 \exp(a_2 \alpha') \tag{8}$$

Here, $\alpha'$ is either $m'$ or $b'$, and $Q'_0$, $a_1$, and $a_2$ are constants. The specific fitting equations for the above model are:

$$Q' = -1.21 + 56.74\exp(-3.55m') \tag{9}$$

$$Q' = -1.26 + 1.67\exp(3.53b') \tag{10}$$

21

OPEN ACCESS
IOP Publishing
Journal of Physics: Condensed Matter
J. Phys.: Condens. Matter **36** (2024) 425702 (6pp)
https://doi.org/10.1088/1361-648X/ad5e52

# Novel ground state structures of N-doped $LuH_3$

**Ashok K Verma**[1,2,*], **Ajay K Mishra**[1,2] **and P Modak**[1,2]

[1] High Pressure and Synchrotron Radiation Physics Division, Bhabha Atomic Research Centre, Trombay, Mumbai 400085, India
[2] Homi Bhabha National Institute, Anushaktinagar, Mumbai 400094, India

E-mail: hpps@barc.gov.in

Received 26 March 2024, revised 28 May 2024
Accepted for publication 1 July 2024
Published 19 July 2024

**Abstract**

*Ab-initio* crystal structure searches have played a pivotal role in recent discoveries of high-Tc hydride superconductors under high pressure. Using evolutionary crystal searches, we predict novel ground state structures of N-doped $LuH_3$ at ambient conditions. We find an insulating ground state structure for $LuN_{0.125}H_{2.875}$ (~1.0 wt.% N), contrary to earlier studies where assumed structures were all metallic. This insulating behavior of ground state was found to persist up to ~45 GPa. However our crystal structure searches revealed a metallic state for an H-deficient variant of $LuN_{0.125}H_{2.875}$. We study bonding characteristics of important structures by calculating electronic density of states, electronic-localization functions and Bader charges. Our Bader charge analysis shows that insulators have both $H^+$ and $H^-$ ions whereas metals have only $H^-$ ions. We find that $H^+$ ions are bonded to N atoms *via* a very short covalent bond. Thus we identify a clear relationship between formation of N–H bonds and insulating behavior of materials. Besides this, we perform crystal structure searches for three more compositions with higher N-content (>1.0 wt.%). Analysis of electronic properties shows that the ground states of these compositions are insulator.

Supplementary material for this article is available online

Keywords: crystal structure search, electronic structure, density functional simulations, hydride superconductors

## 1. Introduction

The search for room conditions conventional superconductors has gained tremendous impetus in recent years after a bunch of important discoveries of high temperature superconductivity at megabar pressures (100 GPa = 1.0 Megabar), in diamond-anvil cell (DAC) experiments, in H-rich materials such as $SH_3$ (Tc = 203 K at 150 GPa) [1], $LaH_{10}$ (Tc = 260 K at 188 GPa) [2, 3], $CaH_6$ (Tc = 215 K, at 172 GPa) [4] and $ThH_{10}$ (Tc = 161 K, at 175 GPa) [5] etc. In these discoveries, density functional theory (DFT) based crystal structure searches have played central role as most of the superconductors were synthesized after theoretical predictions [6–9]. However the requirement of megabar pressure is a major obstacle in producing materials in bulk amount limiting real life applications of these superconductors. Thus reduction of synthesis pressure is a major thrust area of metal-hydride research. Towards this, a recent experimental study has presented evidences of near-ambient conditions superconductivity in an N-doped lutetium tri-hydride sample, which was recoverable at ambient conditions [10]. This result was not only startling and hotly debated but it has also stimulated several groups to repeat the experiment and perform DFT based calculations. So far

* Author to whom any correspondence should be addressed.

most of the experiments, except [11]. Where some evidences of superconductivity were reported, have failed to reproduce the superconductivity [12–18] and DFT based calculations [19–27] also could not explain the observed superconductivity by using conventional mechanism.

It has been reported [10] that superconducting material has an underlying face-centered cubic (fcc) $LuH_3$ lattice with ∼1.0 wt.% N-doping possibly at tetrahedral sites [19]. Subsequent experimental studies indicated that the superconducting material has $LuH_2$ framework [11, 12]. It is worthwhile to note that $LuH_2$ crystalizes in a metallic fcc ($Fm\bar{3}m$) lattice at ambient conditions whereas $LuH_3$ forms in an insulating rhombohedral lattice ($P\bar{3}c1$) [28]. However on compression, rhombohedral $LuH_3$ transforms into an fcc $LuH_3$ at ∼12 GPa which is recoverable at ambient conditions [28]. Based on experimental inputs, a recent DFT based work investigated N-doping at different sites in fcc matrix of $LuH_3$ with stoichiometry $LuN_{0.125}H_{2.875}$ [19]. This study probed tuning of electronic features like flat bands and van–Hove singularities close to the Fermi-level by N-doping at multiple sites and identified possible N sites which could result near-ambient conditions superconductivity in Lu–N–H system. In another DFT calculations, the effect of N-doping was studied by taking two compositions namely; Lu $N_{0.250}H_{2.750}$ (∼1.9 wt.% N) and $LuN_{0.125}H_{2.875}$ (∼1.0 wt.% N) [20]. While N-doing supported stabilization of fcc $LuH_3$ at low pressures, both compositions exhibited large imaginary phonon frequencies. By creating two H vacancies authors succeeded to eliminate the phonon instabilities but resulting $LuN_{0.125}H_{2.625}$ composition was not found to support superconductivity.

To the best of our knowledge, ground state structure of N-doped $LuH_3$ is not fully known at lower N concentrations. With this motivation, we adopt a multipronged approach to understand the composition, crystal structure and electronic properties of the N-doped $LuH_3$ with varying N weight percentage. First we carried out systematic evolutionary crystal structure search by varying N percentage from $\sim 1-2$ wt.% in $LuH_3$ which is achieved by fixing the compositions as $LuN_{0.125}H_{2.875}$ (∼1.0 wt.% N), $LuN_{0.167}H_{2.833}$ (∼1.3 wt.% N), $LuN_{0.200}H_{2.800}$ (∼1.6 wt.% N) and $LuN_{0.250}H_{2.750}$ (∼2.0 wt.% N). This methodology of crystal structure search has been successfully used in several diverse materials under high pressure conditions [29–33]. Energetics and electronic properties of the lowest enthalpy structures are studied and compared in great details. Our study show that ground state structure of $LuN_{0.125}H_{2.875}$ is an insulator at ambient pressure and this insulating behavior persists up to 45 GPa. Additionally, we have considered the effect of one H-vacancy in the $LuN_{0.125}H_{2.875}$ and the lowest enthalpy structure is obtained through crystal structure search. Other extreme of compositions are also explored, where H-deficient and N-excess structures are searched in Lu–N–H system. From this point of view, systematic variable composition crystal structure search is performed which resulted, besides the earlier predicted structures, a new ternary hydride $Lu_7N_6H$ on convex hull. This compound is akin to a rocksalt structure consisting of 7 units of LuN where one of the N atoms is replaced by H. Lastly, a new dynamically stable hexagonal structure is proposed for $LuH_3$ at ambient pressure.

## 2. Computational methodology

We performed *ab-initio* calculations within the framework of DFT using projector augmented wave (PAW) method [34] and Perdew–Burke–Ernzerhof (PBE) exchange-correlation functional [35] as implemented in the Vienna *Ab-initio* Simulation Package [36–38]. All crystal structure searches were carried out using USPEX code [39–41] in combination with *ab-initio* calculations. First generation structures were created randomly at a fixed density and obtained crystal structures were then fully relaxed at chosen pressure. Initial population was taken 10–90 depending upon the total number of atoms in unit cell. Generally, structural evolutions were allowed up to 10–20 generations. Obtained best crystal structures were fully re-relaxed by setting better plane-wave energy cutoff and denser ***k***-points meshes. For structure searches plane-wave basis set was constructed using a 500 eV energy cutoff and Brillouin zone was sampled using Monkhorst–Pack method [42] with a grid spacing of $2\pi \times 0.06$ Å$^{-1}$. For re-relaxation of the obtained best structures, plane-wave basis set energy cutoff energy was increased to 600 eV whereas reciprocal space integrations were carried out with a finer grid spacing of $2\pi \times 0.03$ Å$^{-1}$. Ionic positions were relaxed until forces on them became smaller than a value of 5.0 meVÅ$^{-1}$. Selected computational parameters insured the convergence of total energies better than 1.0 meV per atom. Static enthalpy convex hull calculations were carried by taking $P6_3/mmc$-Lu, $Pa\bar{3}$-N and $P6_3/mmc$-H phases, similar to earlier study [20]. All electron frozen-core PAW potentials were used with Lu ($6s^2$, $5d^1$, $5p^6$), N ($2s^2$, $2p^3$), and H ($1s^1$) valence configurations. It is to be noted that same PAW potentials were applied in earlier study on Lu–N–H system [20]. Crystal structures were rendered using VESTA software [43].

## 3. Results and discussion

We begin our study by searching the lowest enthalpy crystal structures, at 0 and 25 GPa, for $LuN_{0.125}H_{2.875}$ taking 32-atom unit cells (8 Lu, 1 N and 23 H atoms). Within a few generations, our searches find an fcc lattice as one of the important structure. This fcc structure is identical to that reported, as one of the lowest energy phase '*A*' at 0 GPa, in a recent study [19]. Figure 1 shows computed static enthalpies, relative to fcc structure, of the most important crystal structures obtained in our searches. Clearly the trigonal structure, with space group $P3$, is the lowest enthalpy structure at 0 GPa. Thus trigonal structure represents the true ground state and it has around 50 and 100 meV/atom lower enthalpy than that of orthorhombic $P2_12_12$ and fcc structures, respectively as reported in earlier study [19]. Our convex hull calculations show that enthalpy of trigonal structure is very close to convex hull, indicating a strong possibility of its formation in DAC experiments at low pressure conditions (see, table 1).

22

Jinst

PUBLISHED BY IOP PUBLISHING FOR SISSA MEDIALAB

RECEIVED: *December 25, 2023*
REVISED: *March 19, 2024*
ACCEPTED: *March 19, 2024*
PUBLISHED: *June 4, 2024*

# Performance assessment of a newly developed non-invasive 2D beam profile monitor for high-intensity accelerators

**Sherry Rosily**[a,b,*], **Hari Prasad M**[c], **Biswaranjan Dikshit**[a,d], **Srinivas Krishnagopal**[a,b] **and Rajesh Kumar**[a,b]

[a] *Homi Bhabha National Institute, Mumbai, India*
[b] *Ion Accelerator Development Division, Bhabha Atomic Research Centre, Mumbai, India*
[c] *Reactor Safety Division, Bhabha Atomic Research Centre, Mumbai, India*
[d] *Beam Technology Development Group, Bhabha Atomic Research Centre, Mumbai, India*

*E-mail:* sherry@barc.gov.in

ABSTRACT: In high-intensity accelerators, minimizing beam loss is paramount to avoid damages and activation of accelerator components. To achieve this, a reliable beam profile monitor is essential for assessing the beam center and spread. Additionally, the beam profile can be used to steer the beam during regular operation, thus reducing beam loss. In cases of irregular events, the monitor can initiate beam profile recording to identify and address any issues promptly. In this manuscript, we present a detailed description of a non-invasive 2D beam profile monitor, focusing on its components, operation, and most importantly, its reliability and failure modes. From operation experience, failure modes of the system and its effects were identified. Fault tree analysis was carried out. Failure rate of sheet generator was estimated using response surface method. Failure rates of components were used to estimate the failure rate of the system. From the target reliability, the required maximum repair time of the system was calculated.

KEYWORDS: Accelerator Subsystems and Technologies; Beam-line instrumentation (beam position and profile monitors, beam-intensity monitors, bunch length monitors)

*Corresponding author.



https://doi.org/10.1088/1748-0221/19/06/P06001

## Contents



## 1 Introduction

High-intensity proton accelerators are crucial components in accelerator-driven sub-critical systems (ADS, which are designed for various applications, including nuclear waste transmutation and neutron production. ADS is a sub-critical reactor which is driven by a spallation neutron source) [1, 2]. The additional neutrons required by the sub-critical reactor to continue operation is generated by the interaction of a high energy (~ 1 GeV) proton beam produced by a high intensity (typically currents of 10s of mA [2]) particle accelerator with a suitable target (typically Pb-Bi eutectic target [2]) and are called spallation neutrons. One of the challenges in ADS is the requirement of a reliable particle accelerator that provides a high intensity proton beam. Disruption in the beam can lead to reactor down time. It can also cause thermal stress in the components of the reactor [3].

A 1 GeV 10 mA proton accelerator, being developed for the Indian ADS program, will consist of number of energy stages [2]. The current plan of the 1 GeV accelerator program is shown in figure 1. The proton beam is first generated in an ion source and transported to multiple accelerator components. The transport sections consist of diagnostic and control instruments that guide and match the beam from one accelerating section output to the next stage. These instruments also ensure that the high power beam does not interact with the beamline material as it can cause thermal damage and radio-activation [4, 5]. The entire beam path is also maintained in ultra high vacuum to ensure minimise beam loss due to interaction with molecules in the path.

A beam profile monitor can provide essential information about the beam's centre and spread, enabling operators to make real-time adjustments to reduce beam loss during regular operation.

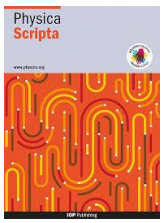



IOP Publishing Phys. Scr. 99 (2024) 085312 https://doi.org/10.1088/1402-4896/ad65c1

Physica Scripta

PAPER

# Phase space reconstruction technique for beam optimization in the Low Energy High Intensity Proton Accelerator (LEHIPA)

**Pallavi Priyadarshini**[1,2], **Jose V Mathew**[1,2], **Deepak N Mathad**[1] and **Rajesh Kumar**[1,2]

[1] Ion Accelerator Development Division, Bhabha Atomic Research Centre, Mumbai - 400085, India
[2] Homi Bhabha National Institute, Mumbai - 400094, India

**E-mail:** pallavip@barc.gov.in

**Keywords:** linear accelerator, proton accelerator, computed tomography, beam dynamics, LEHIPA, phase space reconstruction, beam profile measurements

OPEN ACCESS

RECEIVED
21 May 2024

REVISED
5 July 2024

ACCEPTED FOR PUBLICATION
19 July 2024

PUBLISHED
31 July 2024



## Abstract

The Low Energy High Intensity Proton Accelerator (LEHIPA) has been commissioned to the design energy of 20 MeV at BARC, India. The low energy beam transport (LEBT) channel of LEHIPA consists of two solenoids and drift spaces for matching the 50 keV proton beam from the ECR ion source (ECR-IS) to the RFQ. The ion beam extracted from the ECR-IS also contains molecular species like $H_2^+$ and $H_3^+$. Proton fraction in the beam is found to degrade slowly with time due to surface contamination of the plasma chamber and this reduction in proton beam current has implications for longitudinal and transverse beam dynamics. Hence, it becomes important to characterise the beam at different proton fraction levels to understand the end-to-end beam dynamics of LEHIPA. Computed Tomography (CT) technique has been used for the beam phase-space reconstruction in LEHIPA, using a Python program, incorporating the feature of filtering secondary species from the beam profiles measured using slit scanners in the LEBT. Simultaneous Algebraic Reconstruction Technique (SART) is used in the reconstruction since it is identified to be a better technique for a limited number of projections. The reconstruction program is benchmarked with the TraceWin beam dynamics code and implemented on the measured beam profiles to recreate the phase space distribution at the beginning of LEBT. Further, the tomographic reconstruction method is compared with the solenoid scan method and the rms emittance values are found to be in good agreement. The measured tomographic phase space distribution has then been used as TraceWin input for LEHIPA end-end beam dynamics simulations and the LEHIPA beam line parameters are re-optimized for minimum beam emittance growth. This paper presents the simulations of CT technique, benchmarking simulations with TraceWin, phase space reconstruction with measured beam profiles and beam dynamics studies of LEHIPA using the reconstructed beam distributions.

## 1. Introduction

As the demand for high-intensity proton accelerators continues to rise due to their diverse applications in fields such as energy production, nuclear waste transmutation, neutrino production, Thorium utilization, and more, numerous initiatives are being taken globally to advance their design and development. In India, at the Bhabha Atomic Research Centre (BARC) a 1 GeV, 10 mA proton accelerator for an Accelerator Driven Subcritical (ADS) system has been proposed [1, 2]. The frontend of the ADS accelerator, 20 MeV Low Energy High Intensity Proton Accelerator (LEHIPA) has been developed at BARC [3]. LEHIPA consists of a 50 keV ECR ion source, a 4 m long, 3 MeV, 352 MHz Radio Frequency Quadrupole (RFQ), followed by a 12 m long, 20 MeV, Drift Tube Linac (DTL) [1–8]. Recently, LEHIPA has been commissioned to the target energy of 20 MeV and peak current of 2 mA [3, 6]. The acceleration was carried out in successive stages, starting with an initial acceleration of 3 MeV in the Radio Frequency Quadrupole (RFQ), followed by subsequent accelerations of 6.8 MeV in DTL Tank 1, 11 MeV in DTL Tank 2, and ultimately reaching 20 MeV through DTL Tanks 3 and 4. [3–8]. At each stage of

commissioning, the beam dynamics simulations with the measured beam parameters proved to be very helpful. Beam dynamics and matching channels were re-optimised based on the measured beam parameters [9].

The LEHIPA ECR-IS is a 50 keV, 15 mA proton source operating in pulsed as well as CW modes [10–13]. In proton ECR-ISs, apart from $H^+$ species, there is substantial contribution from molecular species like $H_2^+$ and $H_3^+$ [10, 13]. The usage of high secondary electron yield materials like Aluminium, Boron Nitride (BN) etc as plasma chamber wall material improves the proton fraction considerably to over 80% [13]. However, the proton fraction is found to degrade slowly with time because of surface contamination of the plasma chamber due to sputtering by the back streaming electrons. With the beam composition changing over time, it becomes important to characterise the beam at different proton fraction levels to understand the longitudinal and transverse beam dynamics. Since the RFQ is designed for a higher beam current, a reduction in the input beam current leads to filamentation in the longitudinal phase space and this has been experimentally observed in beam energy spread measurements at LEHIPA [7, 14, 15]. This phenomenon causes an increase in the longitudinal emittance and hence the medium energy beam transport (MEBT) line parameters, especially the double gap re-bunching cavity voltage, need to be re-optimized to reduce the longitudinal emittance growth. In addition, the re-optimization of LEBT solenoids and MEBT quadrupoles is required for transverse emittance control.

Standard techniques that are used to map the beam phase space are pepper pot, slit wire scan, Allison scanner etc [16–18]. Tomographic phase space reconstruction is an alternative technique which remains unique among these spacious measurement setups since it requires just a single wire/slit scanner in the beam transport line in combination with a magnetic focusing element like solenoid or quadrupole. Although the tomography method shares similarities with the solenoid/quadrupole scan method, there are notable distinctions between the two approaches. In the solenoid scan method, only the root mean square (rms) beam sizes are utilized and hence the phase space distribution cannot be generated [18–21]. In addition, this analysis uses a thin lens approximation for the solenoid magnet and hence the emittance values may be better than the actual. On the other hand, tomography incorporates complete beam profile information for different orientations without resorting to thin lens approximations. Tomographic technique has been used in LEHIPA LEBT to reconstruct the beam at the ECR-IS exit (or the LEBT entrance) using the beam profiles measured using a slit scanner.

In the field of medical imaging, tomographic reconstruction is widely used in computed tomography (CT) scans to create detailed 3D images of the human body [22–24]. Tomographic reconstruction is a powerful technique used to reconstruct a higher $n$-dimensional space from projections at a lower ($n$-1) dimension using the Radon transform. The ($n$-1) dimensional projection of an $n$-dimensional image as a function of viewing angle, $\theta$, is described by the Radon transformation [25–32]. The computed tomography is an attempt to achieve an inverse Radon transformation. The technique is modified for beam physics using the Fourier slice theorem [29–32] and by scaling the spatial profile to make it comparable to the Radon transform. McKee *et al* and others [20, 32, 33] had used this technique to reconstruct phase-space with greater accuracy by combining CT with quadrupole scanning. Further, this technique has been successfully used in combination with the solenoid scan to characterise electron beams [29–31, 34].

The use of CT in the characterisation of proton beam is still not very popular except for few works at higher beam energies ($>$ 3 MeV) [35, 36], even though the technique in itself does not depend on the beam species and energies. At lower energies, especially in low energy beam transport lines (LEBTs), there can be difficulty in separating proton from other unwanted molecular species from the ion source. In this work, tomographic phase-space reconstruction from 1D beam profiles using a Python [37] based computer program, incorporating the feature of filtering the secondary species from the beam profiles is presented. To ascertain the accuracy of the code, comparison is done with known distribution from the beam dynamics code TraceWin [38] and the reconstructed distribution using the CT technique. Further, the phase-space distribution has been reconstructed at the entrance of LEBT and the rms emittance has been compared with the solenoid scan method [39, 40]. The measured tomographic phase space distributions have then been used as the input in TraceWin for LEHIPA end-end beam dynamics simulations, to compare with the LEHIPA design simulations. Based on the beam dynamics studies with measured beam distributions, LEHIPA beam line parameters have been re-optimized for maximum beam transmission and minimum beam emittance growth. Thus, the complete analysis of coupling beam diagnostic measurements with the beam dynamics simulations to identify areas of beam degradation and optimizing beam parameters to improve accelerator performance is presented in this paper.

This paper is arranged as follows. Section 2 details tomographic reconstruction techniques where the comparison of Simultaneous Algebraic Reconstruction Technique (SART) & Filtered Back-Projection (FBP) are studied. Further, benchmarking of the SART reconstruction program using TraceWin has been explained in section 3. The beam experiments in LEHIPA, filtering of secondary ion species & SART reconstruction at the beginning of LEHIPA LEBT has been explained in section 4. The reconstructed beam is used as TraceWin input and comparison of rms beam size at the slit scanner position with the measured beam size has also been shown in section 4. Section 5 details the comparison of the reconstructed beam with the solenoid scan method. In

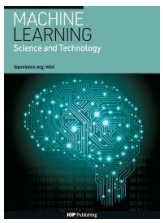

24

IOP Publishing Mach. Learn.: Sci. Technol. 5 (2024) 045007 https://doi.org/10.1088/2632-2153/ad8061

MACHINE LEARNING
Science and Technology

PAPER

# Prediction of flow stress of Ta–W alloys using machine learning

A Kedharnath[1,2], Rajeev Kapoor[1,2,*] and Apu Sarkar[1,2]

[1] Mechanical Metallurgy Division, Bhabha Atomic Research Centre, Mumbai 400085, India
[2] Division of Engineering Sciences, Homi Bhabha National Institute, Anushaktinagar, Mumbai 400094, India
[*] Author to whom any correspondence should be addressed.

**E-mail:** rkapoor@barc.gov.in

**Keywords:** machine learning, XGBoost, SHAP, mechanical threshold stress, stress–strain prediction

Supplementary material for this article is available online

OPEN ACCESS

RECEIVED
28 September 2023

REVISED
5 September 2024

ACCEPTED FOR PUBLICATION
26 September 2024

PUBLISHED
8 October 2024



## Abstract

The primary aim of this article was to predict the flow stress of Ta–W alloys using the eXtreme Gradient Boosting (XGBoost) machine learning model and to explain the outcome using SHapley Additive exPlanations (SHAP). The article details the effect of temperature, strain rate, and alloying content on the deformation behavior. Though grain size, dislocation density, texture and impurities are also important factors affecting the deformation behavior, these have not been considered in this work. Data and constitutive models from the literature were used to find and compare the predictiveness of the flow stress in Ta–W alloys. XGBoost predicted flow stress with a root mean square error of 12 MPa during training and 40 MPa during testing, while constitutive models such as Johnson–Cook (JC), Zerilli–Armstrong (ZA) and mechanical threshold stress (MTS) models showed a root mean square error of 208, 131 and 149 MPa respectively. The linear correlation between the predicted and experimental flow stress at 10% strain was calculated using the Pearson correlation coefficient and found to be 0.64, 0.93, and 0.70 for JC, ZA and MTS models respectively, while XGBoost showed 0.99 during training and 0.98 during testing. The optimized XGBoost model was validated using five-fold and leave-one-group-out cross-validations. The flow stress at 10% strain was predicted using XGBoost at various temperatures, strain rates, and alloying content. The flow stress was low at temperatures above 1000 K and strain rates below $10^{-2}$ $s^{-1}$. From SHAP analysis, it was found that the base flow stress value (at which the SHAP value is zero) was 477 MPa. For temperatures less than 275 K, strain rates greater than 1 $s^{-1}$, and alloying content greater than 2.5 wt.% W, the flow stress showed an increase from its base value.

## 1. Introduction

Tantalum (Ta) and its alloys are used in electronics, medical [1, 2], nuclear [3–9], aerospace [5] and defence [1, 10] applications for their excellent properties such as corrosion resistance [1, 5, 11–13], biocompatibility [1, 2], resistance to grain growth at elevated temperatures [1, 14, 15], and good ductility at low temperatures. The list of main/relevant findings/uses of Ta and its alloys is given in table S1 in the supplementary document S1. Ta alloyed with other refractory metals has shown a significant increase in the thermal and mechanical properties at elevated temperatures [14, 16, 17]. Though Ta is bcc, it does not exhibit ductile to brittle transition [1, 11–13]. Researchers have studied the deformation behavior of as-cast and processed Ta during various manufacturing routes. Experimental testing over a wide range of parameters is time consuming and costly, hence modeling and simulation approaches are being used to predict the mechanical behavior of materials. Mathematical models and constitutive equations help as a base for understanding and are used in simulations. One-dimensional models were formulated during the late 1980s [18, 19]. Later, one-dimensional stress–strain models were replaced by their equivalent three-dimensional models [20]. However, these models did not express the effects of temperature and strain rate on the flow stress. Milella presented a model based on experimental evidence to show the effects of temperature and strain rate on flow stress [21]. The Zerilli–Armstrong (ZA) model [22–24] could not predict the behavior at high temperatures

IOP Publishing Mach. Learn.: Sci. Technol. 5 (2024) 045007 A Kedharnath et al

and strain rates. Models that incorporate high strain rates help study ballistic materials, damage and accidental events on structural materials. Nemat-Nasser *et al* used split-Hopkinson bar experimental results to model Ta and Ta–tungsten (W) deformation behavior at high strain rates [25–27]. Microstructural based models by Voyiadjis and Abed [28] considered dislocation density evolution and their effect on the deformation behavior for a wide range of temperatures and strain rates. The mechanistic models reviewed above lack predictiveness over a broad range of test conditions. Models based on artificial intelligence have been used by the researchers to overcome this problem. Lin *et al* used a deep belief network [29] and a stacked auto-encoder (SAE) network [30] to predict the deformation of Ni-based alloys for a wide range of temperatures and strain rates. Pang *et al* used a reliable SAE model to demonstrate the nonlinear relationship between the flow stress and deformation parameters in Ti alloy [31]. Zhang *et al* used neural networks (NN) and finite element method (FEM) to learn the constitutive relations in plasticity [32]. Weber *et al* used constrained NN and FEM for hyperelastic material modeling to overcome the disadvantages of a small number of samples and noisy data [33]. Frankel *et al* showed the efficiency of NN over crystal plasticity (CP) in predicting the evolution of the stress field of polycrystals [34]. Jung *et al* used NN potentials in molecular dynamics (MD) simulations for studying crack dynamics [35]. Kedharnath *et al* used a random forest (RF) algorithm on MD simulation results to correlate the MD and slip transmission parameters with yield stress [36]. Melching *et al* used generative adversarial networks with a physics-guided discriminator to generate artificial data of cracked specimens which matched well with the experimental digital image correlation results [37]. Manti *et al* combined symbolic regression and discrete exterior calculus to study two-dimensional elasticity problems [38]. Rezasefat and Hogan used convolutional NN and FEM to predict stress concentration around inclusion [39]. Huang *et al* used MD data to train the RF model to predict the tensile stress of natural rubber [40]. These recent works by the researchers were based on NN and RF type of machine learning (ML) models to study the deformation of materials. These ML models were dependent on both experimental and simulation data for training and testing. Simulation techniques such as MD, CP, and FEM were used for data generation. Dornheim *et al* summarized the results and challenges of NN-based constitutive models and listed interpretability, countering error accumulation, and measuring prediction quality as few challenges [41]. This work uses the explainability and generalization efficiency of the recent ML models to increase the interpretability and predictiveness of the deformation behavior.

The aim of this article was to predict the flow stress in Ta–W alloys, given the inputs of strain, alloying content, temperature and strain rate, using ML tools such as eXtreme Gradient Boosting (XGBoost) [42] and SHapley Additive exPlanations (SHAP) [43], and to bring out the relative importance of the input parameters on the flow stress. The effects of input parameters on the flow stress as reported in the literature, have been detailed and the stress–strain data from the literature have been compiled in section 2. Other input parameters such as grain size, dislocation density, texture and impurities, that are also important, have not been considered in this work due to lack of literature data incorporating all the parameters. As a precursor to the aim, the literature data were used in the constitutive models—Johnson–Cook (JC), ZA, and mechanical threshold stress (MTS) to study their predictiveness of the flow stress as shown in section 3. The data from the literature are represented with symbols, colors, and numbers in table 1 which will be used for ease of visualization in the upcoming figures.

## 2. Deformation behavior

### 2.1. Effect of temperature

In general, strength decreases with increase in temperature. Below 0.1 $T_m$ (i.e. 575 K), the decrease in the flow stress with an increase in temperature is because of the inherent lattice friction of the bcc structure defined by the Peierls stress of the material [17, 19, 62]. The classical model of the deformation of bcc metals at low homologous temperatures is the nucleation and propagation of double kinks [14, 63]. At low temperatures, the higher value of Peierls stress for screw dislocations as compared to edge dislocations favors the formation of double kinks [14]. BCC metals predominantly have screw dislocations which also favors the formation of double kinks. At high temperature, the difference in the Peierls stress between the screw and edge dislocations reduces, thereby enhancing the mobility of dislocations and their interactions. Ta has good resistance to grain growth at high temperatures [14, 15]. Dislocation interactions and recovery mechanisms which are temperature-dependent are prominently seen to affect mechanical behavior [58]. This is because the Peierls stress is a function of temperature and shear modulus, and any change in the shear modulus due to temperature change or alloy addition will change the Peierls stress. The shear modulus $\mu_T$ at the test temperature $T$ is given by,

$$\mu_T = \mu_0 - \frac{D_\mu}{\exp\left(\frac{T_0}{T}\right) - 1}, \tag{1}$$

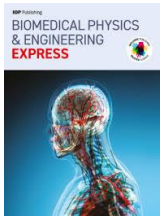


25

IOP Publishing Biomed. Phys. Eng. Express 10 (2024) 045059 https://doi.org/10.1088/2057-1976/ad57ce

Biomedical Physics & Engineering Express

PAPER

# Radiation-induced DNA damage by proton, helium and carbon ions in human fibroblast cell: Geant4-DNA and MCDS-based study

**Arghya Chattaraj**[1,2] **and T Palani Selvam**[1,2]

[1] Radiological Physics and Advisory Division, Health, Safety and Environment Group, Bhabha Atomic Research Centre, Mumbai, 400085, India
[2] Homi Bhabha National Institute, Anushaktinagar, Mumbai, 400094, India

**E-mail:** pselvam@barc.gov.in

**Keywords:** DNA-damage, Monte Carlo, proton, helium and carbon ions, SSB, DSB, cDSB

OPEN ACCESS

RECEIVED
25 January 2024

REVISED
28 May 2024

ACCEPTED FOR PUBLICATION
13 June 2024

PUBLISHED
28 June 2024



## Abstract

*Background*. Radiation-induced DNA damages such as Single Strand Break (SSB), Double Strand Break (DSB) and Complex DSB (cDSB) are critical aspects of radiobiology with implications in radiotherapy and radiation protection applications. *Materials and Methods*. This study presents a thorough investigation into the effects of protons (0.1–100 MeV/u), helium ions (0.13–100 MeV/u) and carbon ions (0.5–480 MeV/u) on DNA of human fibroblast cells using Geant4-DNA track structure code coupled with DBSCAN algorithm and Monte Carlo Damage Simulations (MCDS) code. Geant4-DNA-based simulations consider 1 $\mu$m $\times$ 1 $\mu$m $\times$ 0.5 $\mu$m water box as the target to calculate energy deposition on event-by-event basis and the three-dimensional coordinates of the interaction location, and then DBSCAN algorithm is used to calculate yields of SSB, DSB and cDSB in human fibroblast cell. The study investigated the influence of Linear Energy Transfer (LET) of protons, helium ions and carbon ions on the yields of DNA damages. Influence of cellular oxygenation on DNA damage patterns is investigated using MCDS code. *Results*. The study shows that DSB and SSB yields are influenced by the LET of the particles, with distinct trends observed for different particles. The cellular oxygenation is a key factor, with anoxic cells exhibiting reduced SSB and DSB yields, underscoring the intricate relationship between cellular oxygen levels and DNA damage. The study introduced DSB/SSB ratio as an informative metric for evaluating the severity of radiation-induced DNA damage, particularly in higher LET regions. *Conclusions*. The study highlights the importance of considering particle type, LET, and cellular oxygenation in assessing the biological effects of ionizing radiation.

## Introduction

Recent research has placed a significant focus on the impact of ionizing particles on living cells, with applications spanning the medical field, particularly in cancer treatment through radiotherapy, as well as in space science and radioprotection for astronauts(Francis and Stypczynska 2013, Lee 2017, Manalad 2022). When highly energetic particles traverse biological tissue, they can induce various effects, including excitations, ionizations, and alterations in molecules within the medium (Nickoloff *et al* 2020). Among these effects, the most critical modifications are believed to occur in the deoxyribonucleic acid (DNA), as this molecule governs cellular functions, and any changes to it can disrupt the cell cycle, leading to cell death. Typically, endogenously induced lesions are evenly distributed throughout the cell, whereas clustered damage sites, characterized by the presence of multiple damage events in close proximity, are a characteristic feature of ionizing radiation (Lomax *et al* 2013). Upon detecting DNA damage, cells initiate repair processes. However, the effectiveness of these repair mechanisms is heavily dependent on the type of damage and the complexity of the damage pattern. Notably, repair processes take place within the cell nucleus following irradiation, assuming that single-strand breaks (SSBs) can be repaired (Chapman *et al* 2012). Repairing double-strand breaks (DSBs) is a more challenging task, and the repair of complex damages, characterized by the presence of

more than two SSBs within a relatively small proximity, poses the greatest challenge for repair activities (Chapman *et al* 2012, Nickoloff *et al* 2020). The poor repair process of clustered DSBs (cDSB) at least in part, reflects inhibition of canonical NHEJ (nonhomologous end-joining) by short DNA fragments (Chapman *et al* 2012, Nickoloff *et al* 2020). This shifts repair toward HR (homologous recombination) and perhaps alternative NHEJ, and can result in chromothripsis-mediated genome instability or cell death (Nickoloff *et al* 2020). In various circumstances, the success of the repair process can vary, potentially leading to either successful restoration or, in some cases, an erroneous repair that results in mutations (Francis and Stypczynska 2013). Mutations are a significant concern as they can contribute to the development of long-term cancers or even lead to cell death. This aspect is particularly relevant in the context of radiotherapy, where the primary treatment itself can induce secondary cancers due to radio-induced mutations.

Currently, in therapeutic contexts, a widely used approximation relies on the linear quadratic (LQ) model, which has been extensively analysed by Brenner (Brenner *et al* 1998). This model approximates the cell death rate as being related to the energy delivered to the biological medium. However, the LQ model is constructed based on observations of cell survival following irradiation. As a result, it doesn't provide insight into the internal processes occurring within the cell or nucleus, nor does it offer information about the intricacies of cellular repair activities or the resulting DNA mutations (Brenner *et al* 1998). Furthermore, the predictions made by the LQ model may be limited to relatively short-term cellular responses, as its parameters are typically adjusted to match cell death within a specific time frame after irradiation (Brenner *et al* 1998). It's worth noting that the effects of radiation on the human body can manifest over an extended period, sometimes several years after the initial exposure. Therefore, to precisely quantify the effects of radiation on biological tissue and predict the resulting reactions, it is imperative to gain a detailed understanding of what transpires at the DNA level during irradiation and throughout the subsequent repair phase. This deeper insight can provide a more comprehensive and accurate assessment of the long-term consequences of radiation exposure.

Monte Carlo method is a powerful tool to model a particle's track as it traverses a target volume, while considering its interactions with the medium's molecules and yielding both the positions and the amount of energy deposition at each interaction point. Numerous analytical approaches are subsequently disseminated to gauge the ultimate impact of such a particle trajectory on cellular behaviour, including the probability of cell survival. One approach to investigate this matter involves investigating the yields of energy deposition clusters, which can give rise to complex DNA damage, often referred to as clustered lesions, proven to be fatal for the cell.

Several studies have been conducted to estimate the yields of DNA damages, shedding light on the nature and complexity of these lesions under different radiation conditions. Nikjoo *et al* (1998) analysed DNA damage utilizing the K-means algorithm. Garty *et al* (2010) conducted a study focusing on counting the number of interactions occurring inside small nanometer-sized cylinders ($\sim 3 - 8$ nm) randomly placed along the particle track. Friedland *et al* (2003) described the spatial coordinates of the whole genome inside a human cell and calculated proton induced DNA damage yields using PARTRAC code. Leloup *et al* (2005) measured yields of SSB and DSB after irradiating a plasmid DNA with 1.03, 19.3 and 249 MeV protons, 26 MeV helium nuclei and $\gamma$-rays ($^{137}$Cs or $^{60}$Co). Francis *et al* (2011b) focused on calculating DNA damage clusters resulting from proton irradiation in the energy range of 0.5 - 50 MeV. (Dos Santos *et al* 2013) conducted an evaluation of how chromatin density influences the formation of clustered damages caused by protons within the nuclei of fibroblast and endothelium cells in the G0/G1 phase. Villagrasa *et al* (2017) investigated the correlation between the number of radiation-induced DSB in DNA molecules and the probability of detecting nuclear foci after targeted microbeam irradiation of cells with protons (23 keV/$\mu$m) and alpha particles (37, 90, and 160 keV/$\mu$m). Francis *et al* (2011b), Dos Santos *et al* (2013) and Villagrasa *et al* (2017) used Geant4-DNA code coupled with adapted Density Based Spatial Clustering Algorithm with Noise (DBSCAN) algorithm. Friedland *et al* (2017) evaluated DNA damages induced by light ions (0.25–256 MeV/u) using PARTRAC track structure code. de la Fuente Rosales *et al* (2018) assessed the physical, pre-chemical, and chemical phases of damage to calculate the early DNA damage induced by protons (0.5–30 MeV) and $\alpha$-particles (2–10 MeV) in liquid water. Moeini *et al* (2020) focused on studying damage in the form of SSBs and DSBs by simulating the transportation of primary alpha particles (2–20 MeV) and the resulting secondary particles in liquid water using Geant4-DNA code. Mokari *et al* (2020) investigated direct and indirect DNA damage caused by electrons in the energy range of 0.011–100 keV using Geant4-DNA code. Sakata *et al* (2020) developed a Geant4-DNA based 'fully integrated' Monte Carlo simulation framework that calculates both early DNA damage and subsequent biological responses over time. This unique platform also incorporates a Biological repair model (Sakata *et al* 2020). Zhu *et al* (2020) quantified the proportion of proton-induced direct and indirect DNA damages in fibroblast cell nucleus using TOPAS-nBio code. The details on the physical and chemical processes responsible for DNA damage and the use of Geant4-DNA toolkit for simulating direct and indirect DNA damages are discussed by Bordeaux (2021). In a recent study by Hosseini *et al* (2022), they utilized the Geant4-DNA code and DNA PDB format to compute the damages caused by 0.1–20 MeV protons. Their investigation focused on

26

IOP Publishing J. Radiol. Prot. 44 (2024) 021511 https://doi.org/10.1088/1361-6498/ad42a5

Journal of Radiological Protection

OPEN ACCESS

RECEIVED
22 February 2024

REVISED
1 April 2024

ACCEPTED FOR PUBLICATION
24 April 2024

PUBLISHED
3 May 2024



PAPER

# Radiological complexity of nuclear facilities: an information complexity approach to workplace monitoring

**Abinash Chakraborty**[1,*], **Neeraj Parashar**[1], **Dhananjay Kumar Pandey**[1], **Pankaj Kumar**[1], **U V Deokar**[1], **J P N Pandey**[1] **and M S Kulkarni**[1,2]

[1] Health Physics Division, Bhabha Atomic Research Center, Mumbai 400085, India
[2] Homi Bhabha National Institute, Mumbai 400094, India
[*] Author to whom any correspondence should be addressed.

**E-mail:** chakabinash@gmail.com

**Keywords:** workplace monitoring, time series analysis, sample entropy, radiological complexity, entropy analysis of radiological readings

## Abstract

Nuclear energy is crucial for achieving net-zero carbon emissions. A big challenge in the nuclear sector is ensuring the safety of radiation workers and the environment, while being cost-effective. Workplace monitoring is key to protecting workers from risks of ionising radiation. Traditional monitoring involves radiological surveillance via installed radiation monitors, continuously recording measurements like radiation fields and airborne particulate radioactivity concentrations, especially where sudden radiation changes could significantly impact workers. However, this approach struggles to detect incremental changes over a long period of time in the radiological measurements of the facility. To address this limitation, we propose abstracting a nuclear facility as a complex system. We then quantify the information complexity of the facility's radiological measurements using an entropic metric. Our findings indicate that the inferences and interpretations from our abstraction have a firm basis for interpretation and can enhance current workplace monitoring systems. We suggest the implementation of a radiological complexity-based alarm system to complement existing radiation level-based systems. The abstraction synthesized here is independent of the type of nuclear facility, and hence is a general approach to workplace monitoring at a nuclear facility.

## 1. Introduction

During the 26th session of the United Nations Framework Convention on Climate Change (COP 26) in 2021, India set forth its ambitious target to achieve net zero carbon emissions by 2070 [1]. A pivotal aspect of realising this goal lies in the development of low-carbon electricity systems that are both cost-effective and scalable. Nuclear energy, with its low carbon footprint, aligns well with this imperative [2]. However, a significant challenge in the nuclear energy sector is the delicate balance between cost-effectiveness and the management of risks from ionising radiation. It is crucial to assess and mitigate the risks associated with ionising radiation without overly compromising the contributions of nuclear energy to sustainable development.

The International Atomic Energy Agency (IAEA) is the international statutory body dedicated to establishing safety standards for radiological protection and minimising the risks posed by ionising radiation. Occupational exposure to ionising radiation can occur across a spectrum of sectors including industries, medical institutions, educational and research establishments, and nuclear fuel cycle facilities. Ensuring appropriate levels of radiation protection for workers is fundamental for the safe and justified use of radiation, radioactive material, and nuclear energy.

Over the years, with improvements in radiation protection practices, the radiation exposures and consequently the risk from ionising radiation to workers and the public, have become well-controlled. For

IOP Publishing J. Radiol. Prot. 44 (2024) 021511 A Chakraborty et al

perspective, the average annual effective dose to occupational workers at nuclear reactors across the world between 2010–2014 was 0.5 mSv, compared to 4.1 mSv between 1975–79 [3].

Workplace monitoring forms an integral part of radiation protection program to control exposures to workers at a nuclear facility. According to general safety guidelines on occupational radiation protection [4], the frequency of routine monitoring at a workplace should be commensurate with the occupancy factor of radiation workers in the location and the anticipated changes in the radiation environment. In scenarios where a sudden unexpected increase in radiation exposure might result in a significant radiation dose being received by a worker, provisions for continuous monitoring should be in place. The set of continuous monitors, which include both radiation field and airborne contamination monitors, is collectively referred to as the radiation monitoring systems (RMS).

Merely recording RMS measurement data as part of workplace monitoring is not adequate. It's imperative to analyse the trends in the measurement data to identify any deterioration of engineered safety controls or deviations from safe operating procedures (SOPs). This analysis can be initially performed by plotting the RMS data as multiple time series to observe its trend and by calculating statistics such as mean and variance. While it is relatively straightforward to identify non-decreasing trends in RMS measurement data, pinpointing gradual changes is non-trivial. Gradual changes are incremental changes in measurement data over a long period of time. These changes (which might stem from faults in shielding doors, deviations from safe operating protocols by human operators, or natural wear and tear of radioactive handling equipment) do not leave prominent signatures in the radiation measurement timeseries trends.

These gradual changes are influenced by multiple factors or components within a nuclear facility. Ideally, we could model the contribution of each of these factors to the change in radiological measurands, i.e. define a set of equations whose solution would describe the evolution of radiological parameters over time. These evolution functions $f_x(t)$ could aid in identifying gradual changes in radiological measurands over time. However, the interplay of multiple components within the nuclear facility may render this exercise intractable.

To address this challenge, we propose an abstraction (viewing complex entities by focusing on their essential characteristics, rather than detailed, operational aspects) of a nuclear facility as a complex system. A complex system, broadly speaking, consists of a collection of interacting elements/components, which exhibit behaviour that cannot be simply expressed as the sum of behaviors of these interacting elements [5]. In the context of our abstraction, we have defined radiological complexity as the set of externalities which affect the radiological measurands in a nuclear facility (the system). These externalities (components) can be a set of processes through which a nuclear facility cycles through during the course of its normal operations; or it can refer to the fluctuations in the ventilation patterns; or it can refer to changes in the quality of shielding and other engineered safety measures which might lead to unintended escalation of radiation sources. The complexity of this abstracted system can be quantified using a suitable information theoretic entropy metric. In our abstraction, this entropy metric will encapsulate the amount of surprise that a radiological measurand has, given its history is known. The more the surprise, the more will be the entropy.

In this paper, we explore the abstraction of a nuclear facility as a complex system, and investigate if the study of radiological complexity of a nuclear facility can give us insights and interpretations relevant to radiological safety of occupational radiation workers.

## 2. Radiological complexity

Complex systems are everywhere, from ecosystems to economies to the internet, but defining what exactly makes a system 'complex' has proven to be elusive. In systems theory, a complex system is defined as a system consisting of many parts which have varying degrees of interactions which each other. These parts display collective behaviour, which is not reducible to individual parts [6]. This is also called emergent behaviour. Notable necessary conditions for complexity are time-dependence, interactions between parts, and unexpected behaviour [7]. Complex systems show efficient, robust, fragile phenomena arising from co-evolving networks and are adaptive, with path-dependent dynamics and statistics far from equilibrium [8, 9].

We propose the abstraction of nuclear facility as a complex system. In our abstraction, we define 'the system' as the collection of radiological measurands and the radioactive handling equipment (e.g. including pumps, transfer routes, etc) of location $l_i$ of the facility. The system could have also been used to refer to an entire facility. However, doing so might lead to loss of finer details.

Aligning with the key attributes of a complex system we define radiological complexity of a location $l_i$, $H_{l_i}$ within a nuclear facility **as the set of externalities that affect the radiological measurands of the location**. Radiological Complexity, is characterised by multiple interacting components, non-linear relationships, emergent behaviours and adaptability with time. Since these are the general characteristics of a complex

27

Published by IOP Publishing for Sissa Medialab

Received: *January 4, 2024*
Revised: *January 26, 2024*
Accepted: *January 27, 2024*
Published: *March 5, 2024*

# Suppression of multipacting growth in a superconducting spoke resonator by the use of higher order modes

**Alok Kumar Ghosh**[a,b,*] **and Vyaghri LS Rao Sista**[a]

[a] *Bhabha Atomic Research Centre, Mumbai 400085, India*
[b] *Homi Bhabha National Institute, Mumbai 400094, India*

*E-mail:* alokkr.ghosh20@gmail.com

Abstract: Multipacting is a vacuum discharge phenomenon that constrains the performance of accelerator structures and various microwave devices significantly. The different ways to mitigate multipacting discharge have been a central research goal in Accelerator Physics & Technologies for a prolonged period. In this work, both Monte-Carlo and particle-in-cell (PIC) simulations show that the multipactor avalanche can be mitigated, by the use of Higher Order Modes (HOMs). The intuition behind the approach of using HOMs to suppress multipacting has been explained first. Then, the multipacting suppression has been demonstrated in a simple 1-D metallic gap, when it is exposed to a second carrier frequency in addition to fundamental rf mode, with the help of a Monte-Carlo simulation code. Finally, a detailed PIC simulation has been carried out using CST Microwave studio, to investigate the effect of various HOMs on the multipactor growth in a superconducting spoke cavity. It is observed that a slight excitation of some particular modes can drastically diminish the multipactor growth. Simulation has been done first without any HOMs, to calculate the growth rate and also to spot the discharge location. Next, among various HOMs (more specifically, quadrupole modes), only those have been selected, whose magnetic field locations coincide with the multipacting prone zone of the cavity. In a simulation study, the presence of these preselected quadrupole modes has been found to exhibit a substantial suppression effect on the multipacting growth of the cavity.

Keywords: Accelerator modelling and simulations (multi-particle dynamics, single-particle dynamics); Accelerator Applications; Accelerator Subsystems and Technologies

*Corresponding author.



https://doi.org/10.1088/1748-0221/19/03/P03005

## Contents



## 1 Introduction

Multipacting is an effect of resonant RF discharge driven by secondary electron emission and, a ubiquitous phenomenon in a variety of scenarios, such as high-power RF devices, accelerator cavity structures, and satellite communication systems. It is one of the most severe problems encountered in the operation of superconducting accelerator structures. In multipacting a sheet-like cloud of electrons oscillates in synchronism with the electromagnetic field inside the cavity and impacts multiple times with the wall of the cavity thereby emitting secondary electrons continuously in regular time intervals.

Electron multipacting affects the superconducting cavity structures adversely in several ways. Multipacting generally takes place for some specific values of the accelerating fields inside the superconducting cavity if certain conditions are matched, in which the power fed to the cavity is eaten away by the oscillating electrons with a sharp fall of the Q-value. It seems like a barrier in the way of getting a more accelerating gradient. So, to set up the required energy gradient inside the cavity it takes days or weeks of RF conditioning of the cavity to overcome the multipacting barriers occurring at different field levels. In other words, electron multipacting plays the role of principal limitation in achieving the final energy content in the cavity. Moreover, the impact of the electrons on the cavity surface wall dumps heat, which also adds an extra cryogenic burden or may lead to quenching of the superconducting state. For these particular reasons, most of the research on multipacting has been concentrated on the means to mitigate it.

Endeavour to mitigate multipacting encompasses some special kind of treatments of the interior cavity surface, like deliberately roughening the surface or making some triangular or rectangular grooves to reduce the secondary emission yield (SEY) [1–3], modification of the component geometry in the immediate vicinity of the multipacting zone so as to change the local electromagnetic field and that way making it less susceptible to multipacting [3–7]. Another promising method to suppress the multipacting growth is introducing a dc magnetic bias to affect the motion of the multipacting electrons [7–9]. These techniques are suitable for normal conducting structures. In the case of superconducting cavity geometry modification is the only option to get rid of the severity of electron





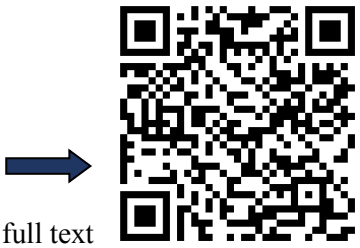

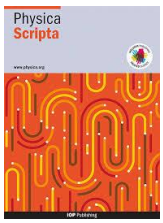

28

IOP Publishing Phys. Scr. 99 (2024) 125301 https://doi.org/10.1088/1402-4896/ad8978

Physica Scripta

PAPER

# Supression of shielding effect of large area field emitter cathode in radio frequency gun environment

A T Sathya[1], Shreya G Sarkar[2], R I Bakhtsingh[2] and Jayanta Mondal[2,3]

[1] Department of Physics, Indian Institute of Technology Roorkee, Uttarakhand, 247667, India
[2] Accelerator & Pulsed Power Division, Bhabha Atomic Research Centre, Mumbai, 400085, India
[3] Homi Bhabha National Institute, Mumbai, 400094, India

E-mail: shreyag@barc.gov.in

OPEN ACCESS

RECEIVED
7 August 2024

REVISED
10 October 2024

ACCEPTED FOR PUBLICATION
21 October 2024

PUBLISHED
4 November 2024



**Keywords:** field emission, shielding effect, large-area field emitters (LAFE), radio frequency (RF) guns, COMSOL simulation, field enhancement factor ($\gamma$)

## Abstract

Utilisation of large area field emitters (LAFE) cathodes for rf gun injector hold promise for delivering compact, high power and high brightness electron beam for advanced accelerator technologies. LAFEs subjected to DC electric fields posses significant challenges due to the shielding effect which restricts emission from central emitters and decreases the overall current density. Mitigating the shielding effect of LAFE in rf gun environment is essential for meeting the desired beam quality requirement in an accelerator. The current distribution of LAFE under DC conditions depend on its various geometrical parameters such as emitter height, inter-emitter distance, aspect ratio, number of emitters. Additionally, in rf gunsetup, LAFEs are subjected to variable macroscopic electric field at different emitter position which can potentially alter the current distribution compared to DC fields. In this work, we have systematically studied the shielding effect properties of LAFE in rf gun environment under the influence of various LAFE parameters. A semi-analytical approachhas been adopted to estimate the current distribution which combines the analytically calculated field enhancement factor ($\gamma$) and numerically calculated applied rf field values. This new methodology was first validated using COMSOL simulation and then employed for field emission performance estimation of a LAFE cathode integrated in a½ cell S-band (2856 MHz) rf gun. The simulation results reveals that under favourable conditions, a Gaussian spatial distribution of beam can be obtained from LAFE thus countering the shielding effect typical in DC fields. By optimizing the LAFE parameters, the desired current and beam distribution pattern can be achieved. This study highlights the adoption of a promising approach for designing LAFE cathodes suitable for rf gun which can lead to advancement of field emission technologies for accelerator-related applications.

## 1. Introduction

Field emission (FE) is a quantum mechanical process where electrons are emitted from a solid surface under the influence of a high electric field. Field emission-based devices have been utilized in various advanced technologies such as vacuum microelectronics [1, 2], field effect transistors [3], x-ray sources [4, 5], advanced microscopy [6] etc One of the emerging applications of field-emitting cathodes is related to electron beam source for electron accelerators [7–9]. Recently, progress has been made toward the development of FE cathode-based rf gun systems for several technologies such as high-power accelerators for industrial applications [10], high-brightness injectors for free-electron laser [11], and power-efficient, compact accelerators for space applications [12]. Radio Frequency (RF) gun injectors based on thermionic and photocathodes are already employed, but field emission sources can offer several advantages compared to conventional cathodes, such as high emission current [13], ultra-low emittance [14], cost-effectiveness [15], and compatibility with superconducting RF cavity environments [16].

Field emission predominantly occurs at the tips of high aspect ratio nanostructures [17–19]. These unique emitter geometries enhance the local electric field, enabling electron emission at moderately applied macroscopic fields. The field enhancement factor ($\gamma$), a critical figure of merit, quantifies the degree to which the local field is amplified at the emitter tip compared to the macroscopically applied field. Efficient, bright, and high-current electron sources demand the use of large-area field emitters (LAFEs) [20–22], which consist of numerous emission tips arranged either in an array or randomly. However, the technical challenge with LAFEs lies in the variation of enhancement factors across different emitting sites due to the shielding effect [23, 24]. The field enhancement factor ($\gamma$) is maximum at the periphery and minimum at the center, allowing the peripheral emitters to predominantly participate in field emission over the central emitters, thereby limiting the practically achievable current density. Consequently, the shielding effect of an LAFE subjected to direct current (DC) electric fields can significantly diminish the efficiency of field emission devices and introduce non-uniformity in the emitted current distribution.

For DC applications, various strategies such as patterning by lithography techniques [25, 26] and utilizing the anode proximity effect [27] have been adopted to decrease the deterimental effect of shielding. The shielding effect, which is mainly a geometrical effect, depends on various LAFE parameters such as inter-emitter distance, emitter height, aspect ratio, number of emitters, etc However, optimization of the performance of such an array of emitters is a difficult task [28, 29]. In recent years, analytical formulas based on line charge model (LCM) [30, 31] have been proposed for predicting the current distribution of LAFE subjected to DC fields. Analytical formulas [32] can predict the $\gamma$ value distribution for hemi-ellipsoid emitters, incorporating the effect of shielding for various parameters of LAFE. With the available formulas, the current distribution can be accurately predicted [24].

For applications related to rf injectors, the quality of the beam is crucial for for reliable operation, especially its transverse beam properties and total emission current. Mitigating the shielding effect is critical for RF gun devices. Unlike in the DC environment, when LAFEs are employed in an RF gun, the emitters are subjected to a varying macroscopic field across the LAFE cathode. The transverse field is maximum at the center of the cavity and gradually decreases towards the periphery. The non-uniform distribution of rf field in the RF cavity environment leads to varying macroscopically applied field across the emitters present in a cathode. The rf field pattern in a rf gun has the potential to counteracts the $\gamma$ distribution observed due to the shielding effect. Unlike DC case, the field emission current distribution of the LAFE in rf gun can be different due to the competing effect of both factors which ultimately decide the local field value at the emitter tip. It is thus necessary to incorporate the effect of varying transverse rf cavity fields for the realistic prediction of current and charge distribution from LAFE in a rf gun setup as the longitudinal as well as transverse beam dynamics depends on the input beam parameter.

The present study aims to understand the role of rf field distribution in the cavity in mitigating the shielding effect of LAFE. The rf field distribution in a rf gun environment will results in a temporally and as well as spatially varying applied macroscopic field in the emitter location. A novel hybrid approach has been proposed for quick and reliable assessment of the total current and current distribution of a LAFE employed in a ½ cell S-band (2856 MHz) gun. The new approach decouples the effect of field enhancement factor of the individual emitter from the macroscopic field applied. The current method utilises analytical formula for $\gamma$ distribution calculation inclusive of shielding effect. The macroscopic rf field distribution of the 2856 MHz rf gun cavity has been numerically calculated using 'COMSOL Multiphysics' software. The field emission current of the LAFE which depends on the product of $\gamma$ and rf field in the cavity has been calculated using the Murphy-Good formalism [33–35]. The new approach has been validated by numerically solving 9 emitter LAFE in a X band rf gun setup.

Our findings demonstrate that the field emission current distribution can be significantly influenced by the applied macroscopic fields. Under favorable conditions, the current distribution pattern can not only mitigate the screening effect but also provide a transverse Gaussian beam, which is maximum at the center and ideal for minimizing transverse beam emittance [36]. In this work, we systematically investigate the effect of various LAFE parameters such as aspect ratio, emitter height, cathode size, emitter count, inter-emitter distance, and accelerating field gradient on the field emission performance of LAFE. These findings are vital for enhancing the performance and efficiency of field emission-based rf gun devices, particularly those used in high-precision and high-demand applications. This approach also provides a method for optimizing total current and transverse beam distribution which could be useful for emerging applications [37].

## 2. Methodology

The aim of this work is to calculte the emission current distribution of large area field emitters (LAFE) cathode present in an rf gun environment. For a realistic estimate of the beam current, a hybrid approach has been employed. The field enhancement factor distribution in a LAFE depends on various LAFE parameters such as

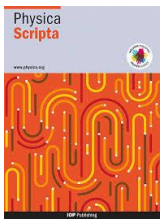

29

IOP Publishing Phys. Scr. 99 (2024) 076017 https://doi.org/10.1088/1402-4896/ad5649

Physica Scripta

PAPER

# Transformer based deep learning hybrid architecture for phase unwrapping

Karthik Goud Bujagouni and Swarupananda Pradhan

Photonics & Quantum Optics section, Atomic & Molecular Physics Division, BARC Facility, Visakhapatnam 531011, India

E-mail: bkarthik@barc.gov.in

Keywords: deep learning, phase unwrapping, vision transformer, CNN., digital holographic microscopy

Supplementary material for this article is available online

OPEN ACCESS

RECEIVED
6 March 2024

REVISED
23 May 2024

ACCEPTED FOR PUBLICATION
10 June 2024

PUBLISHED
21 June 2024



## Abstract

A deep learning Hybrid architecture for phase unwrapping has been proposed. The hybrid architecture is based on integration of Convolutional Neural Networks (CNN) with Vision Transformer. The performance of Hybrid architecture/network in phase unwrapping is compared against CNN based standard UNET network. Structural Similarity Index (SSIM) and Root Mean Square Error (RMSE) have been used as performance metrics to assess the performance of these deep learning networks for phase unwrapping. To train and test the networks, dataset with high mean Entropy has been generated using Gaussian filtering of random noise in Fourier plane. The Hybrid architecture is tested on test dataset and is found to have superior performance metrics against the UNET network. Their performance is also tested in noisy environment with various noise levels and Hybrid architecture demonstrated better anti-noise capability than UNET network. Hybrid architecture was successfully validated in real world scenario using experimental data from custom built Digital Holographic Microscope. With the advent of newer architectures and hardware, Deep learning networks can further improve the performance in solving inverse problems.

## 1. Introduction

Estimation of phase is a very important requirement in many fields. It is typically computed in various techniques such as for surface profiling measurements in interferometry and optical metrology, surface topography measurements in synthetic aperture radar, magnetic field measurements in MRI etc [1–3]. Phase is the main parameter of interest in Quantitative Phase Imaging techniques like Digital Holographic Microscopy [4]. Generally the calculated phase is wrapped in the range $[-\pi, \pi]$ due to inverse trigonometrical functions involved in the computation process. Phase unwrapping is required to obtain a continuous phase beyond the range $[0, 2\pi]$ or $[-\pi, \pi]$. Various techniques are available such as Quality-guided phase unwrapping, Minimum-norm methods, temporal phase unwrapping, Deep learning-based phase unwrapping etc [5, 6]. Spatial unwrapping techniques such as minimum norm, quality guided methods etc have limitations in handling the phase discontinuities and disjoint regions whereas temporal techniques requires multi frames or multi frequency fringes [5]. Deep learning is gaining attraction in various fields such as microscopy, holography, super resolution imaging, optical image encryption, interferometry, natural language processing (NLP), facial recognition, autonomous vehicles, medical image analysis, drug discovery, disease diagnosis, treatment recommendation, etc [7–11]. Advent of newer and complex architectures because of the availability of necessary hardware such as Graphics Processing Units (GPUs) and Tensor Processing units (TPUs) has improved the performance of deep learning in various fields [12]. Convolutional Neural Networks (CNN) in deep learning has advanced the field of medical image segmentation. UNET based on CNN has become the backbone for segmentation problem [13]. Many variants such as UNET++, Attention UNET, Residual UNET, Inception UNET etc were designed to improve the performance [14]. With introduction of Transformers, the field of NLP has seen exponential growth. Chat Generative Pre-Trained Transformer (ChatGPT) and other such large

IOP Publishing Phys. Scr. 99 (2024) 076017 K G Bujagouni and S Pradhan

language models are prime examples. Inspired by Transformer's success in NLP, Transformer was applied to image recognition problem by Alexey *et al* [15]. Since then, the application of Vision Transformers in image processing such as segmentation has expanded. Recently various architectures combining CNN and Transformers have been proposed for image segmentation resulting in improved performance [16–18]. Phase unwrapping problem can be considered similar to an image processing problem. Deep learning (DL) has been considered for phase unwrapping in various approaches. In one of the approaches, the unwrapping is considered as semantic segmentation problem and wrap count of the pixels is predicted using DL. Various architectures such as SegNet, DeepLabv3+, new loss function along with dense blocks etc were proposed in the above approach [19–22]. Here, inaccurate wrap counts due to inaccurate classification, results in error of integral multiples of $2\pi$. In another approach, one-step phase unwrapping is considered, where the DL network directly maps the input wrapped phase array to the output unwrapped phase array [23–25]. UNET or its variant has been used as a backbone typically in one-step phase unwrapping. In both of the above approaches to phase unwrapping, typically CNN based architectures were used. Even though CNN has achieved tremendous success, there are limitations to convolutional networks. As convolution operation is intrinsically local, convolutional networks are at a disadvantage in dealing with long range or global relations [16]. Transformers on the other hand have been demonstrated to model long range dependencies or global contexts successfully [16]. Various Hybrid architectures using Transformers and CNN are possible. But seamlessly combining Transformers and CNN to mitigate their drawbacks and enhance the performance for phase unwrapping is in itself a challenge. There have been very few reports in this direction.

Zhu *et al* [26] have proposed a hybrid model 'Hformer' based on Cross Attention Transformer (CAT) and a type of CNN called High Resolution Network (HRNet) for phase unwrapping in fringe projection. In this model, input phase is fed to HRNet followed by Encoder Decoder network with CAT as building blocks. The model predicts wrap count or fringe order as output. Sun *et al* [27] proposed another architecture using a channel wise cross fusion transformer with UNET for phase unwrapping in single shot fringe projection profilometry. Zhao *et al* [28] have combined Swin Transformer with Zernike polynomial fitting for phase unwrapping. Here Zernike polynomial coefficients are predicted by the Swin Transformer network.

In this communication, a novel Hybrid architecture different from the above approaches has been proposed for phase unwrapping in Digital Holographic Microscopy.

The highlights of this work are as follows.

- Vision Transformer containing multiple Transformers with Multi Head Attention is integrated with a residual connection into CNN.
- Synthetic dataset with high mean Entropy is generated for training and testing the network.
- The network's performance was tested with Gaussian noise of various Signal to Noise Ratios and compared with UNET.
- The Hybrid network was tested in real world scenario with experimental data from custom built Digital Holographic Microscope.

## 2. Materials and methods

### 2.1. Dataset

Dataset consists of input phases and their corresponding ground truth phases. Each input phase is a wrapped phase, represented by a 2d array of size $128 \times 128$, with range $[-\pi, \pi]$. The corresponding ground truth phase is unwrapped phase, represented by a 2d array of size $128 \times 128$. The range of the unwrapped phases/ground truth phases in the dataset is $[-32, 32]$ radians. The dataset contains 4000 input phases and their corresponding ground truth phases. This dataset is split into 80% as training dataset (3200 pairs) and 20% as test dataset (800 pairs).

The above dataset is generated by the procedure described as follows. First, unwrapped phases/ground truth phases $\varphi(x, y)$ are generated and then the corresponding wrapped phases/input phases $\psi(x, y)$ are generated by the following equation (1).

$$\psi(x, y) = argument\{\exp(i\varphi(x, y))\} \tag{1}$$

The method to generate unwrapped phases/ground truth phases is based on Random surface generation using circularly symmetric filters and FFT proposed by Hu *et al* [29]. In this method, a 2d array of Gaussian distributed random numbers is generated and its 2d-FFT (2d Fast Fourier transform) is computed. Then its product with a 2d circularly symmetric filter function is computed. 2d-IFFT (inverse 2d Fast Fourier transform) of the resulting array is computed to generate random surface. By varying the filter parameters and Gaussian

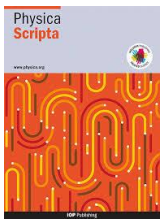

30

IOP Publishing Phys. Scr. 99 (2024) 115001 https://doi.org/10.1088/1402-4896/ad7dbe

Physica Scripta

PAPER

# Unveiling novel drug delivery mechanism: Cisplatin's bonding behaviour with $BC_4N$ Nanostructure

**Seetha Lakshmy**[1], **Brinti Mondal**[2], **Ravi Trivedi**[3,4], **Nandakumar Kalarikkal**[1,5,6], **Nandini Garg**[7] and **Brahmananda Chakraborty**[7,8]

[1] International and Inter University Centre for Nanoscience and Nanotechnology, Mahatma Gandhi University, Kottayam, Kerala-686560, India
[2] Department of Physics, Indian Institute of Technology, Powai, Mumbai-400076, India
[3] Department of Physics, Karpagam Academy of Higher Education, Coimbatore- 641021, Tamil Nadu, India
[4] Centre for Computational Physics, Karpagam Academy of Higher Education,Coimbatore-641021, Tamil Nadu, India
[5] School of Pure and Applied Physics, Mahatma Gandhi University, Kottayam, Kerala-686560, India
[6] School of Nanoscience and Nanotechnology, Mahatma Gandhi University, Kottayam, Kerala-686560, India
[7] High Pressure & Synchrotron Radiation Physics Division, Bhabha Atomic Research Centre, Trombay, Mumbai-400085, India
[8] Departments of Physics, HomiBhabha National Institute, Trombay, Mumbai-400085, India

**E-mail:** brahma@barc.gov.in

**Keywords:** anticancer drug cisplatin, $BC_4N$ nanostructure, density functional theory, pH effect, solubility, adsorption of drug

**OPEN ACCESS**

**RECEIVED**
10 May 2024

**REVISED**
12 September 2024

**ACCEPTED FOR PUBLICATION**
20 September 2024

**PUBLISHED**
1 October 2024



## Abstract

Recent advancements in nanotechnology have opened avenues to address the selectivity challenges in targeted drug delivery systems, minimizing adverse effects. While carbon nanotubes (CNTs) have gained traction as drug carriers, their B, N-containing counterpart, pristine boron carbonite (p-$BC_4N$), remains underexplored. This study investigates the possibility of pristine boron carbonite (p-$BC_4N$) nanotubes as a drug carrier for the anticancer medication cisplatin (CPT). Using first-principles Density Functional Theory (DFT) simulations, we examined the interaction between CPT and p-$BC_4N$ nanotubes, revealing favourable adsorption energies (−0.523 eV) due to orbital interactions and charge transfer between the C 2p orbitals of $BC_4N$ and the 1 s orbitals in H of CPT. *Ab initio* molecular dynamics (AIMD) simulations confirmed the stability of the system at room temperature. Furthermore, pH and temperature-dependent desorption measurements demonstrated the effectiveness of p-$BC_4N$ nanotubes as a promising candidate for CPT drug delivery, highlighting their potential in targeted cancer therapy. This work opens up new avenues for the development of nanotechnology-based drug delivery systems.

## 1. Introduction

In 2012, cancer claimed the lives of 8.2 million people worldwide, and the World Health Organization predicts that the number will rise to 22 million by 2035 [1]. The most popular systemic therapy for halting cancer cell growth, disease spread, and metastasis is chemotherapyp [2], and the most popular anticancer drug to date is cisplatin (CPT) [3]. CPT, also known as CDDP or cis-diamminedichloroplatinum (II), is a platinum (Pt) coordination complex that exhibits significant properties to fight against the spread of cancer in living cells. The path of action of this drug is to modify the damaged DNA through intrastrand, interstand or crosslinks, and formation of other adducts, which eventually stops the replication and transcription of the cell [3]. Rosenberg and Vancamp first suggested CPT as a potential chemotherapy agent in 1969 [4], and the FDA approved its use for treating ovarian and testicular cancers in 1978 [5]. Due to its broad spectrum of antitumor activity, CPT is still one of the most popular and successful anticancer drugs that are used to treat a variety of solid tumours, such as lung cancers, as well as cancers of the head and neck, liver, lung, breast, ovary, testicles, bladder, and lungs [5, 6]. However, the non-specific distribution of conventional chemotherapeutic agents, including the most popular and effective cisplatin affects both cancerous and healthy cells in the body [7].

For anticancer medications to be operative in the treatment of cancer, they must be able to penetrate bodily barriers and reach the targeted tumor tissues with the least amount of volume or activity loss [8]. Second, drugs should be able to selectively target tumor cells without harming healthy cells once they have entered the tumor tissue by using a controlled release mechanism of the active form [2, 8]. Growing evidence suggests that nanoparticles may be able to meet both of these criteria for efficient drug carrier systems[4]. Nanoparticles can increase the intracellular concentration of drugs in cancer cells while reducing their toxicity in normal cells by using both passive and active targeting strategies [9, 10]. Furthermore, when nanoparticles attach to particular receptors and enter cells, they are typically engulfed by endosomes via receptor-mediated endocytosis, avoiding recognition of P-glycoprotein, one of the primary mechanisms for drug resistance [11].

As an anticancer nano-drug delivery system (DDS), in the 1960s liposomes and micelles were; and in the 1980s nanoparticles and dendrimers were introduced [12]. Liposomes, which are made of a lipid bilayer, are pH-sensitive drug carriers with good biocompatibility. However, the amphiphilic nature of liposomes makes them physically unstable, and in some instances, they can cause superficial toxicity, or the 'hand and foot syndrome' [13]. Drug delivery via dendrimer-based multifunctional systems has the main flaw of extremely slow drug release at the target site (less than 15% over 20 h), associated withhigh cost [14, 15]. Nanocarriers like magnetic nanoparticles, micelles, and polymeric nanoparticles have many advantagescompared to other conventional DDS. However, they also have disadvantages like toxicity, poor biocompatibility, decreased solubility, and limited therapeutic indices a significant alternative to all the discussed possible DDSs, carbon-based nanomaterials like graphene, fullerene, carbon nanotubes, and carbon dots draw much attention because of their large surface area, low weight, low cost, structural flexibility, structural stability, interactions with drugs, and biomolecules, and antioxidant and antibacterial properties, which can be used to overcome these drawbacks [16, 17]. Moradnia *et al* [18] reported successfull adsorption of anti cancer gemcitabine using the density functional theory (DFT) and molecular dynamics (MD) circulation. By using MD simulation, Dehneshin *et al* [19] compared the adsorption kinetics of different anticancer medications on the functionalized CNTs. They claimed that streptozotocin primarily participates in hydrogen bonding with functional CNTs, whereas, so rafeni bands unit in ib adsorption includes both hydrogen bonding and $\pi$-$\pi$ stacking on the functionalized CNTs.Using MD simulation, Maleki *et al* [20] examined the process of adsorption of the anticancer drug doxorubicin on the exterior surface of CNT. They claimed that the process of adsorption was determined by the van der Waals interaction between the drug and the CNT. Kiruta *et al* [21] also studied the possibilities of CNTs as a carrier of doxorubicin and analyzed the best solvent for the process as water. Ghadamgahi *et al* [22] investigated the spontaneous interaction of CNT and anti-skin-cancer drug tretinoin; further proving the efficiency of CNTs as nanocarriers for drugs.

An analogous layered structure to a CNT can be found in boron nitride nanotubes (BNNT). After the success of CNT drug carriers, researchers were greatly inspired by the intriguing characteristics of carbon nanotubes to investigate analogous materials like boron nitride (BN), boron carbon nitride (BCN), and boron carbide (BC) nanotubes. Stephan *et al* [23] first reported CNTs containing B and N, and after that, both the interest and the demand kept growing, which acted as the fuel for the continuing research [24]. Homogeneous BCN nanotubes have been explored vigorously for their tuneable properties with tuneable composition intheapplicationof novel composites, electrical conductors, hydrogen storage, gas sensing, electronics, and other fields in forms of BN, BCN, $BC_2N$, $BC_7N$, $BC_4N$, $B_5CN_5$, etc [25, 26]. Unlike CNTs, B-based nanotubes were found to be more bio-friendly and less toxic [27–30], which encouraged the research of the same drug carriers.The mechanical properties and thermal conductivities of the two systems are similar [31–33]. However, BNNT differs from CNT in many ways. For example, BNNT has a large band gap independent of its structural parameters, is structurally stable, and is chemically inert; whereas, CNTs can be either metals or semiconductors depending on tube curvature and diameter, which are difficult to control. Because of these aspects, BNNT is especially well suited forapplications in living organisms. Additionally, BNNT does not absorb visible or infrared light; this would guard against overheating and harm to biological molecules, similar to the case of CNT usage. Zhi *et al* [34] first reported the biological application of BNNTs for protein immobilization.Ciofani *et al* [35] first time demonstrated the application of BNNT in targeted drug delivery. Dehaghani *et al* [36] reported theoretical possibilities of using CNT and BNNT as anticancer drug fluorouracil (FU) carriedthrough molecular dynamics. Khatti *et al* [37] reported on the effectiveness of BNNT and hydroxylated BNNT as Pt-based drug nanocarriers. They discovered that the -OH groups aid in the incorporation of the Pt-based drugs into the BNNT via H-bonding as well as the vdW interaction between the drug and the functionalized BNNT. According to Roosta *et al* [38], the spontaneous encapsulation of gemcitabine into the cavity of BNNT (18, 0) is evidenced by the negative interaction energy.

The $BC_4N$ nanotube has a graphitic structure in which $BN_3$ and $NB_3$ units are interconnected by B–N bonds and is a small band gap material with unique mechanical and electronic properties. They can be synthesized by incorporating definite composition of B and N in the CNT structure. Since the BNnanotubes are biocompatible, the presence of less toxic C, N and B atoms in the $BC_4N$ nanostructure makes them biocompatible and can be

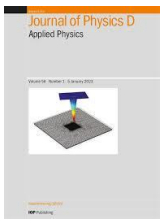

31

OPEN ACCESS
IOP Publishing
Journal of Physics D: Applied Physics
J. Phys. D: Appl. Phys. **57** (2024) 495502 (12pp)
https://doi.org/10.1088/1361-6463/ad75a1

# Zr doped $C_{24}$ fullerene as efficient hydrogen storage material: insights from DFT simulations

**Ajit Kundu**[1], **Ankita Jaiswal**[2], **Pranoy Ray**[3], **Sridhar Sahu**[2] and **Brahmananda Chakraborty**[3,4,*]

[1] Seismology Division, Bhabha Atomic Research Centre, Mumbai, Maharashtra 400085, India
[2] Computational Materials Research Lab, Department of Physics, Indian Institute of Technology (Indian School of Mines), Dhanbad, Jharkhand 826004, India
[3] High Pressure and Synchrotron Radiation Physics Division, Bhabha Atomic Research Centre, Mumbai, Maharashtra 400085, India
[4] Department of Physics, Homi Bhabha National Institute, Mumbai, Maharashtra 400094, India

E-mail: brahma@barc.gov.in

Received 21 September 2023, revised 13 August 2024
Accepted for publication 30 August 2024
Published 12 September 2024

**Abstract**

In this article, we report the hydrogen storage capacity of zirconium (Zr) decorated $C_{24}$ fullerene using state-of-the-art density functional theory simulations. Our study shows that zirconium, like most other transition metals, tends to bind strongly on the C–C bridge of $C_{24}$ fullerene with a maximum binding energy of −3.64 eV. Each Zr atom decorated over $C_{24}$ fullerene can adsorb a maximum of $7H_2$ molecules with an average adsorption energy of −0.51 eV/$H_2$, leading to a gravimetric density of 7.9 wt%, which is higher than the prescribed target of 6.5 wt% set by United States-Department of Energy. There is a charge transfer from Zr to C atoms in $C_{24}$ fullerene, which is the primary cause of the binding of Zr with $C_{24}$ fullerene. $H_2$ molecules are adsorbed over Zr sorption sites via Kubas-type interactions, which include charge donation from the filled *s* orbitals of hydrogen to the vacant 4*d* orbital of Zr and subsequent back charge donation to unfilled $s^*$ orbital of hydrogen from the filled 4*d* orbital of Zr. The structural stability of the Zr + $C_{24}$ system at a high temperature of 500 K is verified using *ab-initio* molecular dynamics calculations. The high diffusion energy barrier of Zr (2.33 eV) inhibits clustering between the Zr atoms decorated on the $C_{24}$ fullerene and ensures the system's practical feasibility as a high-capacity $H_2$ adsorbing system. Therefore, our computational studies confirm that Zr decorated $C_{24}$ fullerene is stable and can be regarded as a potential candidate for $H_2$ storage systems with optimum adsorption energy range.

Keywords: hydrogen storage, DFT, fullerene, adsorption, Kubas interaction, clustering

* Author to whom any correspondence should be addressed.

J. Phys. D: Appl. Phys. **57** (2024) 495502 A Kundu *et al*

## 1. Introduction

Research into alternative energy resources has intensified due to the rapid depletion of fossil fuels [1] and their adverse impacts on the environment, leading to pollution and global warming [2]. In this apprehensive scenario, hydrogen has been investigated as the most promising candidate for green energy because of its natural abundance, maximum energy density among all the fossil fuels known, and clean combustion [3]. Therefore, hydrogen-based fuel has been demonstrated to meet all of the above criteria for green energy, making it a promising 'future' fuel source [4]. However, hydrogen production and its efficient storage are the significant challenges that prohibit the development of a hydrogen-based economy in full fledge. Conventional storage systems are linked with significant technical challenges and security considerations, such as storing hydrogen in gaseous form at high pressure (700–800 bar) or in liquid form at cryogenic temperature (20 K). Thus, these conventional storage methods are not very reliable and trustworthy for the efficient development of cost-effective hydrogen-based transportation systems [5]. Therefore, substantial research is being conducted in this field to develop more efficient techniques for hydrogen storage in material-based systems. However, the efficiency and reusability of the material-based systems for hydrogen storage is a major challenge today. According to the United States-Department of Energy (US-DoE) [6], a material-based system can be considered as promising hydrogen storage material only when it satisfies the following two major criteria-the system should be capable of holding $H_2$ molecules at least 6.5 wt%, and the $H_2$ molecules should be bonded with the material complex with optimum adsorption energy lying in between the range of −0.1 eV to −0.8 eV [7, 8]. Further, the target set by US-DoE for onboard hydrogen storage in light-duty vehicles consisting of hydrogen-based fuel cells is 4.5% by 2020, 5.5% by 2025, and 6.5 wt% overall.

In the decades-long search for an alternative fuel to chemical fuels, many materials, including zeolites [9, 10], metal hydrides [11, 12], metal–organic frameworks [13, 14], etc, have made it onto the list of prospective material-based hydrogen storage systems. However, most of these materials investigated thus far have been found to be either non-feasible for practical applications or non-reusable with limited storage capacity. Conversely, carbon nanostructures like nanoclusters [15, 16], fullerenes [17, 18], graphene [19, 20] etc, when decorated with various alkali metals as well as transition metals like Sc, V, Ti, Zr, etc, provide a feasible and cost-effective medium for the hydrogen storage [21, 22]. Transition metal–doped carbon nanomaterials have recently been explored as possible candidates for material-based hydrogen storage systems because of their large surface area, high stability, good mechanical properties, and low weight. Using first principles simulations, Chakraborty *et al* had previously reported that each Zr and Y atom doped on the surface of the single-walled nanotube could adsorb $4H_2$ and $6H_2$ molecules, respectively, which undergoes 100% desorption at optimum temperature range [23, 24]. Hydrogen adsorption on Pd-doped graphene [25], Cu-functionalized-B-doped graphene sheet [26], and various other materials [27–31] have been investigated and explored as possible hydrogen storage mediums using density functional theory (DFT) simulations. We recently demonstrated through DFT-D3 simulations that Ti-doped Ψ-Graphene is a potential hydrogen storage material with $H_2$ storage capacity of approximately 14.13 wt%, nearly double the target set by US-DoE [32].

Since the discovery of fullerenes in 1985 [33], there has been an upsurge in their investigation of stable carbon nanomaterials. Nevertheless, it has not been extensively explored as a suitable material for hydrogen storage. However, recently, fullerenes have gained widespread appeal in hydrogen storage research due to their porous property, high structural symmetry, and stability. Schur *et al* have experimentally demonstrated that $C_{60}$ fullerene can hold $H_2$ molecules with a gravimetric density of about 7.7 wt% [34]. It is already studied that chain terminated $C_{20}$ fullerene can adsorb $H_2$ molecules with an average binding energy lying in the range of 0.30–0.34 eV/$H_2$ [35]. Further, Teprovich *et al* also experimentally showed that Li-doped fullerene can hold multiple $H_2$ molecules, achieving a gravimetric density of 5 wt% [36]. Recently, Sathe *et al* have demonstrated that Ti-doped $C_{24}$ fullerene can efficiently adsorb multiple $H_2$ molecules with adsorption energies lying in the range of 0.33–0.76 eV, and the adsorbed $H_2$ molecules undergo desorption at optimum thermodynamic conditions [37]. Ammar *et al* investigated the hydrogen storage properties of Ti-decorated $C_{20}$ fullerene and showed that each Ti could adsorb more than $6H_2$ molecules [38]. Further, our studies have also demonstrated that Sc and Y-doped $C_{24}$ fullerene can serve the purpose of potential hydrogen storage materials [39, 40]. A study by Sahoo and Sahu showed that Ti functionalized paracyclophane could adsorb $H_2$ molecules with a gravimetric density of 7.37 wt% [41]. In addition, Guo *et al* have also reported that in Ti-doped $C_{60}$ fullerene, the first $H_2$ molecule undergoes dissociation and is adsorbed in atomic form, whereas the other $4H_2$ are adsorbed in molecular fashion [42]. Recent study shows that Zr decorated 2D holey graphyne can hold multiple $H_2$ molecules and thereby achieving a gravimetric density of 7.5 wt% [43].

In this paper, we address the $H_2$ adsorption as well as interaction with Zr-doped $C_{24}$ fullerene. $C_{24}$ fullerene is a highly symmetric non-metallic cage made up of hexagonal and tetragonal carbon rings. Previous studies report that $C_{24}$ is mechanically and thermodynamically stable [44] and can be successfully synthesized in the laboratory using pyrrole-n-carboxylic acid [45]. As a result, it opens up the possibility of researching it as a more practical hydrogen storage material. Unlike other transition metals, Zr-doped $C_{24}$ fullerene has not yet been studied for hydrogen storage, making it more interesting to investigate its interaction and $H_2$ uptake capacity.

The article is further segmented into three primary sections. In section 2, we outline the computational requirements for conducting this study. Section 3 focuses primarily on the

# Alphabetical List of Division Engaged in Open Access Publishing

## IOP Publishing
## Year 2023

1. Advanced Tunable Laser Applications Division
2. Applied Physics Division
3. Beam Technology Development Group
4. Chemistry Division
5. Electromagnetic Applications & Instrumentation Division
6. Electromagnetic Applications & Instrumentation Division
7. Fuel Chemistry Division
8. Radiation Safety Systems Division
9. Ion Accelerator Development Division
10. Materials Processing & Corrosion Engineering Division
11. Materials Science Division
12. Radiation Biology and Health Sciences Division
13. Radio Analytical Chemistry Division
14. Radiological Physics and Advisory Division
15. Research Reactor Services Division
16. Solid State Physics Division
17. Theoretical Physics Section
18. Water and Steam Chemistry Division

## IOP Publishing
## Year 2024

1. Accelerator & Pulsed Power Division
2. Atomic and Molecular Physics Division
3. Beam Technology Development Group
4. Beamline Development section
5. Computational Analysis Division
6. Fuel Chemistry Division
7. Health Physics Division
8. High Pressure & Synchrotron Radiation Physics Division
9. Industrial Hygiene & Safety Section
10. Ion Accelerator Development Division
11. Materials Processing & Corrosion Engineering Division
12. Mechanical Metallurgy Division
13. Nuclear Physics Division
14. Pulse Power and Electromagnetic Division
15. Radiation Safety Systems Division
16. Radiological Physics & Advisory Division
17. Reactor Safety Division
18. Seismology Division
19. Solid State Physics Division
20. Technical Physics Division
21. UGC-DAE Consortium for Scientific Research

# Alphabetical List of Authors Engaged in Open Access Publishing

## IOP Publishing
## Year 2023

# IOP Publishing
# Year 2024

**A**
A Biswas
A Kedharnath
A P Singh
A T Sathya
Abinash Chakraborty
Aditya Nandan Savita
Ajay K Mishra
Ajinkya P Khangal
Ajit Kundu
Alok Kumar Ghosh
Anandhu Mohan
Anannya Banerjee
Anirudh Chandra
Ankita Jaiswal
Apu Sarkar
Archana Sharma
Arghya Chattaraj
Arnab Sarkar
Ashok K Verma

**B**
B K Sapra
B.R. Doshi
Basanta Kumar Das
Belli Nagaraju
Bhavesh Kadia
Biswaranjan Dikshit
Brahmananda Chakraborthy
Brinti Mondal

**C**
C Prathap
C S Rout
C.N. Gupta
Chitra Lekha C S

**D**
D Bhattacharyya
D. Kumawat
Deepak N Mathad
Dhananjay Kumar Pandey

**F**
Fency Sunny
Fouran Singh

**G**
G. Shukla
Gurupada Ghorai

**H**
Hari Prasad M
Hariom Sogarwal
Harsh Bhatt
Harsh Hemani
Harshita Raj

**I**
I.V.V. Suryaprasad

**J**
J P N Pandey
J. Ghosh
Jayanta Mondal
Jose V Mathew

**K**
K.A. Jadeja
K.M. Patel
K.S. Shah
Kajal Shah
Karthik Goud Bujagouni
Kaushlender Singh
Kumudni Asudani

**L**
L.M. Pant

**M**
M H Modi
M S Kulkarni
M.B. Chowdhuri
M.N. Makwana
Manmadha Rao
Manoj Kumar
Manoj Warrier
Minsha Shah
Munir S Pathan

**N**
Nandakumar Kalarikkal
Nandini Garg
Nandini Yadava
Neeraj Parashar
Neeraj Shiv
Nilam Ramaiya
Nishant N Patel
Nitin R Kakade

**P**
P Modak
P Sarkar
P.N. Maya
P.S. Sarkar
Pallavi Priyadarshini
Pankaj Kumar
Parag M Ahmedabadi
Paritosh Chaudhuri
Prabal Kumar Chattopadhyay
Pradeep Kumar Maurya
Pranoy Ray
Prashant Shukla
Pratap K Sahoo
Praveenlal Edappala

**R**
R B Tokas
R I Bakhtsingh
R. Manchanda
R. Pal
R.L. Tanna
Raghavendra K.
Raghwinder Singh Grewal
Rahulnath P.P.
Rajeev Kapoor
Rajesh Kumar
Rajiv Goswami
Ramandeep Gandhi
Rashmita Das
Ravi Trivedi
Rishi Verma
Rohit Kumar

**S**
S D Sharma
S M Pradhan
S N Jha
S Santra
S. Aich
S. Chaturvedi
S.K. Pathak
Sambaran Pahari
Sanjay Rai
Saroj Bishnoi
Saroj Kumar Jha
Seetha Lakshmy
Sherry Rosily
Shivam Gupta
Shreya G Sarkar
Sridhar Sahu
Srinivas Krishnagopal
Sudip Mandal
Sukantam Mahar
Suman Dolui
Surendra Singh
Swadesh Kumar Patnaik
Swarupananda Pradhan

**T**
T Palani Selvam
Tanmay Macwan
Tarun Patel

**U**
U V Deokar
U.D. Malshe
Umesh Nagora
Utkarsh Bhardwaj

**V**
V. Balakrishnan
Varsha S.
Vyaghri LS Rao Sista
Vyom Saxena

**Y**
Y.C. Saxena
Yogesh Kumar